STUDY OF PHOTOVOLTAIC (PV) MODULE INTERCONNECTIONS FAILURE ANALYSIS AND RELIABILITY

ALIREZA ESLAMI MAJD

DOCTOR OF PHILOSOPHY

AUGUST 2021

Study of Photovoltaic (PV) Module Interconnections Failure Analysis and Reliability

Alireza Eslami Majd

School of Engineering,
Faculty of Science and Engineering,
University of Wolverhampton,
WV1 1LY, UK.
a.e.majd@wlv.ac.uk

A thesis submitted in partial fulfilment of the requirements for the award of Doctor of Philosophy of University of Wolverhampton.

August 2021

Declaration

This research has not been submitted in any form for any degree nor is it being submitted simultaneously for any degree other than the Doctor of Philosophy (PhD) being studied at the University of Wolverhampton. Also, I declare that this thesis is a product of my own investigations except otherwise stated and clearly acknowledged with references hence, I have not plagiarized the work of others.

Alireza Eslami Majd 24/01/2022

---------------------------- ----------------------------

Alireza Eslami Majd Date

(Student)

Nduka Nnamdi Ekere 24/01/2022

---------------------------- ----------------------------

Professor Nduka Nnamdi Ekere Date

(Director of Study)

Fideline Tchuenbou-Magaia 24/01/2022

---------------------------- ----------------------------

Dr. Fideline Tchuenbou-Magaia Date

(Director of Study)

Dedication

This Ph.D. thesis is dedicated to my secondary school teacher, Mr. Asghar Kianpour, and to the memory of my father, Gadder Eslami Majd, who kindly encouraged me to put my best efforts into my educational pursuit. I also dedicate this thesis to my family who have always loved me unconditionally.

.

Stephen Hawking:

"However difficult life may seem, there is always something you can do and succeed at."

Acknowledgment

I would like to acknowledge my supervisor Professor Nduka Nnamdi Ekere, for his continued and consistent support and the invaluable guidance that he provided me throughout this study. I would also like to thank the Faculty of Science and Engineering, University of Wolverhampton for their support in providing me with the sponsorship for my Ph.D. studies. Furthermore, I would like to express my appreciation and gratitude for all the considerate cooperation of the other members of my supervisory team and the School of Engineering staff during my study. Finally, I am grateful to Dr. Armin Rahmati, for his advice and the suggestions he provided during this study.

Abstract

Solar Energy is one of the most widely used renewable energy sources, with the solar Photovoltaic (PV) module technologies deployed as one of the primary renewable energy sources to replace fossil fuels. However, the R&D challenge for improving the performance and reliability of PV modules has become an urgent and critical agenda for the energy generation industry sector. The interconnection between the solar PV cells is a very important part of the PV module assembly, and its failure can adversely affect the performance and reliability of the PV module. The interconnection failure has been mostly linked to the crack initiation and propagation in the solder joints used to connect the ribbon interconnection to the cell.

This research focuses on the study of the thermal failure of PV module solder joint to determine the optimum ribbon interconnection designs that will give improved thermo-mechanical reliability. It develops a virtual reliability qualification process for the assessment of the life expectancy of PV module interconnections. The FEM simulations in ABAQUS 2019 software are implemented to investigate failure of the solder joints in different ribbon interconnection designs under anticipated life cycle loading conditions and high temperature lamination process.

For the first time, the extended finite element method (XFEM) technique is used to determine the crack initiation temperature, crack location, direction and growth rate in solder joint of PV module interconnection under lamination process. Furthermore, the research used the Developed Morrow Energy Density lifetime model to determine the number of cycles to creep-fatigue failure, and then it defined a new generic exponent factor using the Coffin–Manson–Arrhenius model to estimate the lifetime for the designs under different thermal cycling conditions. The research also combines the numerical results of XFEM and creep-fatigue investigation to determine the failure lifetime of PV Module interconnection designs. The results show that the Multi-Busbar interconnection design improves solder joint creep-fatigue life (up to 15%) and consequently provides higher thermo-mechanical reliability for the solar PV modules compared to other studied designs (Conventional and the Light Capturing Ribbon interconnections).

The results of this PV module interconnections study can be used for evaluating potential design changes and to facilitate design for reliability validation of different configurations for improving the long-term PV module system reliability.

Table of Contents

List of Figures

List of Tables

Abbreviations

AC	Alternating Current
Al	Aluminium
Ag	Silver
BGA	Ball Grid Array
BL	Bridged-Link
CALS	Conductive Paste Assisted Low-Temperature Soldering
CEEQ	Equivalent Creep Strain
CdTe	Cadmium Telluride
CIGS	Copper Indium Gallium Selenide
CPE3	Three-node Linear Plane Strain Triangle
CPE4	Four-node Bilinear Plane Strain Quadrilateral
CR	Conventional Ribbon
CSP	Concentrated Solar Power
CTM	Cell-To-Module
CTE	Coefficient of Thermal Expansion
Cu	Copper
c_Si	Crystalline Silicon
DC	Direct Current
ECA	Electrically Conductive Adhesive
ECDDEN	Total Creep Dissipated Energy Per Unit Volume
EL	Electroluminescence
EVA	Ethyl Vinyl Acetate
FEM	Finite Element Method
GaAs	Gallium Arsenide
GFEM	Generalized Finite Element Method
HC	Honey-Comb
IEA	International Energy Agency
IMC	Intermetallic Compounds
LCF	Light Capturing Film
LCR	Light Capturing Ribbon

LEFM	Linear Elastic Fracture Mechanics
MAXE	Maximum Nominal Strain
MAXPE	Maximum Principal Strain
MAXPS	Maximum Principal Stress
MAXS	Maximum Nominal Stress
PCM	Phase Change Material
PCB	Printed Circuit Board
PV	Photovoltaic
QUADE	Quadratic Nominal Strain
QUADS	Quadratic Nominal Stress
SAC (solder)	SnAgCu (solder)
Sn	Tin
SnPb	Lead Eutectic (solder)
SP	Series-Parallel
SWCT	Smart Wire Connection Technology
TCT	Total-Cross-Tied
TF	Thin-Film
WLCSP	Wafer Level Chip Scale Packages
XFEM	Extended Finite Element Method
2D	Two Dimensional
3D	Three Dimensional

Notation

T	Absolute Temperature
W_i	Accumulated Creep Energy
Q	Activation Energy
θ	Angular Component for the Local Polar Coordinate
$F_\alpha(x)$	Associated Asymptotic Crack-Tip Function
H (x)	Associated Discontinuous Jump Function
w_{acc}	Average Accumulated Creep Energy Density (per Cycle)
A	Boltzmann's constant
β	Constant for Creep
ΔT	Cycling Temperature
V_i	Element Volume
W'	Energy Density Constant
G	Energy Release Rate
α	Exponent Factor
X_m	Extra Contact Length between Solder Joint and Silver Pad in MBB interconnection
K	Fracture Toughness
R	Gas Constant
Q	Internal Energy
T_m	Mean Cycle Temperature
a_I	Nodal Enriched Degree of Freedom Vector
b_I^α	Nodal Enriched Degree of Freedom Vector
$N_I(x)$	Nodal Shape Function
N_f	Number of Cycles to Failure
ν	Poisson's ratio
n	Power Constant for Creep
r	Radial Component for the Local Polar Coordinate
$\dot{\varepsilon}_{cr}$	Scalar Creep Strain Rate
S_e	Solder Area in MBB interconnection
H_e	Solder Height in MBB interconnection
S_m	Triangular Area of the Molten Solder in MBB interconnection
σ	Von Mises Effective Stress for Creep
E	Young's modulus

Chapter 1

1. Introduction to Thesis

This introductory chapter presents the background of this Ph.D. study, the importance of the renewable energy sector (in particular the solar PV module technology sub-sector), the problem context, and an overview on PV module failure and reliability. It also covers the research problem and motivation, aim and objectives, scope of research, research contributions, research programme and structure, and thesis outline.

1.1. Background of the Study

The use of solar PV technology is not new, photovoltaic cells (or solar panels), have long been utilised utilized as energy sources on rooftops, spacecraft, handheld calculators and other wearable electronic devices. The Photovoltaic (PV) module power generation has emerged as one of the most widely used renewable energy sources; this is due to their low installation costs and increasing costs competitiveness compared to other renewable energy sources. However, in spite of the global popularity and wider uptake of solar PV, improving the reliability of the PV modules remains one of the major challenges for the solar PV manufacturing industry, as they are keen to meet the lifetime warranty for their products.

The ribbon interconnections are widely used in the solar PV modules to connect the individual crystalline silicon (c-Si) solar cells and to transmit and conduct their electrical current to the external circuits. Solder materials are the most widely used interconnection materials for joining the ribbon interconnection to the solar PV cells. Figure 1 shows the 3D views of the interconnections assembly in a conventional solar PV modules.

The figure is redacted for the
public view due to lack of
permission of the copyright holder.

Figure 1: Ribbon interconnections used in the conventional PV modules, (left) 3D view of the solar PV module (right) 3D view of the interconnection assembly with showing main materials including ribbon interconnection, solder joint and silver-pad (Osborne, 2018).

The thermal strain energy induced in the PV module solder joints during the lamination process and during the lifecycle of the module has been identified as the main source of the thermal failure of the solder joint (and the associated failure of solar PV module interconnections). There is thus an urgent need for a fundamental study to provide better understanding of the effect of the PV module interconnection design on the solder joint failure modes and mechanisms and consequently, how the PV module interconnection configuration can affect the PV module interconnection reliability.

This study concerns a necessary, urgent and fundamental investigation of the thermal failure of the solder joint that lies at the heart of PV module ribbon interconnection manufacture. More specifically, it investigates the effect of ribbon interconnection configuration on the PV module failure and reliability; and how the FEM simulation modelling approach can be used to facilitate the design for reliability validation of different ribbon interconnection configurations to improve the long-term PV module reliability.

1.1.1. Renewable Energy Sector

The rapid development of renewable energy technologies over the last two decades has been driven largely by the growing concerns over the massive increase in global consumption of fossil fuels as well as the concerns associated with the impact of green-house gas emissions on climate change, and the increasing fear that fossil fuel reserves could run out by 2050. It has been reported that the renewable energy sector provided 19.9% of global final energy consumption in 2019 and that the share of modern renewable energy (excluding the traditional use of biomass) has increased from 8.7% in 2009 to 11.2% in 2019 (IRENA, 2020). Figure 2 shows the comparison of the Estimated Renewable Share (including wind, solar, biomass/fuel, geothermal, ocean power and hydropower) of the Total Final Energy consumption (including renewable sources and fossil fuel sources) for the years 2009 and 2019 (IRENA, 2020).

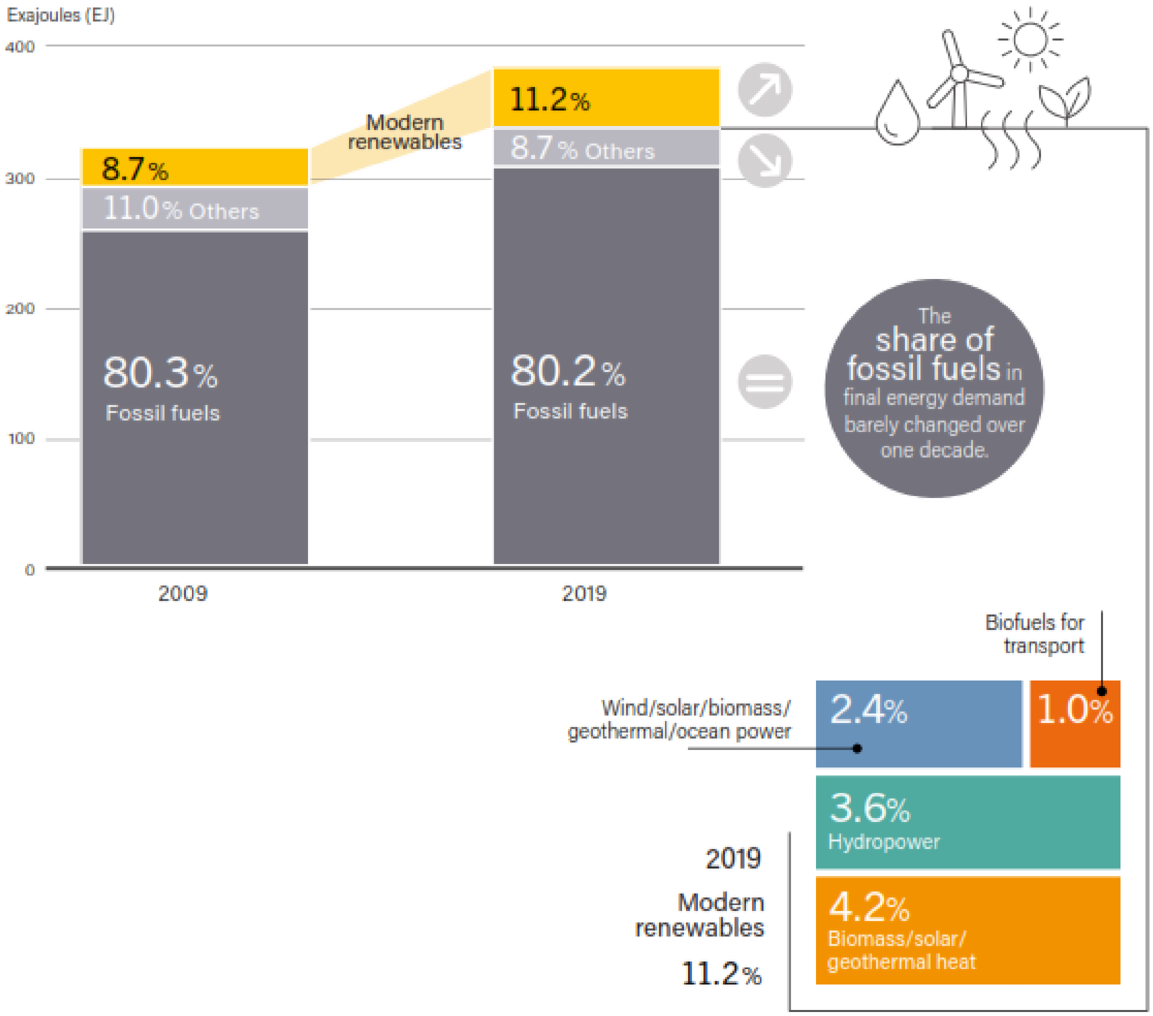

Figure 2: Estimated Renewable Share of Total Final Energy Consumption, 2009 to 2019 (IRENA, 2020).

The increasing energy demand and the rapid depletion of fossil fuel reserves have been identified as the main drivers for the massive investment globally in renewable energy technologies. With massive investments in renewable energy in recent years; renewable energy is establishing a strong foothold in the global energy system at a faster rate than any other fuel source in history; and for this reason renewable energy is expected to become the world's main source of power within two decades. In addition, according to the Renewables 2020 Global Status Report (IRENA, 2020), employment in the renewable energy sector (excluding large-scale hydropower) increased in 2018 to circa 11 million jobs (direct and indirect) with solar PV cells and biofuels providing the largest numbers of renewable energy jobs.

Renewable energy sources such as solar systems are now established around the world as mainstream sources of energy. This rapid growth of solar energy, particularly in the power generation sector, has been driven by several factors, including the energy security and environmental concerns, the improved cost-competitiveness, and the growing demand for energy in developing and emerging economies where energy access remains a challenge. This increase in the use of solar PV cells systems for generating electricity has also been driven by subsidy programs and economic incentives for investments by several governments. Due to the increased economic incentives, the worldwide growth of solar PV cells has been close to exponential between 1992 and 2018; thereby helping solar PV technology to evolve from a niche market of small-scale applications to a mainstream electricity source. This growth in solar PV cells is set to continue, and according to the IEA's latest 5-year forecast, renewable power capacity is set to expand by 50% between 2019 and 2024, led by solar PV cell technologies (IEA, 2019).

1.1.2. Solar Energy Sub-Sector

As the UN SDGs (United Nations Sustainable Development Goals, 2015) follow global strategies to solve many of the world's challenges, such as climate change and working to preserve our oceans and forests, the utilization of clean and renewable energy sources is becoming far more important. One of the fastest developing renewable clean energy sources is solar PV energy systems which can be available in most areas of the world. Indeed, the international energy agency 2014 technology roadmaps for solar photovoltaic energy and for solar thermal electricity concluded that solar energy could surpass fossil fuels, wind and hydro by 2050 to be the world's largest energy source. This is because generating electricity from solar energy using PV systems has become very widespread; and solar PV modules have become more affordable, more accessible, and therefore the most predominant renewable energy source globally. Indeed, the competition between the countries to employ solar PV modules technologies indicates the importance of utilizing solar energy system and the size of its market and industry. In 2016, India commissioned the Kamuthi solar power project, the world's largest solar plant. This solar plant consists of 2.5 million solar modules with generating capacity of 648 MW and it can generate nearly 20% more energy than the former largest solar plant in California (Adani Green Energy Ltd., 2019). The main aim of this research study is to improve the reliability of the PV modules which their market is massively increasing and facing more challenge with the system lifetime. This research also directly supports minimum two of SDGs (namely: affordable and clean energy, and climate action).

In general, there are two main techniques for absorbing energy in the solar energy systems used for generating electrical power. The first technique is concentrated solar power (CSP), which is based on the heating up a particular place by using the focused sunlight. CSP system uses mirrors/lenses to reflect and focus a large area of sunlight onto a receiver connected to a power generator unit which converts heat to electricity. Solar PV module is the second and most predominant technology, and is now widely accepted as a viable renewable energy technology. The solar PV energy harvesting technique is based on the transformation of sunlight into electrical current through the photoelectric effect; in which a photovoltaic substance (semiconductor material) absorbs photons of light and then releases electrons. The flow of the free electrons through the circuit connecting the semiconductor cells, produces a direct current (DC) power which can then be converted by an inverter into the alternating current (AC).

1.1.3. Solar PV Cell

Solar PV cells have been improving in efficiency and dropping in price in recent years, and are therefore becoming more common and economically viable. Similarly, the innovative developments in solar PV manufacturing process and the PV cell/panels interconnection design/configuration has resulted in significant savings in the expensive materials used in the manufacturing process (e.g. solder, silver and silicon). It is mostly this reduction in the use of expensive materials and the simplification of the manufacturing process that has contributed to the associated drop in the solar PV modules production costs and the reduction in the cost for generating a unit of electricity. For example, it is reported that among all renewable energy sources, solar PV exhibited the highest reduction in cost between 2019 and 2020. Indeed, the cost of solar PV cells is reported to have dropped globally from $378 USD/MWh in 2010 to $68 USD/MWh in 2019 (82 % drop). For comparison, the CSP system was the second in ranking with a 47% reduction in cost between 2019 and 2020, whilst in third place, onshore wind costs fell 40% (IRENA, 2020).

As the cost of solar PV cells drops, it is widely expected that solar energy will become the cheapest source of electricity in many parts of the world over the next two decades. According to the International Renewable Energy Agency (IRENA) report, solar PV cell will become the second-largest power generation source by 2050 (just behind wind power) and will be the catalyst for the transformation of the global electricity sector, generating some 25% of total electricity needs globally (IRENA, 2019). In addition, analysis of the capacity of each sector of renewable energy sources shows that the solar PV cell sector is growing significantly faster than the other sectors. Indeed, worldwide solar PV installation capacity had reached 223 GW by the end of 2015 (Ishii & Atsushi, 2017), and the solar PV capacity has increased to 621 GW in 2019 and 760 GW in 2020. Table 1 shows the energy capacity of the different sources of the renewable energy for the years 2019 and 2020 (IRENA, 2020).

Table 1: Capacity of different renewable energy sources in 2019 and 2020 (IRENA, 2020).

	Renewable Energy Source	***2019***	***2020***	***Unit***	***Growth%***
	Renewable power capacity (including hydropower)	2581	2838	GW	9.96
	Renewable power capacity (not including hydropower)	1430	1668	GW	16.64
💧	Hydropower capacity	1150	1170	GW	1.74
☀	**Solar PV capacity**	**621**	**760**	**GW**	**22.38**
✇	Wind power capacity	650	743	GW	14.31
🍁	Bio-power capacity	137	145	GW	5.84
♨	Geothermal power capacity	14	14.1	GW	0.71
☀	Concentrating solar thermal power (CSP) capacity	6.1	6.2	GW	1.64
💧	Ocean power capacity	0.5	0.5	GW	0.00

In addition to the lower costs for installation and operation, the recent increase in global popularity of solar PV modules can also be linked to increased governmental level support in form of tax credits, tax deductions, and other forms of subsidy that have been used to enhance the uptake of this technology. Indeed, the International Energy Agency 2020 World Energy Outlook (Birol, 2020) showed that solar energy has become the new king of electricity; reporting that with sharp cost reductions over the past decade, solar PV is consistently cheaper than new coal- or gas-fired power plants in most countries and that solar projects now offer some of the lowest-cost electricity ever seen.

1.1.4. Crystalline Silicon (c-Si) Solar Cell Technology

Although, several solar PV cell technologies and innovations for harvesting from sun light have been introduced by industry and researchers over the years, more innovative technologies are expected to enter the market in the future as the drive to improve solar PV module efficiency and reliability continues. The solar PV cell technologies can be classified into two main categories, namely Thin-Film (TF) solar cells and c-Si solar cells. The TF solar cells are the second generation PV cells, which uses thin-film photovoltaic materials in form of layers which are laid on substrates (mostly made of plastic, glass, ceramic or metal). TF solar cells are very lower in weight and are more flexible due to the very low thickness of the layers (thickness ranging from a few nanometres to tens of micrometres). The main TF solar cell technologies are Cadmium Telluride (CdTe), Gallium Arsenide (GaAs), Copper Indium Gallium Selenide (CIGS), and Amorphous Silicon (a-Si) (O. Ogbomo, et al., 2017).

The c-Si solar cell is the first generation of the solar PV cell to convert the incident light from sun to the electricity current; and they are well-known as commercial version of solar PV cell. The c-Si solar cells are the crystalline forms of silicon which can be used in form of mono-crystalline silicon cell (a continuous crystal, and also known as single-crystal silicon) or poly-crystalline silicon cell (consisting of small crystals). The thickness of the c-Si solar cells is up to 200µm thick. The measured cell conversion efficiency of mono-crystalline silicon cell is 26.7%, which is higher than the other solar PV cell technologies (Green, et al., 2018). However, in comparison with the poly-crystalline cells, the process for manufacturing the mono-crystalline silicon cells is expensive due to the ingot-growth techniques and the required purity of them (Sangster, 2014). Thus, the high price and complicated manufacturing process of mono-crystalline silicon cells are the main reasons to drop their share in the world solar PV market, as it is reported that the production of mono-crystalline silicon cells decreased from 38% of the market in 2011 to 36% in 2014. However, popularity of poly-crystalline silicon cell is still increasing, as its market share is increased from 48% in 2011 to 56% in 2014. However, the c-Si solar cells have over 90% of the market and are the most popular solar PV cell technologies (D. Lee & U. Ebong, 2017).

In this study, the focus is on the reliability of the PV module ribbon interconnection (i.e. PV module solder joint interconnections) used for connecting the c-Si solar cells.

1.1.5. Problem Context

It is widely known that over 40% of PV module failures are linked to PV module interconnection failures (McCluskey, 2010). Despite the global popularity and widespread use of solar PV modules, improving the performance and reliability of PV modules remains a key challenge for the solar PV manufacturing sector, as manufacturer strive to satisfy their products' lifetime warranties. To ensure that solar PV modules have a long service life and can meet the PV manufacturer’s warranty, the solar PV modules need to have high reliability. Indeed, in order to grow the global share of electricity generation of solar PV systems from the current 3% (IEA, 2021) to the projected 25% by 2050, there is an urgent need for improving the reliability of solar PV modules, which have been reported to fail due to adverse operating conditions such as thermal cycling, damp heat and UV exposure. For example, thermal cycling can cause PV module solder joint interconnection thermal failures and it can generate cracks in the solar PV cells. Solar PV module manufacturers typically provide two warranties: a performance warranty which guarantees 90% of original power output after 10 years and 80% of original output of at 25 years; and an equipment warranty which guarantees their solar PV module will have a minimum of 10-12 years operation before failure.

The ribbon interconnection is a key PV module component; because poor interconnection reliability can lead to solar PV module failure. Furthermore, the interconnection design affects the shadowing on the solar PV cells, and the associated partial shading loss which reduces solar PV module performance and efficiency. Indeed, the objectives of solar PV modules manufacturers is always achieving the optimal PV module ribbon interconnection design that will give the highest possible levels of solar PV module efficiency whilst at the same time improving the PV module reliability. However, during the lamination process and also the service life, the solder joints exhibit high strain energy values due to the coefficient of thermal expansion (CTE) mismatch of the PV module materials. The induced thermal strain energy in these solder joints serve as the catalyst and sources for the thermal crack initiation and progression associated with the PV module ribbon interconnection failures. Hence, there is an urgent need for this study, which will provide a better understanding of the effect of the PV module interconnection design on the solder joint failure modes and consequently, and the associated effect of the PV module interconnection configuration on the PV module interconnection reliability. This programme has addressed this urgent need.

1.1.6. PV Modules Structure

The solar PV module is generally made up of four different materials: glass, metals, polymers and the semiconductor. The exploded view of the components of the conventional PV module is presented in Figure 3 below. This shows that the glass is used for front cover and it is bonded to the main metallic frame. The active solar cells including silicon wafers (semiconductor), the fingers, connection pads (silver layers printed on the silicon wafers), string connectors (interconnections) and cables are embedded in polymer encapsulation material which provides adhesion and structural integrity between the solar cells, the top surface and the rear surface of the PV module. Ethyl Vinyl Acetate (EVA) is the most commonly used encapsulation material. The back sheet (which can be either polymer or glass) is used to cover the bottom side of the PV modules. The Anti Reflective Coating, ARC, (in combination with surface texturing of the silicon) can also be applied in the silicon wafers to reduce the reflection and the glare from the cell and therefore improves the light transmittance which helps to increase the overall efficiency of the PV module (Dricus, 2011) and (Honsberg & Bowden, 2018).

The figure is redacted for the public view due to lack of permission of the copyright holder.

Figure 3: Schematic view of conventional PV module (Wahid, 2015).

1.1.7. Solar PV Cell Interconnections

The ribbon interconnections are perhaps the most critical part of the solar PV module assembly, and they are used for linking the solar cells and for interconnecting to the external circuit (and the ribbon interconnections are in turn joined to the solar cells using solder joints interconnections). This means that the failure of the solder joint and the associated ribbon interconnection can adversely affect the performance and reliability of whole solar PV module. Maximum power generated by a c-Si solar cell can only produce a voltage of 0.5V which is far less than the energy required to feed into the conventional electrical power networks. Therefore, individual cells need to be connected to produce higher voltages (Wiese, et al., 2010). Figure 4 shows the four main configurations that can be used for connecting solar PV cells within the PV, namely: series-parallel (SP), bridged-link (BL), honey-comb (HC) and total-cross-tied (TCT) configurations. Although the SP interconnection configuration is known to suffer the highest Partial Shading when compared with the other three configuration; the SP is still the simplest and the most commonly used configuration technique due to its inherent simplicity and associated wiring time, and low costs due to fewer interconnections and wiring (Pareek, et al., 2017) and (Ramabadran & Mathur, 2012).

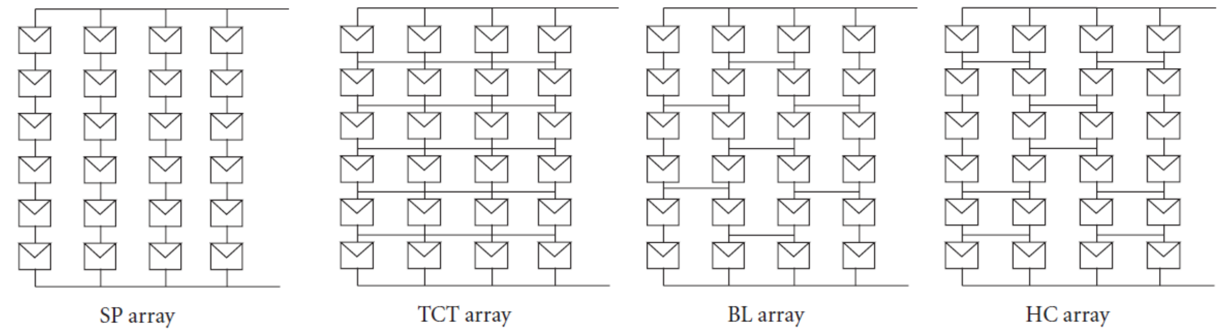

Figure 4: Schematic diagrams of different solar photovoltaic array configurations (Ramabadran & Mathur, 2012).

The front-to-back cell interconnection technique is the most popular method for connecting the neighbour crystalline photovoltaic cells in the PV modules, in which the PV module positive and negative contacts are built to allow the connection to the rest of PV system. Figure 5 shows the schematic cross-sectional view of the ribbon interconnection (using the SP configuration) between cells in a PV module which has been assembled using the front-to-back interconnection method to connect the cells via solder joint materials. However, there are also several technologies that have been introduced as replacement for the conventional front-to-back assembly technique. For instance, an interconnecting method by overlapping photovoltaic cells technique instead of using the ribbon interconnections is suggested to connect cells without any gaps between them (see Figure 6) and it is shown that this design can get higher power output per module area and may also lower production costs (Summhammer & Halavani, 2016). Another emerging interconnection technology is the Metal Wrap Through (MWT) cell technique. With MWT, there is no need for use of solderable busbars on the front metallization and the current transfers to the rear side through metallized holes in the wafer and on the rear side the neighbour cells are interconnected by ribbons (see Figure 7). Although using these techniques results in improving the cell efficiency by minimizing shading losses, less cell-to-module current losses and low thermomechanical stress in manufacturing process (Thaidigsmann, et al., 2011) and (Eitner, et al., 2012), the front-to-back cell interconnection method is still the most popular as the newer techniques are yet to establish reliability track record and also due to the high costs required to implement major changes in the manufacturing process used for assembling the conventional interconnection (T. Zarmai, et al., 2015).

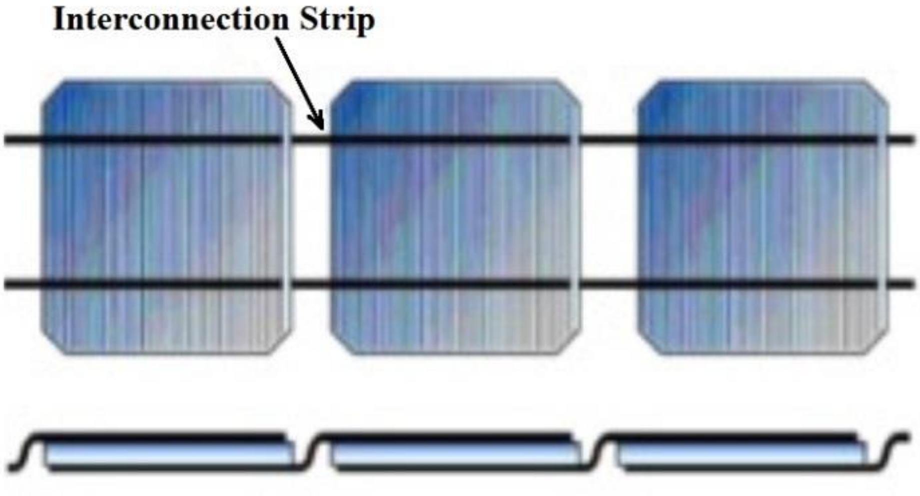

Figure 5: Schematic views of the front-to-back c-Si cell interconnection technique using two CR interconnections (Mat Desa, et al., 2016).

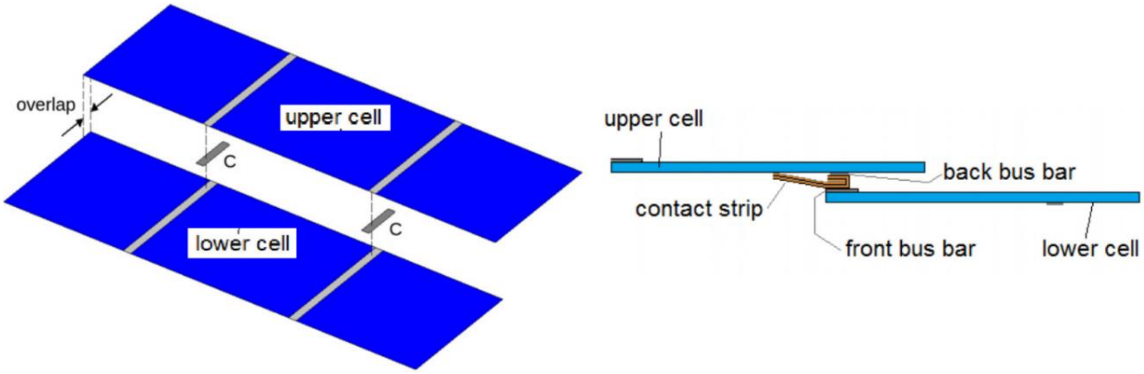

Figure 6: Schematic view of the overlapping photovoltaic cells interconnecting technique. 3D view (left) and side view of connection scheme of two cells (right) (Summhammer & Halavani, 2016).

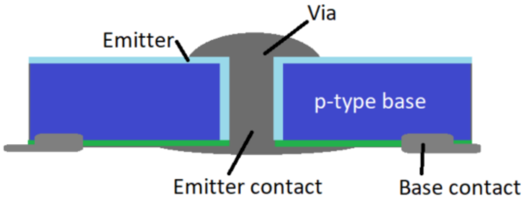

Figure 7: Schematic view of the MWT solar cell concept (Domínguez, et al., 2012).

1.1.8. Overview of the PV Module Reliability

One of the main challenges to further deployment of the solar PV module technology is that of improving the reliability and reducing early failure rates as this is the key to meeting manufacturers' lifetime warrantees and achieving optimal performance for specified operating conditions. Unfortunately, the existing standards for PV module design and qualifications (such as IEC 61215/61646), and for PV module construction and testing for safety qualification (such as IEC 61730), are not intended to be a full guarantee for the whole lifetime of a module (Ferrara & Philipp, 2012) and (Deng, et al., 2005). For example, the experimental investigation on the thermomechanical fatigue resistance of a lead-free solder joint (Sn-Bi) used in PV module MBB interconnections indicates that the accelerated thermal cycling tests suggested in the standard such as IEC 61215 may produce misleading results that are aimed to help with the interconnection designs (Spinella & Bosco, 2021). Despite these limitations in the existing standards, PV module manufacturers continue to provide a guarantee of up to 20 years for the quality of silicon PV modules currently being produced (Honsberg & Bowden, 2018). PV module reliability is particularly dependent on the quality and integrity of the manufacturing process of the PV module interconnection; as the PV module interconnection failure is known to account for around 40% of all solar PV module failures (McCluskey, 2010).

Better understanding of the factors that affect PV module reliability is crucial for predicting their expected lifetimes, especially in various climatic conditions/zones where the solar PV modules can experience different environmental stressors. This fundamental understanding is key to providing more realistic manufacturers guarantees for PV modules. Previous studies, such as that by Jordan, et al. 2017, have attempted to estimate the approximate lifetime of PV modules based on the field data collected from different solar PV installations for varying periods of time. Their work focused on the use of the nonlinear changes in degradation rates and the associated reduction in PV module performance to quantify the long-term PV module reliability. Their work showed that the degradation rates based on the assumption of linearity may not be sufficiently accurate and consequently underlying this nonlinear assumption is the suggestion that estimations can never be accurate at the beginning of the module's life cycle and therefore these assumptions will have a significant impact on the warrantee and manufacturers price (C. Jordan, et al., 2017). Their results confirm the need for enhancing and improving the existing standards for PV Module Design and Qualifications and for PV Module Construction and Testing for Safety Qualification to ensure that they are fit for purpose and can provide accurate PV Module reliability predictions and the associated realistic manufacturers' guarantees (Kelly & Sugathan, 2017).

Enhancing and improving the existing PV Module standards requires better understanding of the impact of the types of PV module degradation and failure modes as well as the impact of the different interconnection configuration/design, and how the different configuration/design can help to reduce PV module failure rates and the associated long-term reliability. This is the focus of this study.

1.1.8.1. Degradation and Failure of PV Modules

The degradation and early failure which are known to affect PV modules components/parts, adversely impacts on the PV module performance, reliability and operating life; and these have been the subject of studies over the last two decades. For example, a number of studies have been carried out on the certified PV modules, to help identify their potential failure modes. The focus of most of these studies has been on the analysis of the field data collected from different solar PV installation for varying periods of time. The PV module degradation modes such as hot spot heating, encapsulate degradation and glass cover breakage are known to lead to partial cell shading; which adversely affects the PV module performance (thus reducing their power output and the energy conversion efficiency of the PV module). However, some other parts of the PV module such as junction box are also known to be of reliability concern.

Although it is possible to utilize the PV module interconnection design and configuration arrangements to mitigate the partial shading effects on the module performance (Bidram, et al., 2012) and (Pareek, et al., 2017); the main challenge remains that of reducing the incidence of (and where possible eliminating) the PV module failure modes, such as cracks and corrosion that are known to occur in different PV module assembly materials. These failure modes can accelerate the degradation rate and negatively impact on the performance of the PV modules. It is widely believed that the thermomechanical stress associated with the thermal cycling loads is the major reason for the cell bowing and the crack failure in PV modules (Honsberg & Bowden, 2018). Indeed, the thermal stress and strain resulting from the PV cell operation under high temperature cycling conditions; and the high temperature manufacturing processes such as the lamination of the PV module can lead to crack initiation and crack propagation in both silicon wafers and the PV module interconnection solder joints.

1.1.8.2. Crack in Solar Silicon Wafers

The fracture and crack analysis in solar silicon wafers have been the subject of several studies, focused on understanding the effect of both service condition and manufacturing process on premature PV module failure (Shin, et al., 2018). It is widely believed that the main reason for cracking in PV cells subjected to thermomechanical loading is the intrinsic properties and structure and of the silicon wafers. Firstly, the silicon wafers in the PV module experience high tensile stress during exposure to high temperatures; and as silicon has lower CTE (coefficient of thermal expansion) compared to the other PV cell materials and this causes stress in the connection between the silicon wafers and ribbon interconnections. Secondly, the tensile strength of silicon wafers is between 100MPa and 200MPa and this is much lower than its compressive strength (~3000MPa). This means that the silicon wafers have a higher probability of cracking when subjected to tension loading compared to when they are subjected to compression loading. In addition, it has also been reported that the slicing of silicon wafers (part of the manufacturing process) is associated with the increase in the residual stress which can lead to the formation of surface cracks in the wafers, and the significant reduction in poly-crystalline silicon wafer strength (Echizenya, et al., 2011).

The importance of crack failure in solar silicon wafers is recognized in several studies as it is widely reported that the crack results in significant reduction of in both PV module performance and their long-term reliability. The effect of cell cracking distribution due to mechanical loads before final installation on the performance of PV modules have been studied by Köntges, and their results show that the crack orientation determines the criticality of the crack (Köntges, et al., 2011). Similarly, experimental studies on PV modules subjected to mechanical/thermal loading shows that the crack in crystalline solar cells mostly initiated at the beginning and the end of busbar (Schneider, et al., 2006); and that the crack grows along the busbar (Sander, et al., 2011) and in the extremely poor condition, the cracks near to busbar can negatively affect the metal connections on the cell and undermine the PV module performance.

It has also been reported that cell cracking may not only be caused by the thermomechanical loads, but it could be also formed due to different loadings conditions (for instance, the vibration and local lifting loads experience during installation). The "latent cracks" that are known to occur during PV module installation, but are unfortunately not detectable through manufacturing inspection, appear sometime later are good examples of this problem (Honsberg & Bowden, 2018).

1.1.8.3. Crack in Solder Joint of PV Module Interconnection

The ribbon interconnection which collects the electrical currents from individual PV solar cells is a key PV module component since their failure can adversely affect the reliability and the performance of PV modules. Solder materials are typically used for joining the ribbon interconnections to the PV solar cells. These solder joint materials represent the critical part of the PV module assembly due to their inherent weak mechanical strength which results in early micro-cracking and deboning. For this reason, solder joint failure is known to be the major source of early PV module solder joint interconnection failure (McCluskey, 2010). Crack is the main reason for the failure of PV module solder joint interconnections during the lamination process and during the lifecycle of the module. Indeed, after cell tabbing and ribbon interconnection soldering stage in the PV module manufacturing processes, the module will be under the lay-up and high temperature lamination process (up to 150°C) to melt, cure and develop a network of EVA. Figure 8 shows the flow chart for manufacturing process of the conventional PV module.

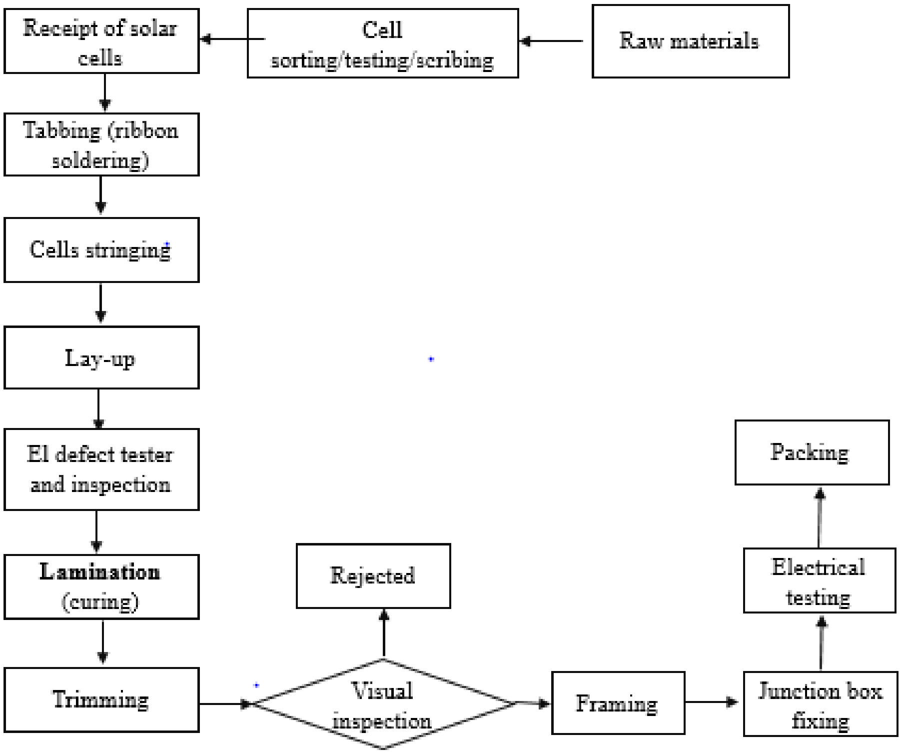

Figure 8: Conventional PV module manufacturing process flow chart, adopted from (Rashedi & Khanam, 2020) and (Satpathy & Pamuru, 2020)

During the lamination process, the solder joints exhibit high strain energy accumulated and this leads to the nucleation of cracks in the solder joint boundaries between the silicon wafer and the ribbon interconnection (Pander, et al., 2011) and (Song, et al., 2019). Also, with thermal cycling during the PV module operation, the associated creep strain energy increases and can accelerate the failure of the solder joints (Ogbomo, et al., 2018). It has been shown that with high temperature cycling of PV modules (such as those experienced by PV modules during high temperature climate operations), the micro-cracks initiated in the solder joint can propagate through the connecting layer and ultimately it can lead to PV module failure. This is particularly true with lead-free solder joint materials (which is now the preferred environment-friendly joining material), as they have higher potential for exhibiting micro-cracks due to their lower fracture strength and higher thermo-mechanical stress levels when compared to tin-lead solder alloys (Pander, et al., 2014).

1.1.8.4. Corrosion

In hot and humid weather conditions, corrosion related cracks in long-term field-aged PV modules are one of the primary concerns because of their effect on the reliability of PV module solder joint interconnections. This is especially true for solder joints made with lead-based solder materials such as the popular 62Sn36Pb2Ag (which has good solderability and low melting temperature due to the Ag content; but suffers from galvanic corrosion). Indeed, some reports show that circa 45% of observed field failures in PV modules are related to corrosion failures (Wohlgemuth, 2008) and (Campeau, et al., 2013). The results of X-ray spectroscopy on the 18 years old PV modules in hot-humid climate has shown that there is significant corrosion damage in Ag metallization due to presence of acetate (which is a product of hydrolysis within EVA after diffusion of moisture inside the module during aging). This type of corrosion can accelerate the mechanical fatigue crack creation between Ag bus-bar and Cu ribbon and can decrease performance and power output of the module by increasing series resistance strings (Zhang, et al., 2018). Operating under higher temperatures conditions can also serve to accelerate the chemical reactions associated with the corrosion of metallic components of PV module leading to failure. In addition, corrosion can also result from the use of polymers additives, which can result in the formation of corrosive substances such as acetic acid (CH_3COOH), which cannot evaporate because of a non-permeable back sheet (Ferrara & Philipp, 2012). However, the addition of certain sacrificial metals such as Aluminium can provide a practical solution to this corrosion challenge and can significantly reduce the galvanic corrosion rate (Kim, et al., 2014). Indeed, this solution is implemented in most of the new silicon PV modules (a thin layer of Aluminium is used to cover the rear surface of silicon), which not only helps to reduce the adverse corrosion effects, but also helps to increase the mechanical strength of the cells as well as improving the PV module reliability.

1.2. Motivation for the Study and Research Questions

The motivation for this study is to investigate both conventional and new PV Module interconnection configurations that can help to improve the module reliability. Particularly, it is urgent to investigate the failure of new PV module interconnection designs as they are new technologies which can improve the PV module power output by increasing the incidence of light onto the solar PV module.

The design of the PV module parts involves achieving the best performance and the highest reliability and at the same time, saving the material consumptions and keeping the manufacturing cost low. Indeed, several performance parameters such as fill factor and power output of PV modules under damp heat-exposed and UV-aged tests are surveyed by researchers to find the effect of different designs and materials on the performance of the PV modules (Wang, et al., 2013).

Numerous experimental and numerical works have been performed to design the PV module parts in order to achieve the best performance and the highest reliability and at the same time, saving the material consumptions and keeping the manufacturing cost low. For example, Wang, et al, surveyed several performance parameters such as fill factor and power output of PV modules under damp heat-exposed and UV-aged tests to find the effect of different designs and materials on the performance of the PV modules (Wang, et al., 2013).

The design of the PV module interconnections has attracted more attention compared to the investigation on other PV module components, as it has been reported that over 40% of PV module failures are linked PV module interconnection failure (Wohlgemuth, 2008) and (Campeau, et al., 2013). Similarly, recent studies have shown that the introduction of new interconnections designs have been beneficial for improving the efficiency of PV modules and for reducing the use of expensive silver materials (Schneider, et al., 2014), (Braun, et al., 2013) and (Rendler, et al., 2017).

The focus of this study is on the investigation of the impact of PV module interconnection designs on their thermo-mechanical reliability and the use of the FEM simulation modelling approach to facilitate the design for reliability validation of different ribbon interconnection configurations to improve the long-term PV module reliability. To this end, the new and conventional interconnection (CR) in PV module are considered to find the effect of changes of the dimensions on the thermal failure of the PV module solder joint interconnections (see Figure 9). The study uses the finite element method (FEM) based techniques to simulate the crack initiation and growth in the solder joint of different PV module interconnections designs during high temperature manufacturing process and also to simulate the creep-fatigue behaviour of the PV module solder joint interconnections operating under thermal cycling loads. The study explores several important research questions relevant to the thermo-mechanical reliability of the of PV module interconnection. The list of the research questions explored in this study include the following:

- What is the effect of ageing and cell temperature rise on the PV module solder joint interconnections failure and packaging reliability?
- What is the effect of thickness/width of the PV module solder joint interconnections and bonded materials on the degradation and failure of the interconnection?
- What is the effect of the Multi-Busbar (MBB) solder coating non-homogeneity on crack initiation and propagation of the solder joints?
- How can we predict the life cycle reliability of the solder joints for different PV module interconnection designs?

Figure 9: Schematic view of the cross section of CR interconnection with showing the questioned thickness/width of solder joints and bonded materials.

1.3. Aim and Objectives

The aim of this study is to build and validate failure analysis and reliability prediction models for solar PV module interconnections. The study addresses the concerns associated with the reliability and failure one of most widely used renewable energy technologies. It investigates the main failure modes of PV module interconnections and develops models for predicting their reliability; and it develops a virtual reliability qualification process for the assessment of the life expectancy of PV module interconnections under anticipated life cycle loading conditions. The need and urgency for this study is demonstrated by the fact that the solar PV module technology is under development; and the premature/early failure of PV module installations continues to be of major concern worldwide. Although some previous studies on PV module failures have been in the literature, there are very few reports on the failure analysis and reliability prediction models for PV module interconnections. This crack analysis differentiates work from what has been reported in the literature, and represents the state of the art.

The main objectives of this study are to:

a) Study the effect of temperature on PV module interconnections and packaging reliability
b) Study the cumulative and residual effects of high temperature PV module manufacturing processes on PV module interconnection lifecycle and to determine appropriate values for operating temperature damage.
c) Investigate the effect of the thickness of bonded materials in PV module interconnections on solder joint failure during the high temperature lamination process and service life condition.
d) Investigate the effect of the Multi-Busbar (MBB) solder coating non-homogeneity (on crack initiation and progression in the solder joints.
e) To investigate the effect of new and conventional PV module interconnection configuration on the thermal failure of the PV module solder joints and to develop the predictive model for estimating their life cycle reliability.

1.4. Scope of Research

The solar PV energy generation is the focus of this study, and more specifically, the interconnection reliability of solar PV modules manufactured with c-Si cells. Although, there has been a lot of R&Ds, the technology for harnessing solar energy using PV modules is still developing and the failure of PV module installations continues to be of major concern. The study will investigate the thermal failure modes of the PV module solder joint interconnections. The thermal failure of conventional and new PV module interconnection desgins with solder joints is studied to investiagte joint failure and long-terms reliability. It also investigates the conventional and new PV module ribbon interconnection desgins, widely used in industry. These interconnection technologies are widely used for interconnecting the silicon wafers to reach enough voltage and power output.

Through a new methodology, it addresses the modelling of the impact of different PV module interconnection configurations and designs on the crack initiation temperatures and crack growth rates during the lamination process in the PV module manufacture.

During the manufacturing of PV modules, the interconnections are made by the soldering of the cells, in which flat copper ribbons are soldered to each side of the cell to carry out current, and the cells are electrically connected in series to form strings of cells. The connected cell will be protected by laminating the encapsulation materials and the glass and the back sheet layers. The lamination process of the PV modules is a high temperature process (up to 150°C) which can induced high thermal stress/strain in the solidified solder materials; and it results in micro-crack initiation in the solder contacts and the failure of the PV module interconnection. Indeed, the ribbon interconnection failures have been linked to the thermal cracks which are initiated in the solder joint material during the high temperature lamination process; and then the crack propagation associated with the thermal cycling of the ribbon interconnections under higher than ambient temperature PV module operating conditions.

In fracture mechanics, numerical investigations and finite element simulation have been extensively carried out to predict crack growth path and rate. For the first time, this research has chosen the extended finite element method (XFEM) to study the solder joint of PV module interconnection in terms of finding the crack initiation, propagation and path. The XFEM is one of the new numerical approach which has been widely applied to a variety of crack problems involving discontinuities, singularities and complex geometries. A key advantage of the XFEM is the capability to determine the crack initiation and to track the crack path without any needs to update the meshing system during the analysis (Belytschko, et al., 2009). This capability provides a simplification of the modelling of discontinuous phenomena for solving the fracture mechanics problems such as the case studies in this research. Furthermore, the literatures showed that the XFEM technique can accurately find the answers for a wide range of fracture mechanics problems such as failure due to high amplitude loading and cycling conditions. For example, an investigation on the failure of the turbine discs and blades subjected to cyclic loading at high temperature during service showed that the XFEM was greatly capable to predict the crack growth and path results which have been found by experiments (Farukh, et al., 2015).

The research has also focused on the creep-fatigue failure of the solder joints in PV module interconnection subjected to the thermal cycling loads to determine the number of cycles to failure. For this, the Developed Morrow Energy Density model is used, and then a new generic exponent factor using the Coffin–Manson–Arrhenius model is defined to estimate the lifetime for different thermal cycling conditions. The research also combines the numerical results of XFEM and creep-fatigue investigation to determine the failure lifetime of PV Module interconnection designs.

It should be noted that this research encountered a number of logistical challenges due to the lack of access to the laboratories and experimental support during the Covid-19 long-term lock-downs and travel restrictions in the UK; in addition, the irregular access to high performance computing facilities also limited the numerical investigation work.

1.5. Contribution to Knowledge

This study has used the FEM simulations to investigate the thermal failure of the PV module solder joint interconnections, and then to recognize the best PV module interconnection configuration in terms of thermo-mechanical reliability. The conventional, the LCR and the MBB interconnections used in the PV modules, were modelled using FEM simulation with considering the details of material behaviour such as nonlinearities of material properties, temperature dependency and creep-fatigue response. For this, a Python code in ABAQUS 2019 software package was scripted which can facilitate the simulation to generate the FEM models (over 350 simulations were investigated). The investigations of models include the thermal failure of the PV module solder joints interconnection during manufacturing process (i.e. high temperature lamination process) and also during different lifecycles of the module. The key contributions are:

1. For all studied PV module interconnection designs, the Extended Finite Element Method (XFEM) technique was implemented to find the crack initiation temperature, crack location, crack propagation direction, and crack growth rate during the lamination process. It was found that in all configurations of the PV modules interconnection, location for the crack nucleation is at the IMC interface layers of solder joints boundaries, and the crack propagates in the shear direction.
2. The XFEM technique also was used to investigate the effect of the solder coating non-homogeneity in MBB interconnection design (due to the manufacturing error) on the cracking temperature; and the results show that the crack initiation temperature is most affected by the direction of solder coating non-homogeneity (up to 21%).
3. The number of cycles to creep-fatigue failure for each PV module interconnection design was determined using the Morrow Energy Density model (with using of the Hyperbolic Sine creep law); and then the Coffin–Manson–Arrhenius approach is used as a handy formulation that can be applied easily to determine the solder joint’s creep-fatigue life during different lifecycles of the module. For the Coffin–Manson–Arrhenius approach, the generic exponent factor was determined to be -1.8.
4. The optimum dimensions of the conventional, LCR and MBB interconnections were found by comparing the results of the XFEM and creep-fatigue investigations of the simulated cases studied in this work. It was also found that the XFEM findings are consistent with the results obtained for creep-fatigue life estimations. It was found that the MBB interconnections can provide more creep-fatigue age compared to the LCR and the CR interconnection designs (up to 15%); and the most optimum configuration for the MBB interconnection is with 15 ribbons of the 276µm copper diameter, with 20µm solder thickness and with 20µm silver-pad thickness.

5. The results of creep-fatigue investigation also showed that for all cases studied, the maximum temperature of the cycling load significantly impacts the creep-fatigue lifetime; as by increasing the maximum temperature from 50°C to 60°C, the creep-fatigue lifetime decreased by 50%.

1.6. Publications from the Research

Six peer-reviewed journal papers have been published from this study (listed 1-6 below). In addition, two further papers (listed 7-8) have also been published from related work on the modelling and simulation of material and components in similar size which are not included in this thesis. The FEM methodology used in this Ph.D. study was also used by the candidate in simulation of micro-structure of Through Silicon Vis (TSV) used for 3D electronics packaging and interconnections reported in papers 7-8.

1. **A.E. Majd** and N.N. Ekere, (2020), "*Crack Initiation and Growth in PV Module Interconnection*", Journal of Solar Energy, Vol. 206, pp. 499-507. DOI: 10.1016/j.solener.2020.06.036.
2. **A.E. Majd** and N.N. Ekere, (2019), "*Numerical analysis on thermal crack initiation due to non-homogeneous solder coating on the round ribbon interconnection of photo-voltaic modules*", Journal of Solar Energy, Vol. 194, pp. 649–655. DOI: 10.1016/j.solener.2019.10.092.
3. **A.E. Majd** and N.N. Ekere, (2020), "*Study of High Temperature Crack Initiation and Growth in Light Capturing Ribbon (LCR) PV Module Interconnection*", Journal of Advanced Materials Science and Technology, Vol. 2(2). URL: http://ojs.omniscient.sg/index.php/amst/article/view/998.
4. **A.E. Majd** and N.N. Ekere, A. R. Darvazi, (2021), "*Investigation of creep-fatigue life in Solar Photovoltaic Module Interconnections*", under review.
5. **A.E. Majd** and N.N. Ekere, A. R. Darvazi, (2021), "A Comprehensive Review of Photovoltaic Module Interconnection Design and Failure". under review.
6. **A.E. Majd** and N.N. Ekere, A. Rahmati Darvazi, (2021), "*Creep-fatigue Lifetime Estimation of Efficient Photovoltaic Module Ribbon Interconnections*". under review.
7. **A.E. Majd**, I.H. Jeong, J.P. Jung, and N.N. Ekere, (2021), "*Cu Protrusion of Different Through-Silicon-Via Shapes under Annealing Process*", Journal of Materials Engineering and Performance 30, pp. 4712–4720. DOI: 10.1007/s11665-021-05775-4.
8. I.H. Jeong, **A.E. Majd**, J.P. Jung, and N.N. Ekere, (2020), "*Electrical and Mechanical Analysis of Different TSV Geometries*", Metals 10(4), p. 467. DOI: 10.3390/met10040467.

1.7. Research Programme and Structure

A first part of this study involves a review of previous published works, including journal/conference papers, books, reports and websites in subject of the PV module technologies, challenges and progresses; and particularly in subject of the PV module solder joint interconnections. Reviewing the literatures has helped to understand the main challenges and to find the gaps in the present technologies and to answer the research questions of the study. For this study, the main reviewed topics are on the PV module interconnection designs and the failure of the PV module solder joint interconnections.

The recognized gaps illustrate that there are some important needs to study the cracking failure of the PV module solder joint interconnections which lead to improve the reliability of the PV module. This includes study on the crack initiation and growth in solder joints of different PV module interconnection during the lamination process and also includes the investigation of creep-fatigue behaviour of the PV module solder joint interconnections operating under service condition. Then a comparative study of the results for the failure of the solder joints is necessary to find the best designs in terms of the thermo-mechanical reliability issues.

The FEM is the approach taken to find the answer to questions on the failure of the solder joints. To simulate the crack initiation and growth in solder joints during the lamination process, the XFEM technique in ABAQUS 2019 is implemented; and to assure the accuracy of the results, the methodology is used to re-find the experimental results for the cracking failure from a published work. To achieve an easy way to update the FEM models, a Python code is scripted and the code is included all commands needed to be applied for finalizing the simulations. This code also includes different libraries for using material properties, importing the dimensions of models and changing other simulation steps such as meshing and load/boundary conditions. Also, this code enables the user to select the required analysis on the solder joints whether the XFEM analysis or creep-fatigue analysis is aimed.

Finally, the results of the simulation of different configuration of PV module interconnection for both XFEM analysis and creep-fatigue analysis are compared to find the best design in terms of thermo-mechanical reliability.

Figure 10 shows an overview for the research structure and plan that was followed throughout the study.

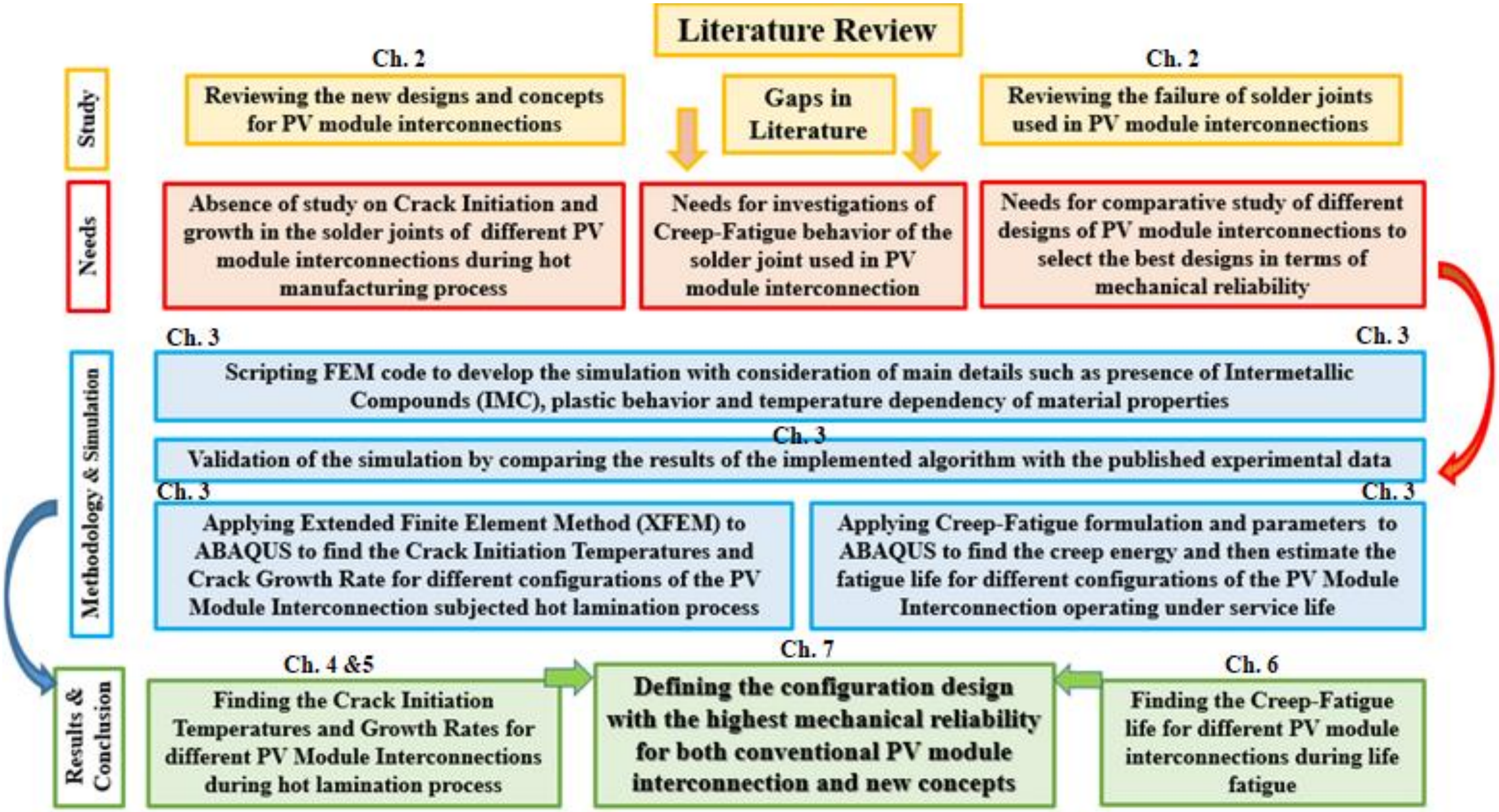

Figure 10: Overview for the research structure and plan followed throughout the research.

1.8. Thesis Outline

The thesis is made up of 8 chapters as follows:

Chapter 1 introduces the scope considered for this thesis with the topic of the failure of the PV module interconnections. Firstly, a background for the topic is presented which contextualizes the study and it shows the importance of this study for the challenges of PV modules reliability and particularly the failure of the PV module solder joint interconnections. Secondly, the chapter is followed by description of the research questions recognized for the issue which bases the objectives and methodologies used in this thesis. Finally, other section of chapter including, scope of research, research contributions and structure of the research are presented.

Chapter 2 presents a literature review on of the previous researches on the design and reliability of PV Module Interconnections and its solder joints. Chapter 3 presents the methodology used in this study for the investigation the PV module solder joint interconnections failure. This chapter depicts the details of the FEM used to simulate the crack analysis and creep-fatigue analysis for the PV module solder joint interconnections. Chapter 4 and chapter 5 present the crack investigations in the lead-free solder joint of the CR interconnections and the new PV module ribbon interconnection designs. Chapter 5 includes two main parts. The first part presents a comparison of the crack parameters in the solder joints between the Light Capturing Ribbon (LCR) and the CR interconnections. Also, the second part of chapter 5 presents the effect of geometrical parameters and the effect of solder coating non-homogeneity (out of centre value and direction) on the thermo-mechanical response of round ribbons used for PV module interconnections. For chapter 4 and chapter 5, the XFEM in ABAQUS 2019 is used to determine the micro-crack initiation temperature and location and also crack growth rate for the given joint designs during the lamination process.

In Chapter 6, the FEM simulation in ABAQUS 2019 is implemented to study the creep-fatigue behaviour of the lead-free solder joints for both conventional and new PV module interconnections. For this, the total dissipated energy is used to find the number of cycles to failure for each of the PV module solder joint interconnections under the test thermal cycling load. The exponent factor of Coffin–Manson–Arrhenius approach for the PV module interconnections is calculated and is then used to determine the solder joint's creep-fatigue life operating under thermal cycling conditions.

The discussion of the results introduced in chapter 4 to chapter 6 is presented in chapter 7. Chapter 8 presents a summary and conclusion of the study including the answers to the research questions, introduction of the selected configuration for the PV module interconnections which can meet the highest reliability without losing the efficacy of the module, suggestions and recommendations for future works.

Chapter 2

2. Literature Review

This chapter presents a literature review of the previous research on the designs and reliability of PV module interconnections using the front-to-back cell technique. The first focus of the chapter is on review of new designs for the front-to-back cell interconnections used in the SP array interconnected PV module. The second and main focus of this chapter is on study of the “crack” failure in the PV module solder joint interconnections, as it is known to be the main catalyst for PV module failure.

2.1. Introduction

One of the key components of the c-Si solar cells assembly is the PV module ribbon interconnection (i.e. the solder joint interconnections) between the solar cells. PV module interconnections are being used to connect the solar PV cells for producing higher voltages to feed energy into conventional electrical power networks. Failure of the PV module interconnections can adversely affect the performance and reliability of whole PV module. Ribbon interconnection failures have been linked to the thermal cracks which are initiated in the solder joint material during the lamination process; and creep-fatigue failure with the thermal cycling of the ribbon interconnections operating under high temperature conditions.

2.2. Ribbon Interconnection Designs

The ribbon interconnection (or strip interconnection) which is typically made of copper is used for collecting the power generated by the individual silicon cells in the conventional PV module. The ribbon interconnection is thus a very important component in the PV module assembly, since it serves as the mechanism for delivering the power generated to the output terminals (failure of ribbon interconnections adversely impacts on the performance of PV module and it reduces the power output).

In a solar PV cell, increasing either the width or number of the ribbon interconnections lead to decrease series resistance and it can be a merit for the whole module. However, using wider ribbons decreases the short circuit current due to more partial shading (with partial shading, one part of the solar panel generates lower amount of energy as compared to the other non-shaded part) and subsequently causes a bigger reduction in the power output, since power loss goes as the square of the current (M. Sachs, et al., 2009). Indeed, in the conventional solar PV module, the ribbons use about 2.3% of the cell’s surface and they reflect the incident rays from the sun. This reflection means losing more received energy and it causes a decrease in the short circuit current. Consequently, on one side, the configuration of the interconnection influences the shading on the PV cells and the partial shading loss reduces the performance and efficiency of PV modules. On the other side, solar PV module manufacturers are keen to achieve higher reliability products in order to match their offer of power output warranties of 25 years (with early and premature failures covered by the warranty and the free replacement of the solar PV module).

In most of the fabricated solar PV modules, the conventional (with rectangular cross-section) ribbon interconnection is being used as a front-to-back cell interconnection technique. However, some manufacturers are trying to do some rearrangements and physical changes in the conventional ribbon interconnections to increase both efficiency and reliability of the PV modules and at the same time, decrease the manufacturing cost. By now, several concepts for the ribbon interconnections and solar cell tabbing have been introduced to reduce the reflection rays from surface of the ribbons such as painting the ribbons with white pigments or using high number of small round ribbons (Muehleisen, et al., 2016). The investigation of the reliability of novel PV module ribbon interconnections is presented in Chapter 5 of thesis, and this focuses on the analysis of the crack initiation in the solder joints of two main new designs (namely: Light Capturing Ribbon, and Multi-Busbar Ribbon), in which, different configurations of these ribbon interconnections are considered to optimize the designs. In addition, Chapter 6 presents the creep-fatigue analysis of the solder joints used in these new designs and the estimation of their service life span. The recent innovations in the design of new and emerging PV module ribbon interconnections are discussed next.

2.2.1. Light Capturing Ribbon Interconnection

One of the innovative concepts for solar cell tabbing is the Light-Capturing/ Harvesting Ribbon (LCR/ LHR) design. This design has a grooved surface (with specific angles) to reflect more light back onto the cell surface (Schneider, et al., 2014). Figure 11 shows a schematic view of reflecting light back onto the cell by using Light–Capturing Ribbon with six grooves designed by Ulbrich Stainless Steels and Special Metals Inc. (Ulbrich, 2013). In comparison with the normal ribbon, the LCR increases the efficiency of a solar module and it brings more power gain and more short circuit current up to 2% (M. Sachs, et al., 2009).

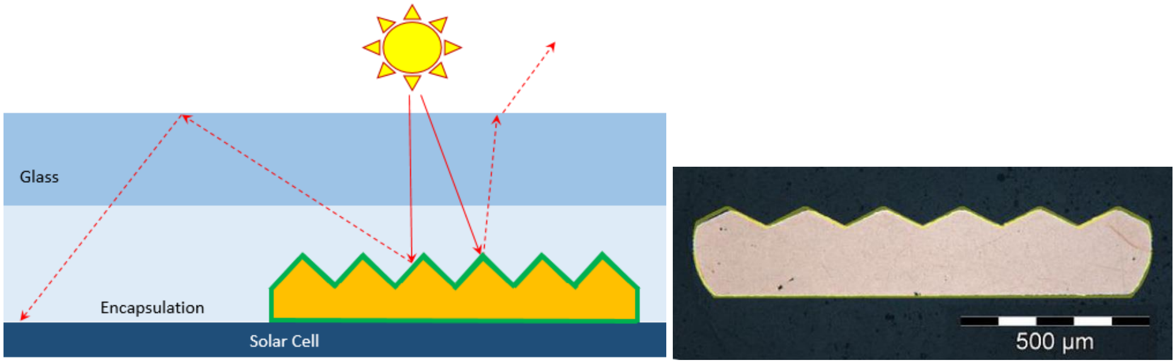

Figure 11: Schematic view of reflecting light back onto the cell for a LCR interconnection (left), and view of the typical geometry of an LCR interconnection (right) (Muehleisen, et al., 2016).

Also, the Light Capturing Film (LCF) is another similar way to improve the performance of the solar PV cell (Holst, et al., 2016). The LCF uses an attached film with different (spotted or grooved) surface pattern on the normal flat ribbon. This design is expected to bring the cost reduction compared to the LCR due to low cost material and simple attaching process. Figure 12 depicts a schematic view of reflecting light for a conventional design and a LCF design of PV module ribbon interconnection; and as it is shown the reflected lights can be mostly recaptured by utilizing the LCF. It is reported that the LCF design can improve the photocurrent recapture ratio of ribbon from 6% to about 50% and it causes an improvement in the module short circuit current and power gain by 1.3% and 1.7%, respectively (Chung, et al., 2013). However, this design is prone to the delamination and debanding, particularly when the PV module operates under high temperature cycling condition.

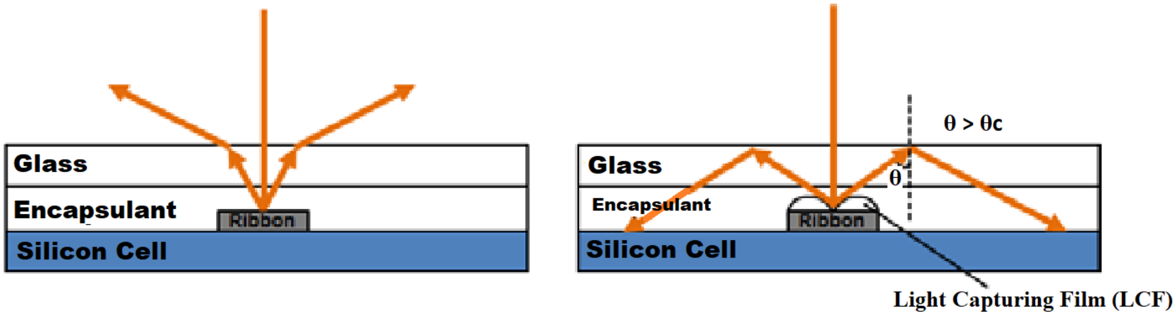

Figure 12: Schematic view of reflecting lights from surface of PV module ribbon interconnection, a: conventional ribbon interconnection design, and b: LCF design (Chung, et al., 2013).

2.2.2. Ribbon Interconnection Embedded in Polymeric Film

Day4 Energy Inc. introduced the Day4™Electrode for cell metallization technique which comprises of low-melting solder coated copper ribbons embedded in transparent polymeric film with adhesive layer (see Figure 13). This approach requires the combination of lamination and interconnection into a single lamination step (Schneider, et al., 2006).

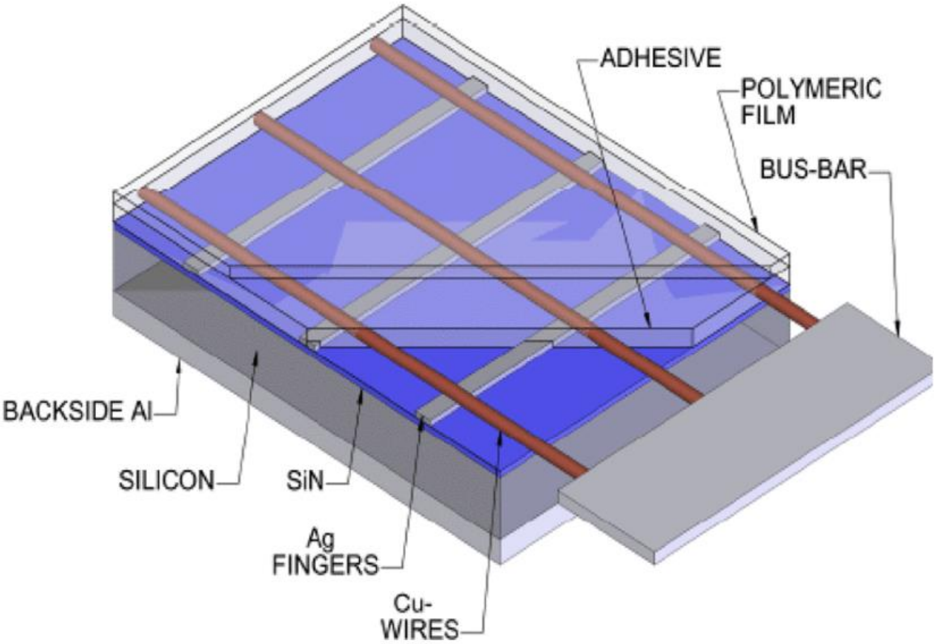

Figure 13: Schematic view of the Day4™Electrode cell metallization technique, using Coated ribbon interconnection embedded into s adhesive (Schneider, et al., 2006).

The Day4™Electrode eliminates the needs for the front side busbars by connecting to the Ag fingers directly and it can save up to 40% of the Ag paste by optimization of the screen printing sequence. So, a considerable reduction in cost, shading drastically and reaching higher value of generated current and cell efficiency are the advantages of this approach. However, the lower the number of electrode ribbons especially in the larger solar cells causes increasing solar cell series resistance and decreasing fill factor values. Another advantage of this design is keeping the performance with almost efficiency of the cell after breaking because electrode ribbons preserve electrical integrity between the cells broken parts (Schneider, et al., 2006).

The smart ribbon connection technology (SWCT) is the developed design of the Day4™Electrode, in which the SWCT uses higher number of ribbons but with lower diameters and can improve the advantages such as less optical losses owing to the shorter length of the fingers Due to avoiding the high temperature soldering steps, low temperature contacting during module lamination, and relaxing the constraint between the ribbon and metallization; better cell backside passivation can be achieved (Faes, et al., 2014). SWCT is also compatible with multiple material types such as Al, Cu, Ni, Ag and the interconnection of new cell concepts, such as rear passivated cells, HJT, metal plating and IBC. (Söderström, et al., 2013).

2.2.3. Multi-Busbar (MBB) Ribbon Interconnection

The MBB Connector is another design which uses high number of busbars and reduces the width of busbar and cross-section of fingers (saving up to 89% of silver consumption) (Braun, et al., 2012). Indeed, the busbars in the conventional ribbon interconnections are replaced by multiple narrower ribbons which are connected to the perpendicularly orientated finger grid (Schindler, et al., 2013). For instance, by using 15 ribbons instead of three/five conventional ribbons, the finger length and width can be reduced from 25mm to 5mm and from 50μm to 17μm, respectively (Braun, et al., 2013). In comparison with conventional ribbon interconnections, the use of the MBB interconnection results in reducing the series resistance losses, since the increased number of current paths associates more uniform current distribution. In addition, the roundness of the circular ribbon geometry causes the reflection of most of the incident light onto the wafer surface and leads to less shadowing loss (Söderström, et al., 2013) (see Figure 14). Also, there is another concept to use MBB interconnection with triangular cross-section which can improve the optical performance up to 2.35% compared to using the conventional ribbon interconnections (Mittag, et al., 2016). By reducing the shadowing loss, MBB technology leads to rise the current and power output and improves the module efficiency (Schindler, et al., 2013) and (Walter, et al., 2014). So, for decreasing the electrical current losses, MBB does not require thicker ribbons and more encapsulate during module production and it avoids more material usage and high stress levels in the solar cells (Qi, et al., 2011). However, there is still an important challenge related to the non-homogeneity of solder coating being produced around the Cu-ribbon which may result in insufficient solder joints and decrease the strength of the ribbon connection to the cell (Walter, et al., 2014), especially if it is closed to the high stress level area of the interconnection (Rendler, et al., 2016). Figure 15, displays a cross-section view for round copper ribbon with solder coat in homogeneous and non-homogeneous coating geometry. Section 2, Chapter 5 of this thesis presents FEM study of the effect of non-homogenous coatings of the crack initiation and propagation in the solder joints of MBB interconnections.

Rendler et al. have investigated the deformation of cell and thermomechanical stress in both cell and MBB interconnecting ribbons of the solar PV modules. They found that by using ribbons with lower diameter and made of softer copper alloys, the thermomechanical stress induced in the silicon cell can be decreased. They also recognized that the maximum stress in the ribbons occurs at the edge of the outermost contact pads on both sides of the solar cell (Rendler, et al., 2018). This important region of the solder joint material is where the IMC is formed.

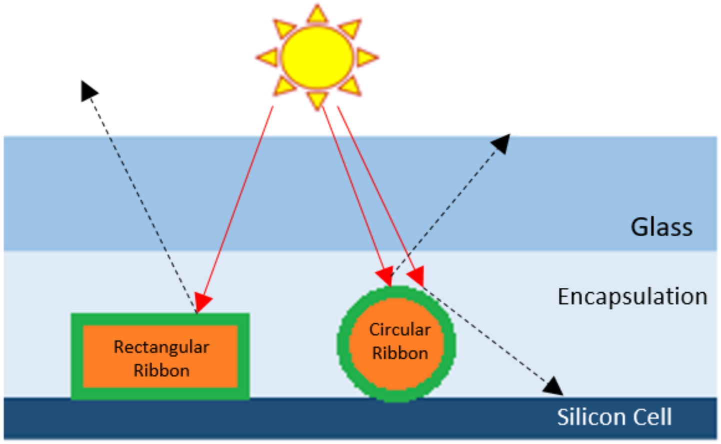

Figure 14: Reflection of the incident light onto the wafer surface for both rectangular and circular ribbons, adopted from (Söderström, et al., 2013).

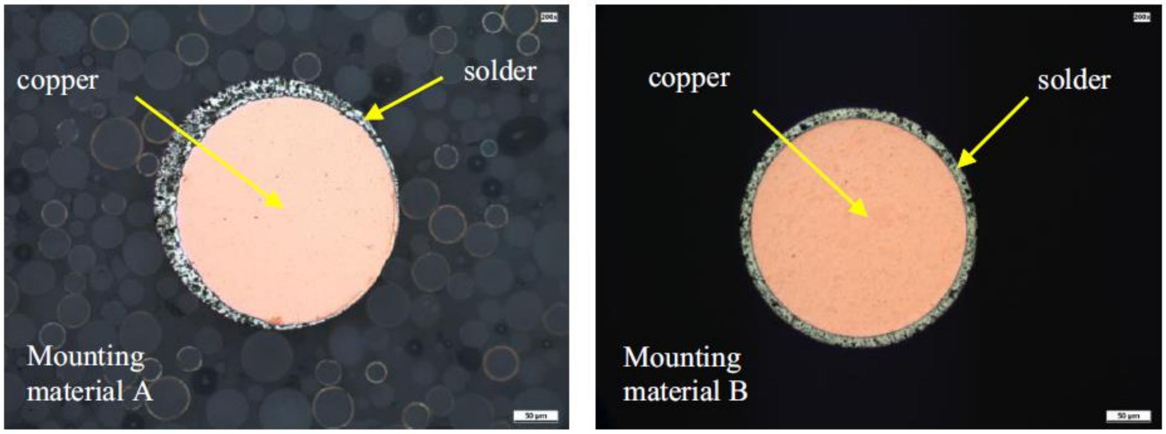

Figure 15: Round Copper ribbon with homogeneous (right) and is non-homogeneous (left) (Walter, et al., 2014).

Triangular ribbon interconnection is another concept for ribbon interconnection design which improves the performance of the PV module. Indeed, this design follows using high number of ribbons in the cell as it is introduced in MBB interconnection design. An investigation of the optical ray tracing for the triangular ribbon interconnection showed that this design improves the optical performance 2.35% compared to conventional ribbon (CR) interconnection (Mittag, et al., 2016).

2.2.4. Wave-shaped Ribbon interconnection

One of other novelties in design of round ribbon interconnection is using wave-shaped ribbons in the PV module which improves its reliability, especially in the case of back-contact method which provides higher efficiency. This interconnection design is based on soldering copper-based ribbons directly on the contact fingers of solar cell without any needs to use the contact pads and it saves the silver consumption. (Rendler, et al., 2017). However, additional shading in case of using wave-shaped ribbons in front side of solar cell and also increasing the electrical resistance of ribbon can be two important disadvantage of this design. Figure 16 shows microscopic images for two different geometries of wave-shaped ribbons and also soldered ribbon assembling on the silicon solar cell. The experiments on the longitudinal softness of wave-shaped ribbons shows an up to 90% reduction of the yield limit in wave shape interconnector which decreases thermomechanical stress levels of the solder joints and also reducing cell bowing problem. Consequently, it improves the long-term stability of solder joints and reliability of PV modules (Rendler, et al., 2017). However, investigation of the mechanical and electrical properties of wave-shaped ribbons with different peak-to-peak amplitudes, periods and diameters shows that the geometry of wave-shaped ribbon increases the electrical resistance (due to increasing the length of ribbons). Also, ribbon diameter change during stretching process may cause grooves at the peak of waves (due to sharp edges of the shaping instrument) and it is detected as another reason for rising the ribbon electrical resistivity(Rendler, et al., 2018).

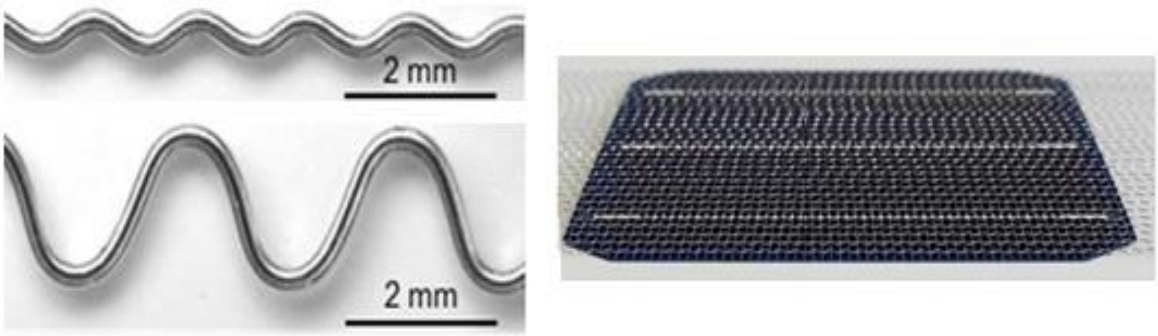

Figure 16: Microscopic images of wave-shaped ribbons, with different amplitude (left) and arrangement on the cell (right) (Rendler, et al., 2018).

Although there are several concepts in design of the ribbon interconnection to improve the reliability and efficiency of PV modules, a massive industrial attention is still being payed to use the conventional ribbon interconnection due to easy fabrication process and most common available manufacturing technology.

2.3. PV Module Reliability

Unlike other electrical equipment, PV modules are unique in that they carry very long-term performance warranties of 20 - 25 years (indeed, very few types of electrical equipment have such long warranties). For this reason, improving the reliability of PV modules remains a major R&D challenge; as reliability is neither defined nor covered by the existing quality certification standards such as the IEC 61215 (IEC International Electro Technical Commission). Hence, the design qualification to those standards does not imply the PV module reliability. This lack of reliability standards is partially due to the fact that solar PV module technology is still in its early stages (with most PV installations yet to reach their 20 to 25 year lifetime as per warranty), and thus there is very little or no statistical data available on the field failure of PV module (Ishii & Atsushi, 2017).

The focus of the recent PV module reliability studies has been on the ribbon interconnection design and thermal failure (Ogbomo, et al., 2018) and (Afriyue Nyarko & Takyi, 2021). These include some experimental studies focused on the investigation of the failure rate of the ribbon interconnection and this shows that the solder joint in the ribbon interconnection is the most common source of failure. Indeed, the solder joint of ribbon interconnection has been reported as the most susceptible part of the PV module system, and hence the dominant factor in PV module degradation and responsible for about 40% of recorded field PV module failures (Hermann, 2010). In particular, an investigation on the PV module life-time using 3 million module-years of live field data showed that solder interconnection failures were the reason for circa 66% of the PV module returns (due to failure over an average deployment period of 5 years), whilst encapsulate and back-sheet failures accounted for circa 22% of the returns (Hasselbrink, et al., 2013).

According to the literature, several studies on the fracture mechanics of the silicon cells in the PV modules have been performed; for example, in the PV solar cells exposed to thermal cycling and to mechanical loading, cracks were observed mainly at the beginning and the end of the busbars, in which the cracks grow along the busbars (Sander, et al., 2011). Although the failure and reliability of the most components in the PV solar modules have been studied well, however, there are not enough reported studies on the thermal failure of the solder joint in PV modules interconnection and their design to improve the reliability. Hence, the study of solder joints used in different device, but under similar loading condition can be a good practice to understand the thermo-mechanical reliability challenges of the solder joints in the PV module interconnections. For this there are numerous works on the thermal failure of solder joints used in the electronic packages. For example, the failure and thermos-mechanical reliability of the BGA (Bull Grid Array) solder joints in PCB (Printed Circuit Board) assemblies have been greatly studied since 1990 (Anjoh et al., 1998). In particular, increasing application of BGAs in the miniaturized electronic device such as mobile phones still faces the thermo-mechanical reliability challenge in terms of the device functionality, system miniaturisation and the capability of solder joints to remain in conformance with their electrical and mechanical specifications under operational conditions (Lu et al., 2020) and (Depiver et al., 2021). Also, the FEM simulation for thermomechanical analysis of BGS solder joints has shown that the package size is the most influential factor among all design parameters in which the smaller size of package can provide higher reliability (Strusevich et al., 2007). Investigations on the thermal fatigue failure of the BGA solder joints have shown that the induced stress (mostly in shear direction rather and tensile direction) and the accumulated strain energy lead to crack initiation and propagation in the solder joints (Chen et al., 2016). By now, several approaches using constitutive equations (correlated with FEM results) are developed to predict the thermal fatigue lifetime of the solder joints (Morooka & Kariya, 2021). In this case, Section 2.7 and Section 2.8 of this chapter present a review on the solder joint failure and the numerical approaches for prediction of the solder joint fatigue lifetime.

2.4. Reliability of the PV Module Ribbon Interconnection

The ribbon interconnection of the solar PV module is critically important in component. The ribbon interconnection is soldered directly onto silicon crystals to interconnect solar cells in the PV module and it plays an important role in determining cell efficiency, as it serves to carry the current generated in the solar cells to the PV busbars. There are several recognized reliability challenges for the PV module interconnection such as the connection of the ribbon to the cell and bending the ribbon between the adjacent cells. For example, an investigation on the placing the ribbon interconnection on the rear pad in the solar PV cells showed that an unbalance positioning of the ribbon can lead to a massive increase of thermomechanical stress in the silicon cell (up to 50%) which can adversely affect the reliability of the PV module (Hsiao, et al., 2020). Also, the FEM results for the stress distribution in the copper ribbons near the vicinity of the gap between cells showed that during the lamination process (150°C temperature), the copper ribbons exhibit some plastic stress due to the movement of the cell (Pamir Aly, et al., 2020). The movement of the cell can cause a high shear force in connection between the copper ribbon and the cell and leads to failure of the solder joint material used to connect the copper to the cell finger. Also, the investigation of the thermo-mechanical stresses in the silicon cell showed that stress level on the ribbon bend between the cells (which is more flexible to move) is lower than stress in connection of ribbon to cell (Owen-Bellini, et al., 2015). However, among all aspects of potential failure of PV module cell connections, the major challenge is referred to the contact area between the ribbon and the cell. Indeed, the weak contact strength of ribbon interconnections to the cell using solder joint materials or even low contact strength between the ribbons and fingers (due to low width of fingers) can adversely affect the reliability of the PV module (Rendler, et al., 2017).

The ribbon interconnection failure is mostly linked to crack initiation and propagation in the solder joints material which exhibits brittle mechanical behaviour. The nucleated crack in the solder joint can lead to hot spots resulting from high contact resistance at the ribbon and the cell interface and then potentially results in DC arc (Itoh, et al., 2014). In addition, these hot spots can also lead to the degradation of the encapsulation and partial shading cell effect; consequently, this problem impacts on the parameters of performance and reduces power outputs and the efficiency of the PV module (Bidram, et al., 2012)and (Pareek, et al., 2017).

In this section, the main focus is on the failure of the solder materials used in the PV module ribbon interconnection. In fact, the reasons for the failure of ribbon interconnections can still be held in common with other new interconnection technologies since the most of designs use the ribbon interconnections made by coating solder alloys on copper ribbons. It should be noted that the most common material for ribbon interconnection is copper thanks to high electrical conductivity and low material cost. However, other ribbon interconnection materials including silver, brass, tin and aluminium are numerically studied and FEM results of creep strain energy showed that silver provides the highest reliability of PV modules compared to the other materials (Ogbomo, et al., 2018).

2.5. PV Module Interconnection Joint Materials

Many efforts focused on developing new joining materials have been reported, such as that on electrically conductive adhesive (ECA) joints or conductive paste assisted low-temperature soldering (CALS) as an adhesive layer to connect the ribbons to the cells (Song, et al., 2019) and although this leads to a cheaper interconnection solution (use of less solder materials), the interconnections do not have the required high shear strength. By now, there are not widely established interconnection material types to provide enough strong interface connection and it is mostly limited to lead-based/lead-free solder joints which are the most common materials for connecting the ribbon to the PV cells (T. Zarmai, et al., 2015). Hence, the design and reliability of the PV module interconnections are mostly based on investigation of lead-free and lead-based solder joints. For example, a study on the life prediction of lead-based and lead-free solder joints used in c-Si solar cell interconnections under thermal condition in high temperature operation condition has shown that the lead-based solder joint (Sn60Pb40) are likely to exhibit superior reliability (up to 30% higher thermal cycles to failure) compared to the lead-free (Sn3.8Ag0.7Cu) solder joints (Afriyue Nyarko & Takyi, 2021).

In 2002, the European Union adopted the Restriction of Hazardous Substances (RoHS) legislation which restricts the use of certain hazardous substances in electrical and electronic equipment due to containing lead and the required flux contents which result in disastrous effects on the environment. The first RoHS Directive took effect from July 2006 and based on that the use of lead-based solders is restricted (The EU Parliament and the Council of the EU Union, 2011). For this reason, lead-free solders which are environmentally friendly are one of the most common materials to replace using lead-based solders in solar PV modules. The melting point for lead-free SnCu alloys (with/without additives such as Ni, Bi, Ge, Co, and Mn) is about 227°C and the melting point of conventional lead eutectic solder (Sn37Pb) is only 183°C. Consequently, lead-free solder has higher defect probability on the PV module material such as silicon layer due to higher thermo-mechanical stresses resulting from higher soldering temperatures in manufacturing process (Cheng, et al., 2017). SnAg alloys has also the melting point about 221°C. However, by adding some alloying elements such as Bi, Zn or Cu, not only the melting temperatures will be decreased, but also better structural, thermal and mechanical properties such as higher young modulus, longer fracture and creep resistance can be provided. One of the most famous lead-free compositions of solder alloys is Sn-xAg-0.5Cu (x=1, 2, 3 and 4 in mass%) which makes possible less increase in temperature of soldering process and consequently induce less thermal stress in the cell. For instance, Sn3.0Ag0.5Cu which contains 3% of Silver has the melting point around 215°C, but it raises the cost of soldering process compared to other solder materials due to high percentage of using silver material (Cheng, et al., 2017) and (Mostafa Shala, et al., 2018). It is also found that among all SnAgCu solder alloys, SAC396 (Sn3.9Ag0.6Cu) shows better thermo-mechanical reliability due to less accumulated creep strain energy in solder contact boundaries subjected to the thermal cycling load (A. Depiver, et al., 2019). For these reasons, all the FEM investigations carried out for this PhD study (presented in chapters 4,5, and 6) are based on the use of lead-free (SAC396) solder joints - for connecting the ribbon interconnections to the c-Si solar cells.

Another alternative for the interconnection joints in the solar PV module is the ECA (Electrically Conductive Adhesive) technology which uses the lead-free joints to replace soldering process with gluing process to connect the ribbon to the solar cells. Indeed, using the ECA technology solves the challenge linked to formation of the brittle IMC layer which has high potential to be cracked (Song, et al., 2019). Hence, conductive adhesive bonding can be a beneficial idea to exclude high residual thermal stresses caused by the soldering process as it can be processed at relatively low temperatures (approx. 180°C) (Pander, et al., 2014) and (Schwark, et al., 2017). However, the main challenge of the ECA technology is high manufacturing cost and there are some efforts to reduce the cost by decreasing silver consumptions based on optimizing the bonding volume and the contact design (Geipel, et al., 2018). However, this type of bonding is still not largely recommended and popular in the industry due to another challenging weak point which is high delamination potential and low adhesive strength. Indeed, the high temperature (~150°C) in the lamination process and the applied pressure (~760mmHg) in assembling the back-sheet and the glass can have negative thermal effects on the strength of adhesive joints and can increase probability of micro-crack nucleation in the interconnection (Pander, et al., 2011) and (Song, et al., 2019).

2.6. Crack and Failure of PV Module Solder Joint Interconnections

Whilst in several works related to the reliability of PV modules, the attention has been closely drawn to the failure of the interconnection between PV cells. Heiman, et al. proved that different failure modes on the front and rear side of solar PV cells have different influences on the reliability of the PV module. They explained that to achieve the long-term mechanical and electrical stability of the solder joints, failure of the solder on backside of cell can be more important rather than others; if the solder ribbon is placed incorrect on the aluminium metallization pad on the rear side (Heimann, et al., 2014). However, the FEM results for the accumulation of strain energy in the solder interconnection (without assuming incorrect placement of the interconnection ribbon) subjected to the thermal cycling showed that the front joint is more susceptible to the degradation compared to the rear joint (Jiang, et al., 2020).

Cracks are the main reason for the failure of PV module solder joints as they are mostly initiated in solder boundaries during both high temperature manufacturing process and operating under thermal cycling. Tippabhotla found that during encapsulation in manufacturing process, the CTE mismatch between materials (from $16.8 \times 10^{-6} \frac{1}{K}$ for Cu and $2.5\times 10^{-6} \frac{1}{K}$ for silicon) makes a local bending curvature in silicon cell and results in a high residual stress and strain in area near to the soldered interconnectors (Tippabhotla, et al., 2017) and (Itoh, et al., 2014). It means that the CTE mismatch between interconnection materials generates high thermal strain energy which causes cracking and failure of the solder joint. In the PV module solder joint interconnections, the cracking parameters such as the crack initiation temperature and growth rate are dependent on the configuration of the ribbon interconnections as the magnitude and distribution of the induced strain and stress components (due to the CTE mismatch between solder and interconnection materials) are influenced by the geometry of design. It is also reported that the crack is nucleated in the corner of the solder joint material as the maximum in plastic deformation occurred in this region (Deng, et al., 2005), (Zhu, et al., 2014) and (Nhat Le, et al., 2016). Kumar also studied the damage at the silver-solder interface of the PV module; and it is observed that the damage at the interface layer increases due the presence of extra solder around the busbar (Kumar & Gupta, 2019). Figure 17 shows a cross-sectional view of the crack initiated and propagated at the solder joint boundary with the silver-pad in a PV module interconnection subjected to the thermal test (Park, et al., 2013).

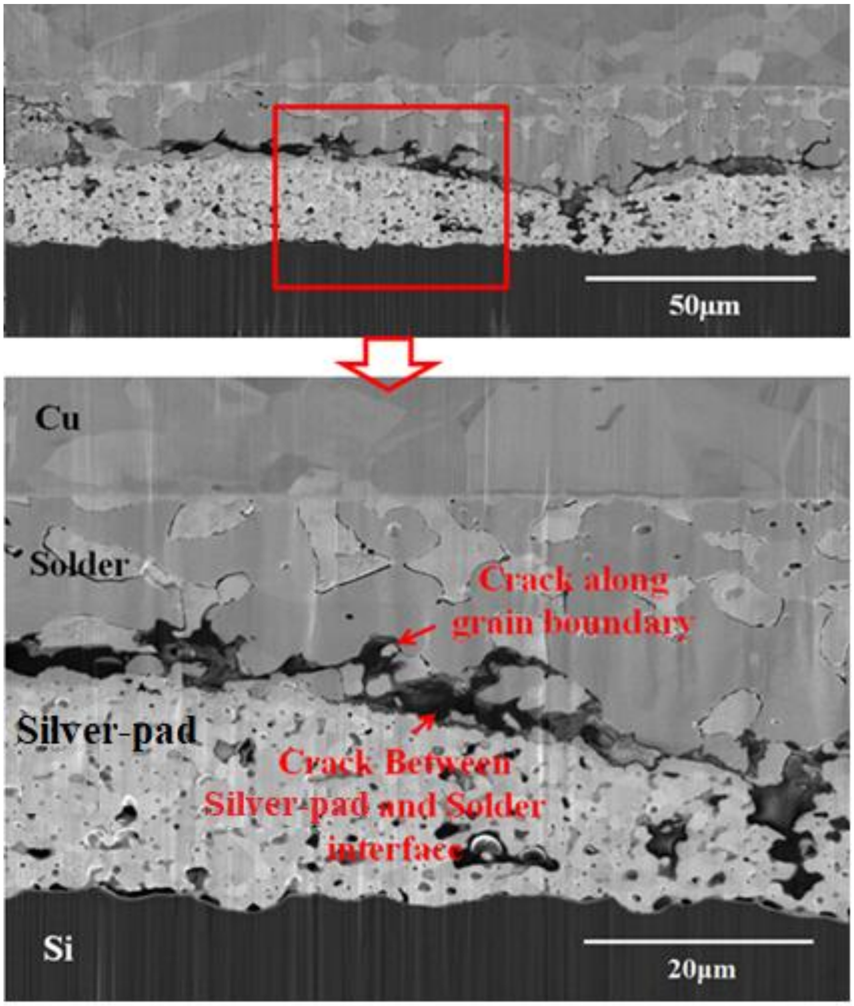

Figure 17: SEM micrographs of crack at the solder joint (in the silver-pad side) of PV module interconnection subjected to the thermal test (Park, et al., 2013).

The nucleated crack can grow through the connecting layer and ultimately leads to failure of the PV module solder joint interconnections during high temperature cycling condition. In many number of works regarded to the failure of PV interconnection, progressive crack in solder joint is the main reported failure mode which during fatigue life it can adversely affect the performance of PV module and decrease the power output. Indeed, generated crack induces weak contact condition between Cu ribbon and the cell and consequently it increases contact resistivity and electrical cell-to-module (CTM) loss and decrease the power gain from the module (Tae-hee Jung, 2014) and (Park, et al., 2013). This problem can also cause hot spot and eventually disconnection of bus bar line and consequently resulting in DC arc (Itoh, et al., 2014). For example, the Electroluminescence (EL) images of PV module sample before and after 200 thermal cycles showed that some cells in the PV module becomes dark after test, while the maximum power decreases by 3.7% as a result of an increased R of 12.6% (Du, et al., 2020).

It should be noted that the thermal crack in the PV module solder joint interconnections is highly depended on the material properties (particularly for PV modules operating under hot climate). As there is not a wide range of interconnection material to properly solve the challenge for the thermal failure of the PV module interconnection, lowering the module temperature could be an option to increase the reliability of PV modules' part and at the same time keep the efficiency of the module high. There are some technologies introduced for cooling the PV module by using air/water/combined coolant systems installed at the backside of the module (Diwania, et al., 2020). However, cooling system for PV modules are not very popular as they need frequent maintenance due to the mechanical coolant systems. Weber, et al., also studied the influence of phase change materials (PCM) on the fatigue life of PV module interconnection to enhance thermal conductivity and to reduce the short-time fluctuation of the module temperature during the operational condition. They modelled the PV module interconnection operating under recorded temperature loads to determine the cumulative damage in the interconnection. Their FEM results showed that a significant increase (20% to 30 %) for the reliability of PV module interconnection can be achieved by using commercial Paraffin RUBITHERM RT 28 HC mounted on the backside of a PV module (Weber, et al., 2018).

2.7. Solder Joint Failure

Based on the literatures, there are few works that has studied the failure mechanism of the PV module solder joint interconnections; and the reason seems to be the complexity of the experimental sample of PV module interconnection. However, the nature of failure and mechanical characteristics of solder joints in the silicon boards of electrical devices (particularly in the ball grid arrays) are widely studied in both experimental and numerical works. A number of previous studies have reported on the fracture mechanics and the effect of solder joints geometry on the reliability of electronics assembly board interconnections subjected to thermo-cycling loads. These include the development of an empirical equation for predicting the thermal-fatigue life of solder bumps using the measured crack growth rate at the crack tip (H. Lau, et al., 2001); the creep investigation to study the effect of solder joint geometry on the reliability of ball grid array (BGA) solder joints on flexible and rigid PCBs subjected to thermo-cyclic loading (Lau, et al., 2014); and modelling evaluation of Garofalo-Arrhenius creep relation for lead-free solder joints in surface mount electronic component assemblies to propose a paradigm for selecting a suitable constitutive model to predict accurate creep parameters (H. Amalu & N.N. Ekere, 2016).

The literatures illustrate that, one of the key challenges in numerical investigation of thermal failure of the solder materials is accurately determination of the material temperature dependencies that can extremely affect the numerical outputs to find the exact thermomechanical response and to predict the failure behaviour of the solder materials. In this case, the experimental tests to study the stress-strain behaviour of the solder joints in different strain rate and at various temperatures showed that particularly Sn–Pb solder behaviour is strongly strain rate and temperature dependent, whereas the lead-free solders showed less dependency (Siviour, et al., 2005). Among all mechanical characterizations of the solders, elastic parameters (Young's modulus, E, and Poisson's ratio, ν) and also creep parameters have been well studied. For instance, Tanaka employed the Ultrasonic Pulse Echo Method to determine analytical formula for elastic parameters with considering temperature dependency of both lead based and lead-free solders (Tanaka, et al., 2005). They considered that there is a rapid decrease in the Young's modulus above 80°C due to the atomic motion along dislocations and grain boundaries.

The failure of solder joints subjected to the thermo-cycling loads has been more attended rather any other solder joint failure aspects due to exhibition of higher negative influence on the reliability of solder joints. Most of experimental works on the fatigue failure of the solder joints have used the thermal aging tests to understand the nature of crack nucleation and to define of the length of crack in low and high fatigue cycles. However, other mechanical aspects of the solder failure have been partially studied to determine the effect of the both non-thermal conditions and the combined mechanical-thermal condition on the failure of the solder joints. For example, an experimental work on the cyclic behaviour of solder joints in vibration coupled with thermal cycling showed that vibration significantly modifies the total behaviour of solder joints in the concurrent loading (Basaran, et al., 2001).

2.8. Numerical Approaches for Estimating Solder Thermal Fatigue Lifetime

Numerical approaches (i.e. FEM) have been widely used in many studies to find the different fatigue parameters such as plastic strain energy density and plastic strain and then to calculate the number of cycles to failure. The Coffin-Manson model (Chen, et al., 2017) and (Chen, et al., 2021), the Total Strain model (Lee, et al., 2000) and (Yao, et al., 2017), the Morrow Energy Density model (Akay, et al., 2003) and (Stoyanov & Bailey, 2009), the Paris Law model (Zhang, et al., 2008) and (Ma, 2009), the Darveaux fatigue model (Darveaux, 2000) and the Johnson–Cook model (Halouani, et al., 2020) are major numerical models to estimate the fatigue life of solder joint materials. Basically, the models for estimation of the fatigue life of solder joints can be sub-divided into three categories, namely: stress-based, strain-based and energy-based approaches. According to the stress-based approach, the fatigue failure occurs when the induced stress reaches a trigger threshold (Li, et al., 2017) and (Han & Han, 2014).

In terms of the energy-based models used for predicting the creep-fatigue life of materials, the Morrow Energy Density model (Andersson, et al., 2006) and (Zhu, et al., 2014), is one of the most widely used methods. In this approach, the plastic strain energy density is used instead of the plastic strain values. The advantage of this method is that it incorporates the effects of both plastic strain and plastic stress on the cumulative energy. In the Morrow Energy Density model, the number of cycles to failure (N_f) is a function of the plastic strain energy density, which is obtained from the hysteresis stress-strain loops for each cycle.

In another study, Akay developed the model for predicting the creep-fatigue life based on the total strain energy, rather than the plastic strain energy density (Akay, et al., 2003). The stress–strain hysteresis energy is also important for predicting the fatigue failure life (Steinhorst, et al., 2013). For example, Darveaux proposed a fatigue model with consideration of the accumulated stress–strain hysteresis energy in the material to derive the equation for the crack initiation cycle number and crack propagation rate (Darveaux, 2000).

The strain-based approach is the most widely reported method in the literature for the computational study of creep-fatigue behaviour of the solder joints. For strain-based fatigue models, the strain is composed of the elastic strain, plastic strain, creep strain components, which are not easily distinguishable (Knecht & Fox, 1990). The Coffin-Manson model and the total strain energy model are two of the most popular strain-based models used for prediction of the thermal fatigue life of materials (Li, et al., 2017) and (Lee, et al., 2000). The Coffin-Manson model uses the plastic strain amplitude over a cycle to estimate the number of cycles to failure. Several modifications of the Coffin-Manson model have been used for the prediction of the fatigue life of materials in specific conditions. For example, Chen used the modified Coffin-Manson equation to introduce a coupling damage model considered low-cycle fatigue and creep (Chen, et al., 2017). In another study, Zhiwen Chen reported work based on combination of Coffin-Manson FEM model and Artificial Neural Network to reduce the computational time (Chen, et al., 2021). Previous work by Hund and Burchett showed that for strain levels less than 1%, Coffin-Manson model cannot accurately estimate the creep-fatigue life, and hence is not recommended, as the strain is mostly composed of creep and elastic strains rather than plastic strain (Hund & Burchett, 1991). The total strain energy model is introduced as a modified form of the Coffin–Manson model to incorporate both the elastic and plastic strains terms (Lee, et al., 2000) and (Yao, et al., 2017).

The strain and the energy terms used in the models discussed above for the estimation of the fatigue life of materials can be found by using the analytical constitutive models of creep behaviour. Examples of the constitutive models used for the prediction of the creep fatigue life of materials include the following: (a). Hyperbolic Sine (Ramachandran, et al., 2018) and (Stoyanov, et al., 2002), (b). Anand (Baber & Guve, 2017) and (Cho, et al., 2018), (c). Johnson-Cook (Halouani, et al., 2020) and (d). Power Law (Zhang, et al., 2008) and (Ma, 2009). Most of numerical studies on the creep behaviour of the solder joint (particularly for high-temperature creep) have used the Hyperbolic Sine constitutive models (Garofalo and Anand's visco-plastic creep models) (Depiver, et al., 2020).

2.9. Software for Simulation of the Thermal Failure of the Solder Joints

For numerical investigation of material thermal failure, there is a wide range of commercial finite element software to implement the relevant simulation. For this purpose, ANSYS and ABAQUS have been widely used for the damage investigation and the non-linear study of the creep-fatigue failure. These software support most notable creep models such as Hyperbolic Sine model and Anand model and there are numerous studies have been conducted to predict the solder joint reliability by means of ABAQUS and ANSYS. For example, Halouani et al., used ABAQUS software to develop a nonlinear damage model for SAC solder (Halouani, et al., 2020). In their model, the Johnson–Cook visco-plastic model is utilized to describe the material hardening behaviour and to estimate the fatigue life and to simulate the progressive damage in the solder joint. In another work, Stoyanov et al., has used ANSYS software to predict the physics-of-failure of micro-BGA solder joints in electronic packaging (Stoyanov, et al., 2020). In this research, the Hyperbolic Sine creep model in ABAQUS 2019 is used to determine the creep stress-strain distribution, and the total dissipated energy in PV module solder joint interconnections operating under different thermal cycling loads. Then, a developed Morrow Energy Density model as well as Coffin–Manson–Arrhenius formulation are used to estimate the creep-fatigue lifetime. Chapter 6 of this thesis presents the study of creep-fatigue analysis for different PV module interconnection designs.

Furthermore, ABAQUS is known as one of the main pioneer software (since 2009) for the implementation of the XFEM techniques to simulate the fracture mechanics problems. In 2017, ANSYS 18 also developed the feature for the XFEM simulation. Also, there are some other software such as GetFEM++, Altair Radioss, Code-Aster, etc. that can support the XFEM technique for the simulation of fracture mechanics. This research has used ABAQUS 2019 for the XFEM simulation of crack initiation and propagation in PV module solder joint interconnections (presented in Chapter 4 and 5) thanks to its user-friendly features such as easy implementation of the contact properties for the areas with high crack potential.

2.10. Intermetallic Compounds (IMC) Failure

Intermetallic compounds (alloys) form whenever two different metals are soldered together and grow as solid phases during solidifying of solders on the interface between the solder alloy and its bonding pads (Pecht, 1993). The diffusion-based intermetallic compounds have a brittle mechanical behaviour and the crystal structure of intermetallic compounds differs from that of the other constituents (Schmitt, et al., 2012). Indeed, diffusion of copper (Cu) and tin (Sn) elements in the soldering process causes formation of IMC interface layers at the solder and copper ribbon interface (mainly Cu3Sn and Cu6Sn5 IMCs). Deng observed the Cu6Sn has a larger grain size rather than Cu3Sn, resulting in a fracture path that is more cleaved through the grain, while Cu3Sn is cracked along the grain boundaries (Deng, et al., 2005). In the same way, Ag and Sn elements diffuse to form Ag3Sn IMC layers at the solder and silver pad (metallization) interface. The IMC layers grow during ageing process and service life and become thicker and as a result they are responsible for a decrease in the strength of the connection surface. It is shown that the IMC layers in the solder region boundaries play a crucial role in nature of failure and subsequently life time and reliability of solder interconnection (Yang, et al., 1994). Consideration of the IMC layers in solder failure investigation has been paid attentions in several works. For IMC layers, physical and mechanical properties such as elastic parameters as well as fracture toughness are measured to get better understanding of the fracture and failure of them and to predict the joint reliability more exact (Fields, et al., 1991).

Investigation of the impact of IMC layers on reliability of the lead-free solder joints in a flip chip package at elevated temperature operation shows that IMC layers play significant roles in the life of lead-free solder joints (Amalu & Ekere, 2011). The results of these previous studies show that the thermal fracture mechanism of a solder joint interconnection can generally be sub-divided into two distinct modes. Firstly, the fractures that occur inside the solder joint due to solder grain size growth and the corresponding decrease in bonding strength during thermal cycling, which then leads to crack propagation at the interface of large grain. Secondly, the fractures that occur at the interface of solder with interconnection material (that is within the IMC layer formation); for example Cu5Sn6 and Ag3Sn which is formed through the dissolution of the Ag/Cu materials in the solder (Itoh, et al., 2014).

There is also another potential defect for nucleation of voids by the outgassing in a solder joint (due to evaporation of solvents and additives) during heating in soldering process (Cheng, et al., 2017). Fei applied finite element approach to investigate the effect of probable microscopic voids in solder material under dynamic loads. They used porous plastic material and elastic material for modelling Pb-free solder and IMC interface layer, respectively, and the wave interface surface was applied between two these layers. Their simulation study shows that higher strain rates and thicker IMCs results in IMC-interface brittle fracture or IMC-controlled fracture; whilst lower strain rates and smaller IMC thickness leads to solder-internal fracture or solder-controlled fracture (Fei, et al., 2012). Results from a study on the analysis of experimental samples have shown that the Ag to solder crack in IMC region is more prevalent than the Cu to solder region crack (Jeong, et al., 2012), whilst the studies by Li showed that fractures and the straight crack propagation path tends to be located on the component side of the solder interconnections (beneath die edge) (Li, et al., 2009); and that the tensile and the shear strength of IMC layers decrease with increase in the IMC layer thickness. Zhong also studied the mechanical properties of two separated major species of IMC, Cu6Sn5 and Cu3Sn in lead-free solder and it is detected that cracking around the IMC layer is the primary failure mode in the PV module solder joint interconnections (Zhong, et al., 2010).

Among all IMC layer parameters, thickness and material combination of the IMC layer are recognized as the most important parameters, as they have a considerable influence on the strength and fracture morphology of the solder joints. It has been shown that an increase of IMC thickness results in a rougher interface and consequently leads to weaker solder joints (Zhong, et al., 2010). Indeed, the strength of the solder joint can be reduced by thermal cycling due to coarsening of Ag3Sn particles in IMC layer. This is particularly true for the manufacturing process in which the high reflow soldering time and/or temperature lead/s to a significant increase in the IMC thickness (Yang, et al., 1994). Conversely, it has also been shown that higher cooling rates (after reflow) results in thinner IMC layer. Furthermore, the results from the microstructure evaluations of thermally aged solder joints shows that the IMC thickness determines the shear fracture mode of the solder joints, but the shear strength is more controlled by the solder strength, rather than intermetallic thickness (Deng, et al., 2005). Thermo-mechanical investigation of the solder joints in c-Si solar cell assembly indicated that the optimal IMC thickness for 20μm thickness of lead-free solder (Sn3.8Ag0.7Cu) is 2.5μm since the creep strain energy density in solder is the minimum and can guaranty 25-year fatigue life. They also found that the highest creep strain energy levels are located in the lower side of solder joint adjacent to silver-pad and this area has the most potential to initiate crack (Zarmai, et al., 2016).

2.11. Chapter Summary

In this Chapter, a review on the design and reliability of PV module interconnection is presented. The literature showed that although using the ribbon interconnection in the front-to-back cell interconnection technique is very common and well-satisfying approach to build in the interconnection between cells, but there are still several challenges to re-design them for improving the PV module efficiency and reliability. Several new configurations for the design of the PV modules interconnections are introduced by manufacturers to solve the challenges especially in case of module efficiency and performance. Many new ideas for structured ribbons such as Light Capturing Ribbon, Multi-Busbar interconnector, Round Ribbon, Triangular Ribbon and Wave-Shaped interconnections have been developed to improve the performance of the PV modules. The mentioned concepts can offer a reduction in manufacturing costs (by reducing material consumption) and an increase in power outputs of each cell (mostly by decreasing optical losses).

However, there is no longer sufficient investigation to find more exact reliability of these new designs and subsequently the market has not still paid enough attention to use them in new products. Therefore, investigation of reliability and study on failure of these new designs are highly suggested to introduce them for a wide manufacturing range.

Secondly, to study the reliability of the PV module interconnections, the failure modes of solder joints (as the most common material to connect the ribbon to the cell) are reviewed. The collected data from PV module field data and analytical/experimental works showed that the main concern for the PV module interconnection reliability is the thermal failure of solder joints; and it is mostly because of crack initiation and propagation during high temperature condition. In the brittle IMC layer (interface area between the solder and interconnecting materials), the micro-cracks can be nucleated (due to the high accumulation of strain energy and thermomechanical stresses); and then they propagate throughout the layer during thermal cycling in service condition. The crack induces contact condition and increases the contact resistivity and consequently it causes adversely affect the performance and reliability of the PV module.

For investigation of micro-scale crack initiation and propagation in the PV module solder joint interconnections subjected both lamination process and thermal cycling of service condition, FEM simulation can be a very helpful method to evaluate the reliability of the PV module interconnection. To accurately simulate the PV module interconnection, considering the nonlinearities such as plastic material property, time/temperature dependency of material properties, presence of the IMC layers and also modelling all structural details are the main challenge. So, there is a vital need to develop an advanced FEM simulation equipped by fatigue and fracture mechanics' solvers to accurately estimate failure rate of interconnecting contacts and to predict reliability of PV module ribbon interconnections.

The thermal fatigue and creep is also known as one of the main failure mode of the PV module solder joint interconnection operating under high thermal cycling load. According to the literature on numerical approaches for estimating creep-fatigue life of the solder joints, using the modified Coffin-Manson model and the developed Morrow Energy Density model (based on the total strain energy) are mainly suggested to determine the number of thermal cycles to failure (N_f). In addition, the analytical Hyperbolic Sine constitutive model is also widely used to define the energy terms of the mentioned models for the estimation of the creep-fatigue life of the solder materials.

In summary, the review of recent published works on PV module reliability, depicted that there are some important gaps and questions to be studied and answered. These gaps are mainly relevant to the reliability and thermal failure of the solder joints in all type of PV module ribbon interconnections (particularly, new ribbon interconnections). Answering the questions needs better understanding the PV module ribbon interconnection design and the effect of configuration on its failure and the associated reliability. The needs are mainly including investigation of the potential crack initiation and propagation in the PV module solder joint interconnections during the lamination process (early cracks) and also investigation of the creep-fatigue failure of them during the lifecycle of the module.

In the next chapter, the methodologies used in this study to investigate the thermal failure of the PV module solder joint interconnections is presented. These methodologies are based on FEM simulation and they concern the most important nonlinearities such as time/temperature dependency of material properties; as considering the nonlinearities in computer aided simulation is recognized as a key requirement.

Chapter 3

3. Methodology

Understanding and improving the design, production, and operating requirements for PV module and solar plant installation requires better characterization and modelling of the causes, modes, and mechanisms of failure of PV module interconnection. In general, failure analysis is designed to determine the failure modes (how the product failed), the failure site (where the product failed), the failure mechanism (the physical phenomena involved in the failure), the root cause (the design, defect, or loads that caused the failure), and the failure prevention methods. The information gathered during the failure analysis stage is then used to create reliability prediction (or physics-of-failure) models that designers can use to choose design attributes that will reduce future designs' susceptibility to failure due to the mechanisms identified during the failure analysis stage. The predictive models also enable the user to choose climatic and operational loads that reduce the PV module interconnection design's vulnerability to failure during usage.

The methodology presented for this study employs physics-of-failure based concepts to analyse if a part/system can satisfy established life cycle criteria based on its materials, geometry, and operational characteristics. As a result, prior to manufacturing, the design may be evaluated. The technique may also be applied to the design for dependability evaluation process, which allows designers to make design modifications in real time and analyse the impact on product reliability. Ultimately, the project will provide a virtual reliability qualification method for evaluating the life expectancy of PV module interconnections (and packages) under expected life cycle loading circumstances.

This chapter presents the methodology used in this study for the investigation of PV module interconnection failure. Also, the chapter depicts the details of the applied FEM to simulate the crack analysis and creep-fatigue analysis for PV module interconnections.

3.1. Introduction

To understand the failure modes of the PV module including the failure mode of the PV module solder joint interconnections, investigation of the field data could be the first step. The design based on the observation of failure modes in operation of the PV module needs a long time equal to the service life of the modules. However, this is not practical as the manufacturers are motivated to introduce new designs with better performance and but at lower cost. In terms of the reliability and failure of the PV module parts, particularly solder joints, the designs are not still sufficiently based on the available standards and more experimental and numerical analysis are needed to estimate the service life of the PV modules. Numerical analysis is the most available and is the cheapest way to understand the solder joint failures and to help with estimating the PV module reliability operating under service condition.. For example, FEM investigation on the failure of the conventional PV module interconnection (under thermal cycling load with temperature ranges of 25°C to 65°C) estimated that the number of cycles to creep-fatigue failure of the SnPb solder joint is 12,814 cycles (Afriyie Nyarko, et al., 2021).

The computer aided simulation and numerical investigation of different failure modes of the PV module solder joint interconnections has still a challenge to consider the real form of all engaged parameters including nonlinearity of materials and the structural details of the whole PV module operating under field conditions. The simplification of the material properties such as ignoring plastic property of material or not assuming the temperature dependency of materials or ignoring IMC layers are seen in most of the published works for the FEM simulation of PV modules. For example, the material properties for the main interconnection component such as copper and even solder are generally assumed linear elastic; then, the results (in some cases the established formulas) are only valid for the early elastic states (Wang, et al., 2016). To answer the questions on more relatively exact failure mechanism of different component of PV module and particularly ribbon interconnection; it is necessary to develop much more extensive models consist of considering all important nonlinearities of the interconnection materials and also the structural details. Therefore, understanding all aspects of the failure modes and implementing the simulation with real assumptions and sufficient details can be remarkably helpful to achieve accurate results; and then to reach an optimized interconnection design with high efficiency but with low manufacturing cost.

3.2. Numerical Approaches

This section depicts the details of the FEM simulation used to investigate the crack initiation/propagation in the PV module solder joint interconnections subjected to the lamination process; and also to estimate the creep-fatigue life of the solder joints. Both studies are implemented in ABAQUS 2019 which enables to study the different aspects of the fracture mechanics such as crack analysis and fatigue evaluation.. This study also considers main nonlinearities of the models such as plastic behaviour of the materials, temperature dependency of the materials and also modelling the brittle IMC interface layer at the border of the solder joints.

3.2.1. Crack Initiation and Propagation

To determine the crack initiation temperature and crack growth rate in the PV module solder joint interconnections, the XFEM feature in ABAQUS 2019 is used. The XFEM is a numerical technique which extends generalized (ordinary) finite element method (GFEM) focusing on the crack propagation and it is introduced by Belytsckho and Black in 1999 (Belytschko & Black, 1999). The XFEM is based on the GFEM and the partition of unity method (PUM), and this numerical technique extends the GFEM and allows local enrichment discontinuous functions to be combined with the numerical approximation (ABAQUS, 2019). Indeed, the special enriched functions in conjunction with additional degrees of freedom are used to ensure the presence of discontinuities such as crack and inclusions in structure, and then to find the discontinuity of system variables.

Unlike ordinary FEM, with the XFEM method there is no need to define the crack location, path or initial crack beforehand and these solution dependent crack geometry specifications can be obtained through the approach. In effect, the XFEM models a crack within an enriched element by adding degrees of freedom in elements with special displacement vector functions. Also, in the GFEM, singularities near crack tip (boundary layers) can only be solved by requiring mesh refinement in the regions with the significantly large gradients of the fields, however, the XFEM does not require to update the mesh topology and it facilitates stress intensity factor computations even on relatively coarse meshes, and further-more, no re-meshing is required for crack growth simulations. This means that while the XFEM is generating discontinuous fields along a crack and around its tip, there is no need for modelling the geometry of crack and re-meshing in the simulation (ABAQUS, 2019). Figure 18 compares the mesh refinement in a cracked plate simulated using the ordinary FEM (with an adaptive mesh refinement) and the XFEM technique (with a uniform mesh) (Khoei, 2014).

The figure is redacted for the public view due to lack of permission of the copyright holder.

Figure 18: Schematic views of crack discontinuities in a plate with a hole and initial crack under tension load: (a) Initial crack simulated in the plate with a hole plate with a hole; (b) Crack propagation in the plate using the ordinary FEM (with an adaptive mesh refinement); (c) Crack propagation in the plate using the XFEM technique (with a uniform mesh and no mesh refinement) (Khoei, 2014).

To explain details of the XFEM crack analysis, the enrichment discontinuous functions include the asymptotic functions that capture the singularity near crack tip, and a discontinuous function that represents the jump in displacement vector across the surface of crack. The approximation for a displacement vector function, u, with the partition of unity enrichment is shown in Equation #1 (ABAQUS, 2019).

$$\mathbf{u} = \sum_{I=1}^{N} N_I(x)\left[\mathbf{u}_I + H(x)\mathbf{a}_I + \sum_{\alpha=1}^{4} F_\alpha(x)\mathbf{b}_I^\alpha\right] \qquad Eq.1$$

where, $N_I(x)$ is the nodal shape functions; u_I is the nodal displacement vector associated with the GFEM solution (the product of $N_I(x)$ and u_I required to be considered for all model nodes); $H(x)$ is the associated discontinuous jump function; a_I is the nodal enriched degree of freedom vector; (the product of $N_I(x)$, a_I and $H(x)$ is the jumped displacement vector across the crack surfaces); $F_\alpha(x)$ is the associated asymptotic crack-tip function; and b_I^α is the nodal enriched degree of freedom vector (the product of $N_I(x), F_\alpha$ and b_I^α represent the jumped displacement vector at the nodes near crack tip).

Assuming x is a sample point, x^* is the point on the crack closest to x, and n is the unit outward normal to the crack at x^*; $F_\alpha(x)$ can be found as shown in Equation #2.

$$\mathrm{F}_\alpha(\mathrm{x}) = \left[\sqrt{\mathrm{r}}\sin\frac{\theta}{2}, \sqrt{\mathrm{r}}\cos\frac{\theta}{2}, \sqrt{\mathrm{r}}\sin\theta\sin\frac{\theta}{2}, \sqrt{\mathrm{r}}\sin\theta\cos\frac{\theta}{2}\right] \qquad Eq.2$$

where r and θ are the radial and angular components for the local polar coordinate system in a two-dimensional field. Also, the associated discontinuous jump function, $H(x)$, is a modified Heaviside function which is shown in Equation #3. Figure 19 shows the variable vectors of the associated discontinuous jump (Heaviside) function corresponding to the crack discontinuity across the surface of crack and the crack tip. The detailed formulations and further information for the XFEM can be found in (Mohammadi, 2008) and (Moës, et al., 1999).

$$H(x) = \begin{cases} 1 & \text{if } (x - x^*) \cdot n \geq 0 \\ -1 & \text{otherwise} \end{cases} \qquad Eq. 3$$

The figure is redacted for the public view due to lack of permission of the copyright holder.

Figure 19: Vectors of the associated discontinuous jump function corresponding to the crack discontinuity.

The XFEM fracture theory uses the cohesive traction-separation law to simulate the fracture mechanics in the materials, in which different strain and stress components (MAXPS / MAXPE[1], MAXS / MAXE [2] and QUADS/ QUADE[3]) can be used to control damage initiation. In this study, The XFEM feature of the ABAQUS 2019 is employed for determining the critical temperature for micro-crack initiation and growth in the PV module solder joint interconnections. To investigate the damage initiation, the maximum nominal stress (MAXS) is considered as the controlling parameters of the traction-separation laws. This means that the damage (crack) is initiated when the nominal stress exceeds the strength limit (maximum stress in shear and normal directions). Then, the initiated crack (in plane strain elements) is progressed according to the fracture energy formulations based on the parameters of fracture toughness (the critical stress intensity factor) and elastic coefficients (Young's modulus and Poisson's ratio) as follows (Du, 2009):

---

[1] Maximum principal stress (MAXPS) and maximum principal strain (MAXPE)

[2] Maximum nominal stress (MAXS) and maximum nominal strain (MAXE)

[3] Quadratic nominal stress (QUADS) and quadratic nominal strain (QUADE)

$$G = \frac{(1 - \nu^2)\, K^2}{E} \qquad Eq.4$$

where, G is the energy release rate ($unit$: $\frac{mJ}{mm^2}$), K is the fracture toughness (unit: MPa×$m^{0.5}$), E is Young's modulus (unit: MPa) and ν is Poisson's ratio (unit less).

The XFEM formulation can work accurately when the material imposed to be cracked, is based on the theory of Linear Elastic Fracture Mechanics (LEFM). This means that when a material has a brittle behaviour and it exhibits cracking in the elastic region (before experiencing the plastic behaviour), the XFEM can appropriately predict the crack initiation, crack propagation. For materials with elastic-plastic behaviour, the XFEM can also estimate the crack behaviour, but not as well as the possible estimation for the materials with elastic behaviour (ABAQUS, 2019) and (Mohammadi, 2008). The IMC interface layers in the PV module solder joint interconnection exhibits a very brittle material behaviour, so, in this study, the linear elastic behaviour is assumed for the IMC layers between solder and silver (connection pad) materials and also between solder and copper materials. However, for all other metallic materials in the PV module ribbon interconnections are considered to have plastic behaviour.

3.2.2. Numerical Approach for the Creep-Fatigue Analysis

The empirical energy based models for estimating the creep-fatigue life of SAC solder joints have been developed by Syed. In this approach, he correlated the experimental data obtained the results of the FEM simulation to derive the formulation for prediction of the thermal creep fatigue life of SAC solder joints (Syed, 2004). In this study, a developed Morrow Energy Density model (based on the total strain energy density) is used to determine the number of thermal cycles to failure (N_f). This model uses the stress–strain hysteresis energy loops for predicting the creep energy in each cycle. The strain-stress terms used in the models can be found by using the analytical constitutive models of creep behaviour such as Hyperbolic Sine (Akay, et al., 2003) and (Steinhorst, et al., 2013) and (Syed, 2004).

Previous studies on the failure of solder materials shows that solder joints exhibit elastic, bilinear kinematic hardening plastic behaviour after yielding (Che & Pang, 2004). The Hyperbolic-Sine creep model is perhaps, one of the most widely reported in the literature for investigating the effect of temperature and strain rate on the elastic plastic creep behaviour of materials. The results for stress/strain from the simulation of the PV module solder joint interconnections using Hyperbolic-Sine creep model can be used to estimate the number of cycles to failure. In this study, the Hyperbolic-Sine creep model in ABAQUS 2019 is used to find the total dissipated energy in the solder joints for different ribbon interconnection designs. The total dissipated energy extracted from FEM simulation is used to find the mean number of cycles to failure for the solder joints using Coffin–Manson–Arrhenius reliability formulation.

The modified Coffin–Manson–Arrhenius lifetime model is one of the most widely used approach for studying the behaviour of materials under thermal cycling fatigue; and has been used for predicting the creep life of the solder joints. The solder joint fatigue failure is the mechanical degradation of the solder material due to deformation under cyclic loading and this is known to occur at stress levels below the normal yield stress of solder due to either repeated temperature fluctuations, or mechanical vibrations, or mechanical loads (or combined temperature fluctuations, vibrations and loading). However, in the Coffin-Manson method, the cycling temperature is considered as the main parameter that affects the creep fatigue life. Previous studies have reported on the use of the Modified Coffin-Manson-Arrhenius model for estimating the number of cycles to failure of solder joints for different cycling temperature ranges (Samavatian, et al., 2020) and (Guyenot, et al., 2011). Held reported on the creep behaviour of the solder joints under fast thermal cycling test and they proposed a descriptive model based on the modified Arrhenius lifetime model for predicting the number of cycles to failure (N_f) for solder joints. The analytical formula that describes the relation between the number of cycles to failure, N_f and cycling temperatures (see Equation #5) has been reported by Held (Held, et al., 1997).

$$N_f = A * \Delta T^{\alpha} * \exp\left(\frac{Q}{RT_m}\right) \qquad Eq.5$$

where, N_f is the number of cycles to failure, ΔT is the cycling temperature (in kelvin, R and Q are the gas constant and internal energy, respectively, T_m is the mean cycle temperature (in kelvin), α is the exponent factor (dependent to the design) and A is a constant for the material.

Equation #5 can be used to determine the number of cycles to failure, N_f for each design of the solder joint interconnections when the value of exponent factor modified Coffin–Manson–Arrhenius lifetime model, α, is known. The value of α is related to the configuration and design of the solder joint. There are several studies to define α for the solder joints used in the electronic packages. However, there is not any specific study to determine the value of α and A for the PV module solder joint interconnections; and in some other research the value of α for other application of the solder joints is used rather than the true value of α for the PV module solder joint interconnections (Guyenot, et al., 2011). Using the arranged form of Equation #5, gives the relation between N_f and α and A in each thermal cycling load condition. To eliminate the constant A in the arranged form of Equation #5, two different thermal cycling loads with different temperature intervals (ΔT) can be compared (see Equation #6); and then arranged form of Equation #5 will be based on α and N_f for the compared ΔTs (see Equation #7). Thus, assuming two thermal cycling loads are the field and test thermal conditions, the exponent factor (α), can be found by rearranging Equation #5, as follows:

$$\frac{N_{f_{field}}}{N_{f_{test}}} = (\frac{\Delta T_{field}}{\Delta T_{test}})^{\alpha} * \exp\left(\frac{Q}{R}\left(\frac{1}{T_{m_{field}}} - \frac{1}{T_{m_{test}}}\right)\right) \qquad Eq.6$$

$$\alpha = \frac{1}{\ln\frac{\Delta T_{field}}{\Delta T_{test}}} \ln\left(\frac{N_{f_{field}}}{N_{f_{test}} * \exp\left(\frac{Q}{R}\left(\frac{1}{T_{m_{field}}} - \frac{1}{T_{m_{test}}}\right)\right)}\right) \qquad Eq.7$$

To find the α by using Equation #7, it is required to define N_f for the field and test thermal conditions. Syed et. al, developed a formula to estimate the creep-fatigue life of solder alloys joint by correlation of the creep fatigue damage data obtained from experimental studies with the FEM results (i.e. accumulated creep strain and energy density per cycle) (Syed, 2004). Based on the developed approach, the mean number of cycles to failure (N_f) for the solder joints under thermal cycling loads can be calculated from the following equation:

$$N_f = C(w_{acc})^{\eta} \qquad Eq.8$$

where C and η are the energy density constants for failure and w_{acc} is the average accumulated creep energy density (per cycle). For the SAC solder joint the value for C and η are reported 526 (1/0.0019) and -1, respectively (Syed, 2004). The average accumulated creep energy density for the solder joint elements in the contact between interconnecting materials is then given by the following equation:

$$w_{acc} = \frac{\sum W_i V_i}{\sum V_i} \qquad Eq.9$$

where i is the solder joint element number, V_i and W_i are the element volume and the accumulated creep energy for each element, respectively.

In this study, to find V_i and W_i, FEM simulation of the CR interconnection is used; and then, the exponent factor (α) for the PV module ribbon interconnection under any field condition, is found by comparing the correlated FEM results for different ΔTs) with the test condition.

For the FEM simulation of behaviour of the solder joint, the Hyperbolic-Sine creep model is used to find the accumulated creep (total dissipated) energy for different designs. The Hyperbolic-Sine creep model considers temperature and strain rate dependency of the material properties (H. Amalu & N.N. Ekere, 2016). Equation #10 shows the formula to express Hyperbolic-Sine creep model:

$$\dot{\varepsilon}_{cr} = A\left(\sinh(\beta\sigma)\right)^{n} exp\left(-\frac{Q}{RT}\right) \qquad Eq.10$$

where $\dot{\varepsilon}_{cr}$ is the scalar creep strain rate, A is Boltzmann's constant, β and n are constants, σ is the Von Mises effective stress, Q is activation energy, R is gas constant and T is the absolute temperature (Table 6 shows the value of these parameters for the SAC Solder).

3.3. Structure and Geometry of Models

Solar PV module is typically built up of different materials, including: silicon as the semiconductor material, EVA which serves as encapsulate materials to protect solar cells, aluminium sheet to envelop the backside of the silicon, the pasted silver-pads and fingers to receive the electrical current, Tedlar (Polyvinyl Fluoride) as a back sheet to cover the bottom, glass as front cover and the copper ribbon coated by solder materials to collect the electrical current from the individual cell. Figure 20 shows the schematic view of the assembly of the ribbon interconnections between solar PV cells in the module assembled by back to front connection method.

In this study the thickness of aluminium, silicon cell, EVA, glass and Tedlar layers used for the FE models are assumed to be 25µm, 200µm, 460µm, 3mm and 190µm, respectively. The thickness of other component parts such as silver-pad, copper, solder used and the ribbon interconnection width have been varied to investigate the effect of ribbon interconnection geometry and design on the crack initiation and propagation parameters and creep-fatigue analysis.

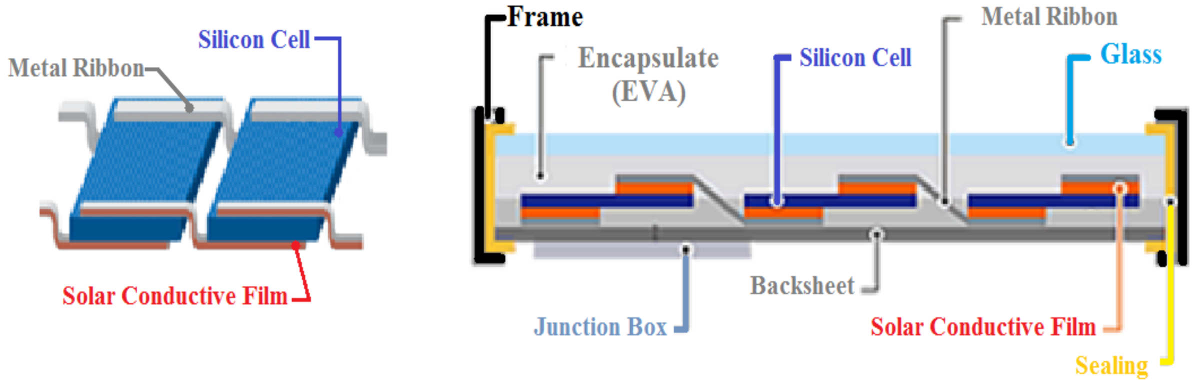

(a) **(b)**

Figure 20**:** Schematic view of the ribbon interconnections assembly between solar PV cells, (a) 3D view, (b) side view.

3.4. PV module ribbon interconnection dimensions

To have the equal electrical resistance of ribbon interconnections in c-Si cells tabbing, the summation cross-section area of all ribbon interconnections (the conventional ribbon, the MBB and the LCR interconnection) are considered to be same. For this, the number of ribbon interconnections in each design is taken into account to determine the generic dimensions of the copper core in the ribbon interconnections. For example, when the number of the ribbon interconnections for the LCR and the conventional designs are same, the cross-section area of the 200µm thick CR interconnections (with 3 ribbons) is equal to the cross-section area of the 250µm thick LCR interconnection (with 3 ribbons) and the MBB with 276µm diameter. Table 2 shows the common dimensional specification of PV module ribbon interconnection designs used in this study. Also, for each of the cell tabbing designs, other dimensions of the material interconnections (including solder thickness, silver-pad thickness, IMC layer thickness, and ribbon width/thickness) are changed to find the best design in terms of the thermo-mechanical reliability.

Table 2: Numbers and dimensions of the different PV module ribbon interconnection designs used in this study.

Cell Tabbing Design	**Conventional**			**LCR**		**MBB**
Number of ribbons	2	3	5	3	5	15
Ribbon width range (mm)	1.5-2	1.0-2.0	0.5-1.5	1.2-1.5	0.9-1.2	0.27-0.35
Ribbon width average (µm)	1750	1500	1000	1350	1050	313
Copper thickness range (µm)	200-300	150-250	150-200	200	100-200	270-357
Copper thickness average (µm)	250	200	175	200	150	313
Cross-section area of the copper (mm^2)	0.88	0.90	0.88	0.81	0.79	1.15
Cross-section area of the ribbon (with 20µm solder coating) (mm^2)	1.04	1.11	1.12	1.07	1.11	1.30

3.5. FEM Models

This section presents the FEM models used in this study for simulating the PV module ribbon interconnections. The material properties, the load and boundary conditions, the element discretization, and the validation for the simulation of the PV module ribbon interconnection are presented in this section.

3.5.1. Material Properties

Few of the reported analytical/numerical studies on the failure of the PV module solder joint interconnections have considered the modelling of nonlinearities in their investigation failure and most studies have only assumed linearity and early elastic states (Wang, et al., 2016). Similarly, in their consideration of the influence of the coefficient of thermal expansion (CTE) of the PV module materials on the stress level, most studies have assumed linear, fully elastic and temperature independent behaviour. The focus of this study is to incorporate nonlinearities and temperature dependence in the investigation of the impact of ribbon interconnection design on the reliability of solar PV modules. For a more realistic simulation, the metallic materials used in this study are assumed with elastic- plastic behaviour. The mechanical properties of the material used in the FEM simulation are presented in Table 3. Also, the temperature dependency of important material properties such as coefficient of thermal expansion of silicon and metallic materials and the Young's modulus and plastic behaviour of the solder joint material are considered for the FEM simulations in this study.

Table 4 shows the temperature dependency of PV module materials used in the FEM simulations of this study including the CTE for copper, silver, aluminium, SAC solder joint, IMC and silicon; Young's modulus and Plastic Stress for solder joint.

Table 3**:** Mechanical properties of material used in the FEM simulation of PV module ribbon interconnection.

Parameter (unit)	**Material**								
	IMC (Deng, et al., 2005)	**SAC Solder Joint** (Li, et al., 2009)	**Silver** (AZoM, 2001)	**Copper** (Jing, et al., 2015)	**EVA** (Cambridge University Engineering Department, 2003)	**Silicon** (Owen-Bellini, et al., 2015)	**Aluminium** (AZoM, 2005)	**Tedlar** (DuPont™, 2014)	**Glass** (Tippabhotla, et al., 2017)
Elastic Modules (GPa)	110	See Table 4	69	121	11	130	68.3	2.138	73.0
Poisson's Ratio (-)	0.3	0.35	0.365	0.34	0.499	0.28	0.34	0.4	0.235
Yield Stress (MPa)	-	-	43	121	12	170	85	41	-
Thermal Expansion Coefficient (ppm/k)	See Table 4	See Table 4	See Table 4	See Table 4	270	See Table 4	See Table 4	78	8.0
Plastic Stress-Strain Curve (MPa)	-	See Table 4	43@0.001 120@0.04	121@0.001 186@0.004 217@0.01 234@0.02 248@0.04	-	-	85@0.001 100@0.12	41@0.001 55@0.9	-

Table 4: Temperature dependent properties of PV module materials.

Temp. (**^{0}C**)	**CTE (ppm/k)**, Interpolated.						**Young's modulus (GPa)** (49-0.07*T)	**Plastic Stress (MPa)** at 0.001and 0.065 Plastic Strain, Interpolated.
	Copper (Taulaukian, et al., 1975)	**Silicon** (Sasi Kumar, et al., 2017)	**Silver** (Taulaukian, et al., 1975)	**Aluminium** (Taulaukian, et al., 1975)	**IMC** (Jiang, et al., 1997)	**SAC Solder** 21.3+0.017T (Li, et al., 2009)	**SAC Solder** (Li, et al., 2009)	**SAC Solder** (Siviour, et al., 2005)
0	16.22	2.35	18.67	22.50	17.7	21.3	49	71, 145
30	16.60	2.63	18.98	23.29	18	21.81	46.9	52, 131
60	16.91	2.87	19.20	23.85	18.3	22.32	44.8	16, 110
90	17.22	3.04	19.42	24.41	18.6	22.83	42.7	-
120	17.53	3.20	19.65	24.97	19	23.34	40.6	-
150	17.76	3.36	19.91	25.40	19.8	23.85	38.5	-

3.5.1.1. Special Material Properties for the XFEM Analysis

To meet the requirements of the theory of LEFM which is basis of the XFEM for investigation of crack propagation, the IMC layers between solder and silver pad/copper are assumed as a brittle elastic material; whilst all other metallic materials in the PV module (silver, copper and solder) are considered to have plastic behaviour. Based on cohesive traction-separation law method, the maximum nominal stress in the shear and tensile directions are considered as the controlling parameters for the damage initiation in the IMC layers. Table 5 shows the fracture characteristic (shear/tensile strength and fracture toughness) of the bonded metallic materials used in PV module ribbon interconnection including SAC solder joint, IMC layer, silver-pad , copper and aluminium.

Table 5: Fracture Material characteristic of the metallic materials of PV module ribbon interconnection.

Parameter (unit)	**Material**				
	IMC (Zhong et al., 2010)	SAC Solder (Li, et al., 2009)	Silver (AZoM, 2001)	Copper (Jing, et al., 2015)	Aluminium (AZoM, 2005)
Shear Strength (MPa)	27.6-1.95*H_{IMC}	30	120	248	60
Tensile Strength (MPa)	65	78	120	248	100
Fracture Toughness (MPa.m^0.5)	1.4	7	40	30	22

3.5.1.2. Special Material Properties for Creep-Fatigue Analysis

To simulate the creep behaviour of the solder joint in PV module interconnection, the Hyperbolic-Sine creep model is used for defining the stress/strain hysteresis loop and the total accumulated creep energy density. Table 6 shows the Hyperbolic-Sine creep model parameters for the SAC solder joint (see also Equation #10).

Table 6: Hyperbolic-Sine creep parameters for SAC solder (Schubertt, et al., 2003).

Symbol	Unit	unit	Value
$\dot{\varepsilon}_{cr}$	Scalar Creep Strain Rate	Sec. $^{-1}$	Found During Analysis
A	Boltzmann's Constant	J/K	1.381×10^{-23}
$\boldsymbol{\beta}$	Constant	MPa^{-1}	0.02447
n	Constant	-	6.41
$\boldsymbol{\sigma}$	Von Mises Effective Stress	MPa	Found During Analysis
R	Gas Constant	$\text{J}\cdot\text{Mol}^{-1}\cdot\text{K}^{-1}$	8.314
Q	Activation Energy	$\text{J}\cdot\text{Mol}^{-1}$	6500×R
T	Absolute Temperature	K	Changing During Analysis

3.5.2. Load Condition

3.5.2.1. Load Condition for the Lamination Process

For modelling the PV module interconnections during the lamination process, the thermal load is applied uniformly to the model as the temperature of all components of the PV module is assumed homogenous and the temperature is applied linearly by increments of 15^0C per minute. Indeed, the temperature is assumed to be linearly increased from ambient temperature (25^0C) to maximum temperature (150^0C) for the lamination process in manufacturing process. It should be mentioned that the potential residual stress in the solar PV cells resulted from the manufacturing processes before the lamination process is not considered (such as soldering step) in the present simulations. Indeed, it is assumed that the solar PV cell and the PV module interconnection experience the stress only during and after the high temperature lamination process.

3.5.2.2. Load Condition for the Creep-Fatigue Analysis

To simulate the PV module under thermal cycling creep-fatigue condition, the models are subjected to a homogenous thermal cycling load, with time history in accordance with the IEC 61215-2:2016 standard (see Figure 21) (IEC 61215-2, 2016). For this study, a minimum temperature of -40^0C and a maximum temperature of the 85^0C are considered for the thermal cycles. The cycles start at ambient temperature (25^0C) and then the minimum temperature is experienced after cooling the module with a rate of 100^0C per hour and then the temperature remains constant for 10 minutes (dwelling time). Following this, with a similar heating up rate (100^0C per hour), the temperature increases to jump up to 85^0C and again it remains without any change for another 10 minutes. After staying 10 minutes at the highest temperature of the cycle, the model starts to cool down to reach the ambient temperature and to finish the cycle and then immediately the second cycle starts with the same temperature oscillating of the first cycle.

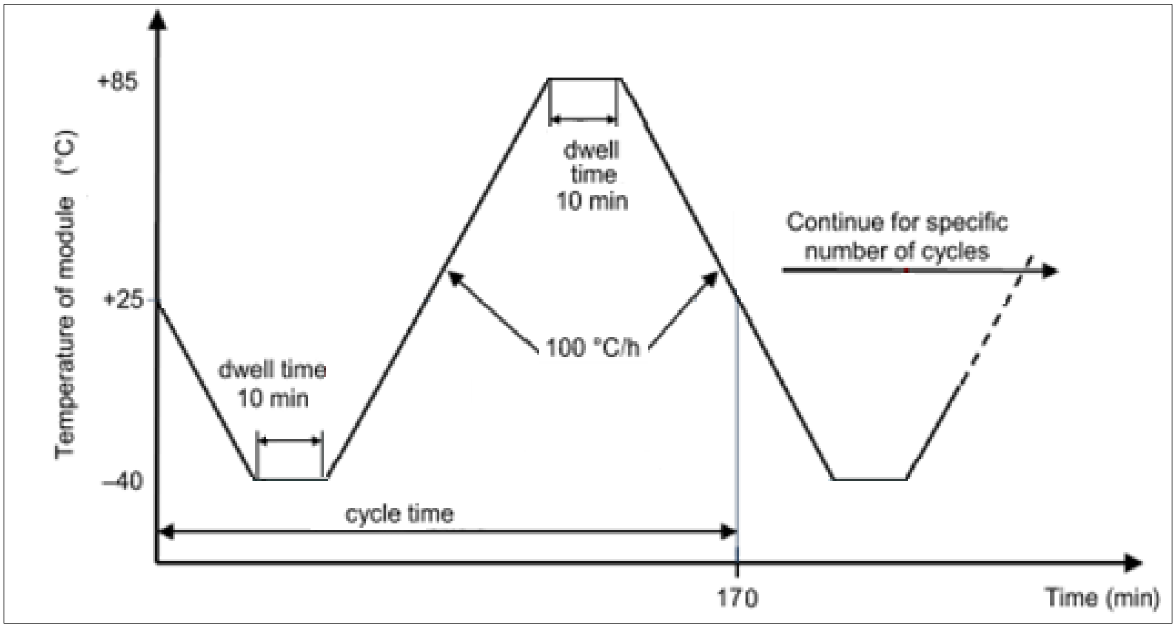

Figure 21: Applied thermal cycle amplitude in accordance with the IEC 61215-2:2016 (IEC 61215-2, 2016).

3.5.3. Boundary Conditions

In this study, to increase the computational solution speed, the two dimensional (2D) models using plane strain elements are considered for the simulation of the PV module interconnections since the geometry of the models have a high ratio of the interconnection length to the other dimensions of model and the strain distribution is almost similar in different cross-section of the cell. Also, the symmetry boundary condition is applied to the mid-points of the ribbon interconnection section and bottom-end of the Tedlar material is fixed displacement 0in thickness direction.

Figure 22 shows a schematic view of the cross-section of the CR interconnection showing the applied boundary conditions, the arrangement of component materials used for the FEM. For other ribbon interconnections (MBB and LCR interconnections) the same boundary conditions are also applied.

3.5.4. Element Discretization

The three-node linear plane strain triangle (CPE3) and four-node bilinear plane strain quadrilateral (CPE4) elements considered for the 2D FEM simulation of the ribbon interconnection used in this study. The IMC layers which are more probable to be cracked due to their brittle material behaviour; are modelled as the boundary layers of the solder joint materials. A very fine meshing technique is applied for the area near IMC layer (crack area in the solder joint material), in which the element size for the IMC layer is 1µm and the element size for the rest of solder joint is 4 µm. The size and the algorithm for the used fine meshing technique is found from comparing different meshing styles and sizes in which the used meshing style has the highest convergence of the strain distribution results in the PV module solder joint interconnection. Also, it should be mentioned that the mesh size influences on the crack initiation temperature since in the XFEM technique, the initiated crack length is according to the element size. Indeed, using finer mesh gives earlier crack initiation, but with lower crack length and using coarse mesh gives the initiated crack with a length of the propagated crack using finer mesh, Figure 22 also shows a schematic view of the materials mesh design used for the FEM simulation of the CR interconnection in PV module.

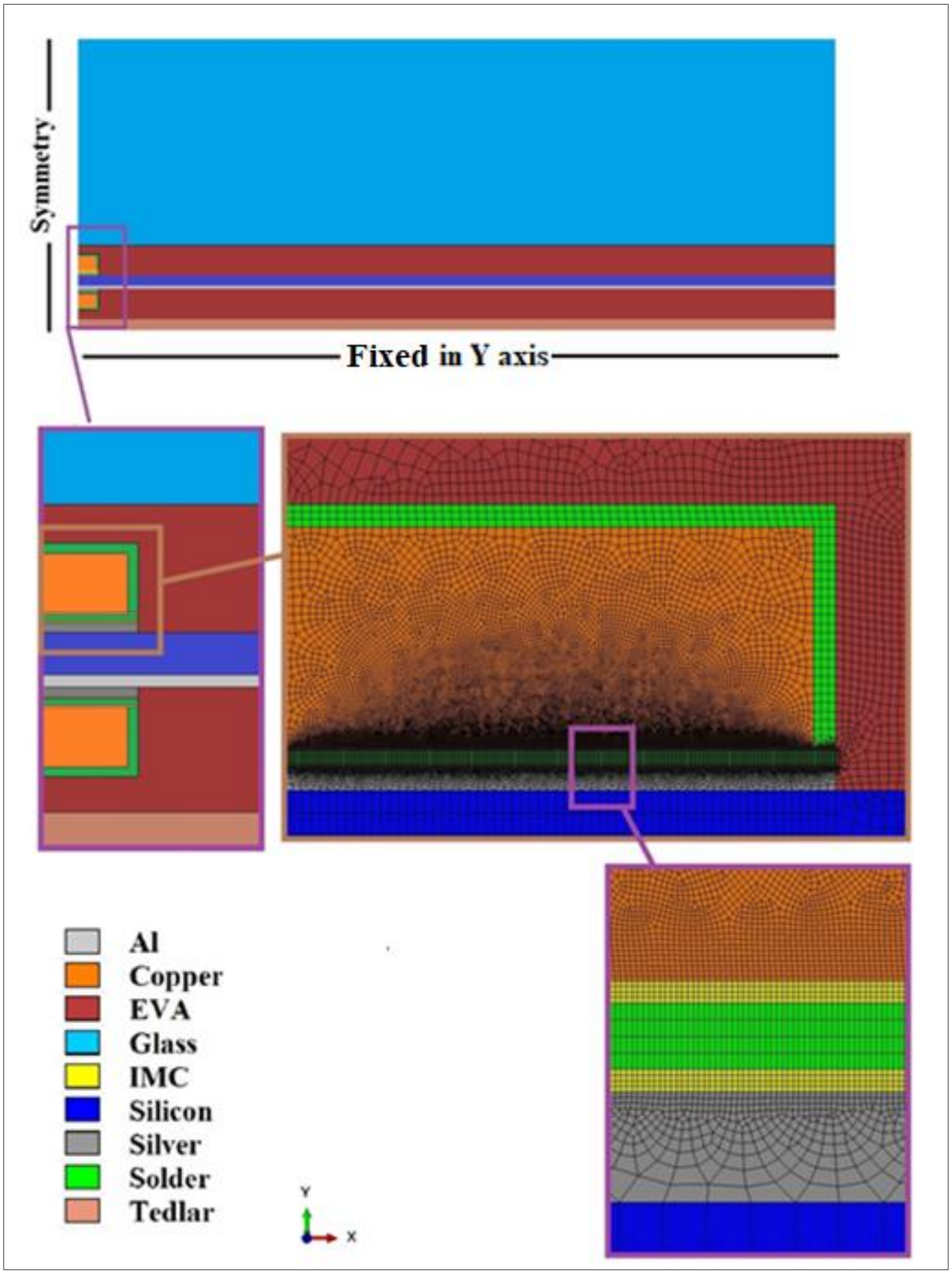

Figure 22**:** Schematic view of the 2D FEM simulation of the CR interconnection in with showing the boundary conditions, the arrangement of component materials and the materials mesh design.

3.5.5. Validation

This section presents the validation of the methodology used in this study (the XFEM technique and creep-fatigue models). For this, the results of the simulation methodology used in this study are compared with the published numerical and experimental results. The comparison of the results shows that very good agreements between the results are achieved which means that the simulation methodology, techniques, and the command setups of the software (ABAQUS 2019) are appropriately implemented.

3.5.5.1. Validation for the Analysis of Crack Initiation and Propagation

To validate the XFEM simulation , the results for crack initiation and propagation from an experimental work are compared with the results obtained from the present XFEM algorithm. The experiment has been applied for finding fracture mechanics of aluminium alloy (Al 1050) dog-bone specimen with square notch under uniaxial tension test. The Young's modulus, the Poisson's ratio, and yield stress for the used aluminium alloy are 70 GPa, 0.33 and 85 MPa, respectively. Also, the maximum principal stress of the material used in this case is 107.75 MPa and the fracture energy or the material is considered 3000 J/m^2 (Schiavone , et al., 2015). Figure 23 shows a schematic view of the specimen used for the validation of XFEM simulation. Also, details of the specimen dimensions are presented in Table 7. The top edge of specimen is subjected by uniform tension load (linearly increased from zero to 5000 N) and the bottom edge is fixed. Also, the symmetry boundary condition (perpendicular to the longitudinal axis) is applied to the specimen. The tension load is applied to the specimen until nucleation and propagation of crack which finally cause the section breakage. To ensure that there was no rate dependency on the results, the tensile tests were performed at three different extension rates: i.e. 1, 0.5 and 5 mm/min. Accordingly, the tensile load applied to the present XFEM simulation has 1 mm/min. It should be noted that, all setups implemented in ABAQUS 2019 such as 2D analysis setups, damage for traction separation laws and damage evaluation criterion are in accordance with the setups used in XFEM simulation of PV module interconnections (presented in Chapter 4 and Chapter 5). In addition, the minimum time step in the present simulation is considered 1e-12 second. It means that if the software cannot find a converge transient response for each increment with higher time steps, it automatically reduces the time step by the minimum time step to find the response, otherwise the analysis would be terminated if the minimum time step is not enough low.

The figure is redacted for the
public view due to lack of
permission of the copyright holder.

Figure 23: Schematic view of the specimen used for the validation of XFEM simulation (Schiavone , et al., 2015).

Table 7 Dimensions of the specimen used for the validation of XFEM simulation (Schiavone , et al., 2015).

Dimension	**Symbol**	**Value**
Gauge length	G	200mm
Width	W	40mm
Thickness	T	1mm
Radius of filler	R	25mm
Overall length	L	450mm
Length of reduced section	A	270mm
Length of grip section	B	75mm
Width of grip section	C	50mm
Notch Width	W_n	5.8mm
Notch Length	L_n	5.8mm

Figure 24 compares the results (Force-Displacement curve) from the present work using ABAQUS 2019 and also from other XFEM result and experiment during applying tension load to the one end of specimen (Schiavone , et al., 2015). Also, Figure 25 shows the crack initiation and propagation determined from the present work and from the previous XFEM and experiment works. As Figure 25 shows, the crack is initiated at the corners of notch in the specimen and the initiated crack at the bottom corner (is side of fixed end) is fully propagated across the mid-section.

Comparison of the present results with the results of previous works showed good agreement for both crack investigation and force-displacement curve (< 20). Hence, the XFEM technique setups in ABAQUS 2019 are accurately used to find the fracture mechanism and crack analysis for this study. So, the steps of simulation from this case study, is extended and applied to the XFEM simulation for the PV module interconnection designs; even they have different geometry and material properties.

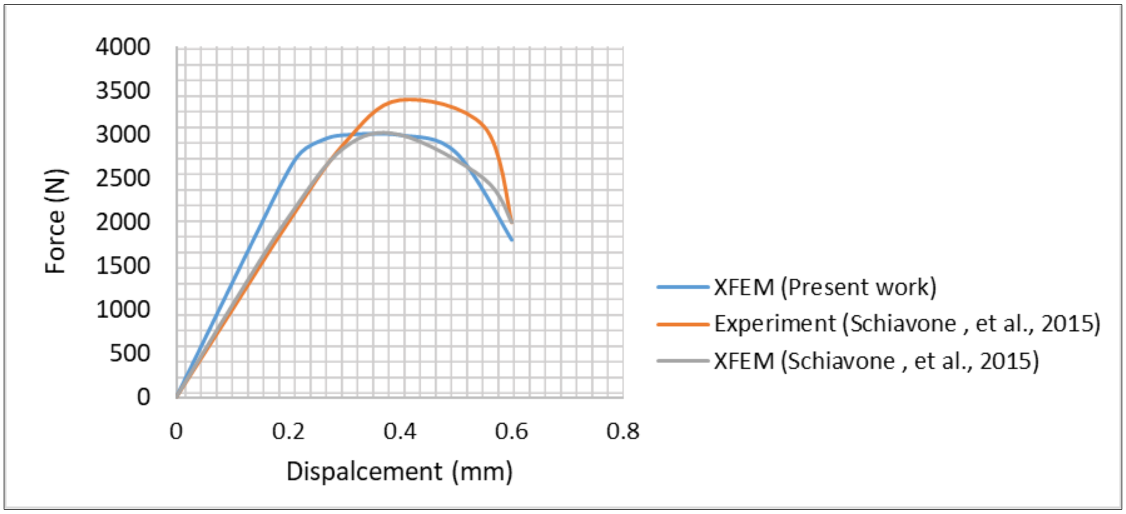

Figure 24: Force–displacement curves for the specimen under uniaxial tension (Schiavone , et al., 2015).

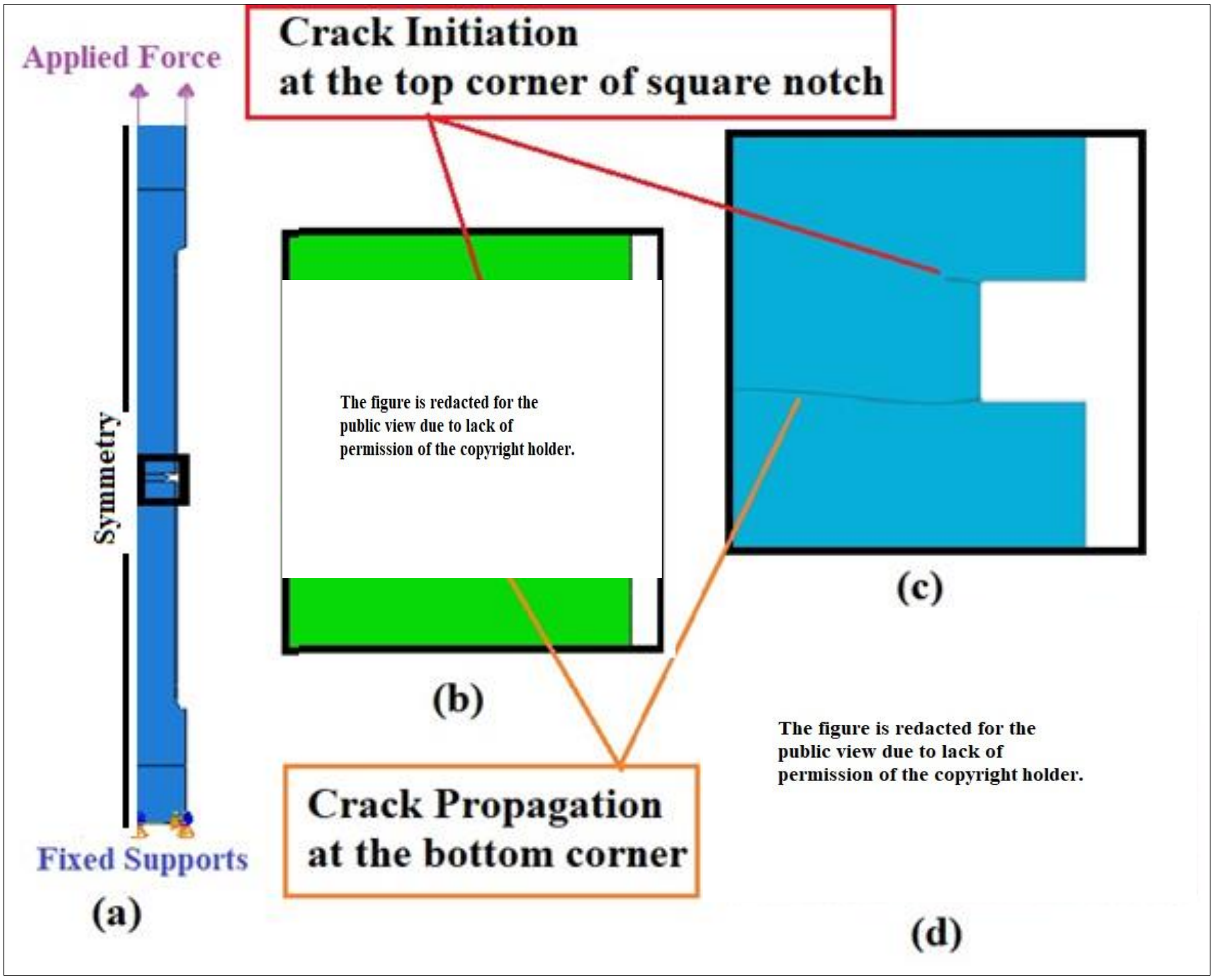

Figure 25: (a) assembly view of the FEM simulation of the specimen used for validation, showing boundary conditions, (b) crack at the notch corner, from the present XFEM work, (c) crack at the notch corner, from previous XFEM work (Schiavone , et al., 2015), (d) observed crack in the specimen (Schiavone , et al., 2015).

3.5.5.2. Validation for the Analysis of Creep-Fatigue Analysis

The creep-fatigue methodology used in this study (see Section 3.2.2) is validated by comparing the FEM results for the solder joint used in a Wafer Level Chip Scale Packages (WLCSP) with experimental and other numerical results. For this, 2D and 3D FEM models of the WLCSP (with a symmetry boundary condition) are implemented in ABAQUS 2019 (see Figure 26).

The model is designed according to the JESD22-B11 design guidelines with the board size 132x77x1mm (details for the dimensions of the WLCSP are shown in Table 8). Also, the solder joint dimensions used in the WLCSP model are presented in Table 9. A thermal cycling loading with a 10-minute dwell time is applied to the model. The temperature of cycle uniformly changes between the minimum temperature (-40°C) and maximum temperature (125°C) during 15 minutes; and that is according to the standard JESD22-A104D (JEDEC, 2009). Figure 27 shows the thermal loading profile applied to the model. All materials used in the WLCSP model are considered homogenous and isotropic in which the linear elastic behaviour is assumed for the materials, and only the Young's modulus of the solder joint is assumed temperature-dependent (Motalab M, 2013). In addition, the Garofalo-Arrhenius creep model (introduced in Section 3.2.2) is used for the SAC solder material, and the developed Morrow Energy Density model is used to estimate N_f. It should be mentioned that the lifetime model parameters used in the present creep-fatigue methodology are different with the lifetime model parameters used in the literatures. However, all investigations considered in this section use the same methodology (based on equation 8 in Section 3.2.2) for estimating the N_f. The lifetime model parameters used in these investigations are shown in Figure 26Table 10 compares the number of cycles to failure (Nf) estimated using the present methodology (introduced in Section 3.2.2) with the Nf reported in the literature from the experiment and the FEM simulations and . As Table 10 shows, there are good agreements between the estimated Nf using the present methodology in this research study and the Nf reported from the experiment. The results shows that 3D modelling of the WLCSP provides more accuracy for estimation of the Nf (with a 6% error) compared to 2D modelling (with a 9.8% error). The higher amount of error of the 2D modelling could be because the used creep-fatigue lifetime model parameters in the present methodology have been determined based on the investigation of the 3D FEM models. Another reason for the error is considering more simplifications in the geometry of model. Indeed, the 2D model is based on one slice of the 3D geometry and then it cannot consider the exact geometry details for the solder joint in the WLCSP FEM model. However, the geometry of solder joint in the PV module interconnection is very simpler than the geometry of solder joint in the WLCSP, and the cross-section of solder joint in the PV module interconnection is same for each slice of the model. So, it should be expected that using the 2D FEM model for the solder joint in the PV module interconnection can have less errors rather than the solder joints in the WLCSP. Although the results show that using the 3D model can provide more accurate estimation for the Nf, there is still a convincing accuracy for the estimation of the Nf using the 2D model. Hence, the 2D models used in this study can reasonably predict the creep-fatigue life of the PV module solder interconnection.

Table 10

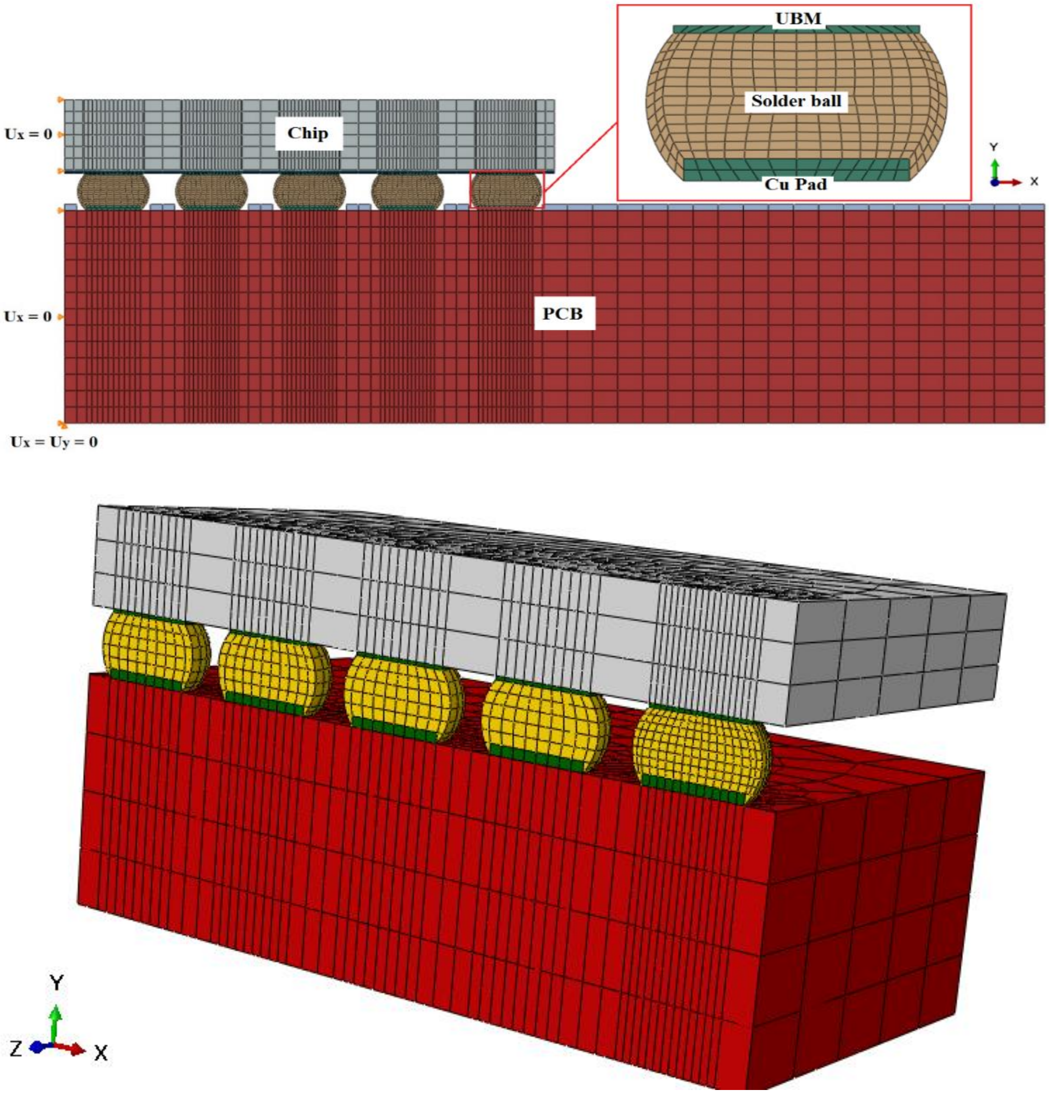

Figure 26: FEM view of the WLCSP model used for the validation of creep analysis, top: 2D FEM model, bottom: 3D FEM model (shown with symmetry in Z direction).

Table 8: Dimensions of the WLCSP model used for the validation of creep analysis (unit: mm×mm), (Tsou, et al., 2017).

Silicon Chip	Cu UBM	Cu pad	PCB
4 ×0.33	0.24 × 0.0086	0.22 × 0.025	8 ×1

Table 9: Dimensions of the solder joint used in the WLCSP model, Unit: mm, (Tsou, et al., 2017).

Diameter	Pitch	Height
0.25	0.4	0.166

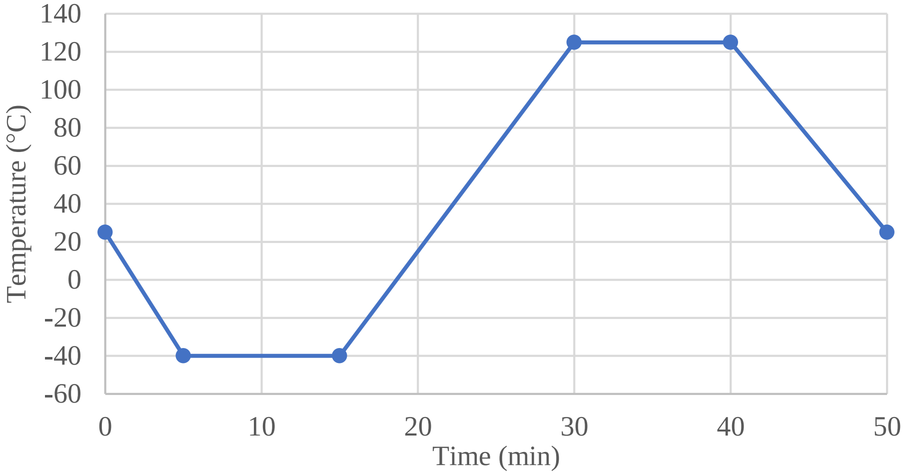

Figure 27: Thermal cycling profile applied to the WLCSP model.

Figure 28 compares the FEM simulation results from this study (for both 2D and 3D models) with the results from the published works (Hsieh & Tzeng, 2014) and (Tsou, et al., 2017) and (Lee & Chiang, 2019) referenced earlier. As Fig 28 shows, the corners of solder joint in contact with the chip has the maximum creep strain and creep dissipated energy density. Similarly, the results from the experiment (shown in Figure 28) depicts that the corners of the solder joint are cracked, and this means that the elements in these areas experience the highest creep strain energy density in the solder joint.

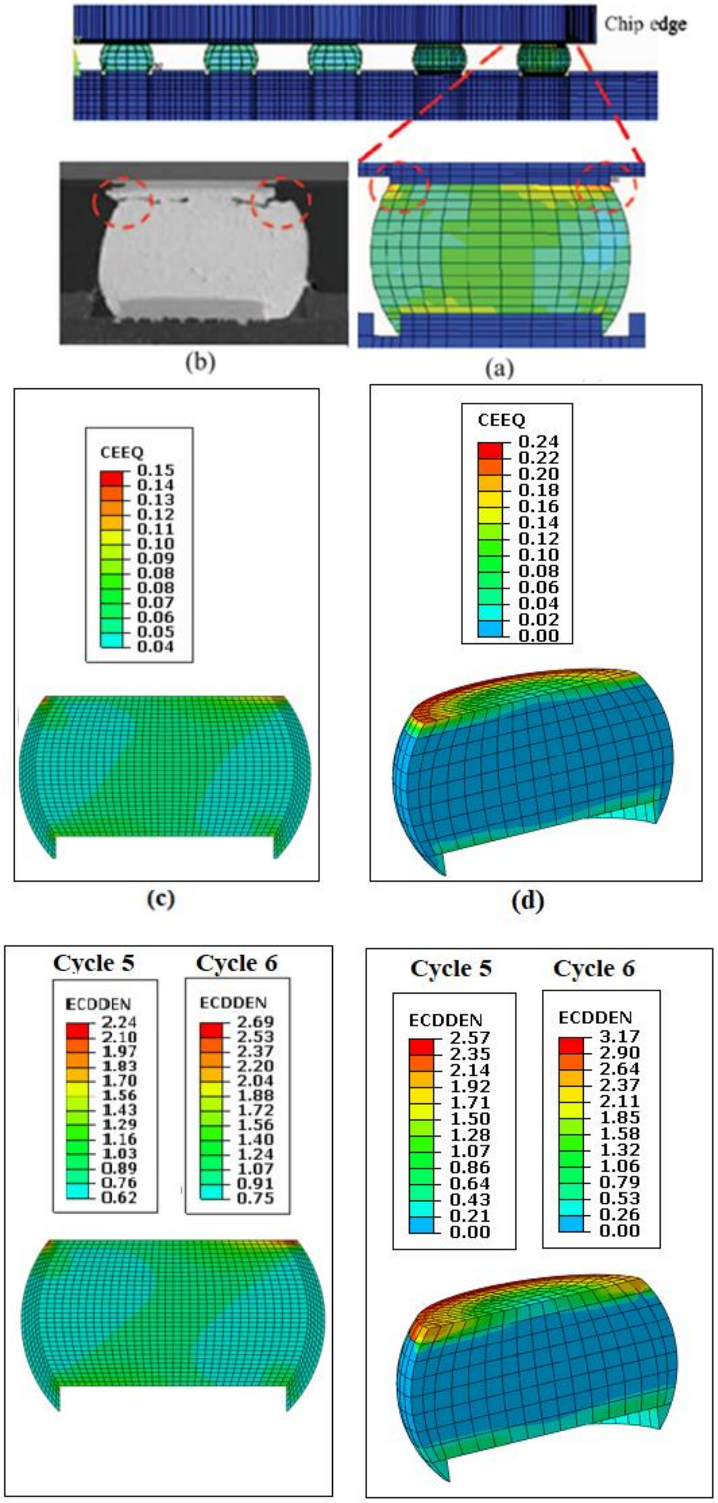

(b) (a)

(c) (d)

(e) (f)

Figure 28: (a) Equivalent creep strain after cycle 5 (CEEQ) in the corner solder joint of WLCSP, from previous 2D model (Tsou, et al., 2017), (b) observed failure in experiment (Hsieh & Tzeng, 2014), (c) CEEQ, from the present 2D model, (d) CEEQ, from the present 3D model, (e) total creep dissipated energy density (ECDDEN, in mJ/mm^3) after cycle 5 and 6 from the present 2D model, and (f) ECDDEN from the present 3D model.

Table 10 compares the number of cycles to failure (N_f) estimated using the present methodology (introduced in Section 3.2.2) with the N_f reported in the literature from the experiment (Hsieh & Tzeng, 2014) and the FEM simulations (Tsou, et al., 2017) and (Lee & Chiang, 2019). As Table 10 shows, there are good agreements between the estimated N_f using the present methodology in this research study and the N_f reported from the experiment. The results shows that 3D modelling of the WLCSP provides more accuracy for estimation of the N_f (with a 6% error) compared to 2D modelling (with a 9.8% error). The higher amount of error of the 2D modelling could be because the used creep-fatigue lifetime model parameters in the present methodology have been determined based on the investigation of the 3D FEM models. Another reason for the error is considering more simplifications in the geometry of model. Indeed, the 2D model is based on one slice of the 3D geometry and then it cannot consider the exact geometry details for the solder joint in the WLCSP FEM model. However, the geometry of solder joint in the PV module interconnection is very simpler than the geometry of solder joint in the WLCSP, and the cross-section of solder joint in the PV module interconnection is same for each slice of the model. So, it should be expected that using the 2D FEM model for the solder joint in the PV module interconnection can have less errors rather than the solder joints in the WLCSP. Although the results show that using the 3D model can provide more accurate estimation for the N_f, there is still a convincing accuracy for the estimation of the N_f using the 2D model. Hence, the 2D models used in this study can reasonably predict the creep-fatigue life of the PV module solder interconnection.

Table 10: Lifetime model parameters and estimated number of cycles to creep-fatigue failure (N_f) for the corner solder joint of WLCSP .

Lifetime model parameter $N_f = C(w_{acc})^{\eta}$	FEM Simulation (Tsou, et al., 2017)	FEM Simulation (Lee & Chiang, 2019)	Present FEM simulation for 3D analysis	Present FEM simulation for 2D analysis
w_{acc} (from FEM)	0.35	0.39	0.49	0.44
C	145	175	526	526
η	-2	-1.9	-1	-1
N_f	1152	1058	1074	1112
N_f from experiment (Hsieh & Tzeng, 2014): 1013				
Error for the N_f	13.7%	4.4%	6%	9.8%

Chapter 4

4. Study of High Temperature Crack in Conventional PV Module Solder Joint Interconnection

For any design of the interconnection ribbon, it is necessary to study the main failure modes to ensure the design is enough reliable. The main failure mode of PV module interconnection is failure of solder joint material that is caused by high accumulated strain energy due to the CTE mismatch between interconnection materials. The failure of solder joint becomes more important when the solar cell experiences high temperatures, particularly during the lamination in the manufacturing process which the cells need to be heated up to 150°C, to develop a network of EVA.

The focus of this chapter is on the study of high temperature crack initiation and propagation in the conventional PV module solder joint interconnection and is one of the four main components of the PhD Study as shown in Figure 10. The CR interconnections with different interconnection material dimensions are investigated to find the micro-crack initiation temperature and the crack growth rate during the lamination process.

4.1. Introduction

In spite of the best efforts of manufacturers to minimize and control thermomechanical stress effects on the PV module, the high temperature process can lead to high induced thermal stress in the PV module solder joint interconnections and the cells, which can lead to micro-cracks nucleation and propagation and subsequent interconnection failure. This can be explained by the fact that during the lamination process, the CTE mismatch between interconnecting materials results in high levels of stress and strain; and this accumulation of strain energy is responsible for the initiation of micro-cracks in the solder joint materials.

In this Chapter, we investigate the micro-crack initiation and growth in the lead-free solder joint material of the CR interconnections during the lamination process. The results of the study will be beneficial for researchers in predicting the propagation paths for existing micro-cracks during the thermal fatigue cycling under in-service PV module operating conditions; and hence for the predicting of PV module interconnection reliability. It concerns a necessary and fundamental revision of the manufacturing process. The XFEM technique in ABAQUS 2019 is used for this study as it enables the accurate solution of boundary value problems with discontinuities and singularities freely located within elements of the mesh (Fries, 2018).

4.2. Finite Element Modelling and Simulation

2D model of the CR interconnections with 3- and 4-node plane strain elements are used (see Section 3.5.5, Chapter 3) to find the crack initiation temperature and crack growth rate during the lamination process.

Different configurations of solar cell tabbing including ribbon the designs with 2, 3 and 5 CR interconnection are investigated (see Table 2, Section 3.4, Chapter 3). The ribbon interconnection width and thickness (i.e. copper thickness) changes are considered to find the best design in terms of the thermo-mechanical reliability. Also, the silver-pad thickness, solder thickness and IMC interface thickness changes are considered to achieve the best interconnecting material configuration for the design.

The FEM details of the simulation are presented in Section 5, Chapter 3. This includes the material properties of all interconnecting materials in which fracture material characteristics of the metallic materials are used for the implementation of the XFEM simulation (see Table 3,

Table 4 and Table 5 of Section 3.5.1 in Chapter 3). A uniform thermal load is applied to the model in which the temperature is linearly increased from ambient temperature (25^0C) to the maximum lamination temperature (150^0C) with the increments of 15^0C per minute (see Section 3.5.2.1, Chapter 3). Also, the symmetry boundary condition is applied to the mid-section of the model and bottom-end of the Tedlar layer is fixed in silicon cell thickness direction (Y axis) (see Section 3.5.4, Chapter 3). A schematic view of the FEM model for the conventional PV module interconnection is shown in Figure 22, Section 3.5.4, Chapter 3.

4.3. Results and Discussion

This section presents the results and analysis of the simulation modelling for CR interconnection configurations and design parameters. The crack location, the crack initiation temperature and crack growth rate are determined for each state. Our results show that the crack initiation temperature and crack propagation rate are quite dependent on the dimensions of ribbon interconnection. The effect of different PV module ribbon interconnection configurations and design parameters on the crack initiation temperature and crack growth rate are presented in the sub-sections below. For each group of simulations, the related design parameter is changed and the other design parameters are kept at the nominal values (see Table 2 in Section 3.4, Chapter 3).

4.3.1. Effect of Ribbon Width Change

Figure 29 and Figure 30 show the effect of changing the ribbon width on the crack initiation temperature and crack growth rate, respectively, for different solder thicknesses (silver-pad thickness, copper thickness and IMC thickness are considered as 50µm, 200µm and 4µm, respectively). The results presented in Figure 29 show that increasing the ribbon width leads to an increase in the crack initiation temperature for the ribbons with the width up to 1200µm; but for increases beyond the 1200µm limit the crack initiation temperature remains relatively constant. As it will be noted from Figure 29, increasing the solder thickness leads to a decrease in the crack initiation temperature. The investigation of the effect of solder joint coating on the crack initiation temperature and crack growth rate is separately presented in Section 4.3.3. It should be mentioned that the average increase of crack length in terms of temperature increase is considered to calculate the crack growth rate.

Our results presented in Figure 30 shows that the PV module solder joint interconnections experienced a sharp increase in the crack growth rate beyond the 1200µm width limit. The reason for this sharp increase in crack growth rate is that the crack nucleation location has moved from the IMC layer interface with the copper ribbon (the IMC-Copper) to the IMC layer interface with the silver pad (the IMC-Silver). In addition, our results show that the crack locations in now nearer the centre of ribbon interconnect width, but the crack propagation is still in same shear direction. The location and direction of the initiated crack is in line with the experimental results from the literatures (Jeong, et al., 2012) and (Li, et al., 2009). Figure 31 shows the location for the crack nucleation is at the edge of IMC layer interface with the copper ribbon and the propagation is in the shear direction; as the shear strength of the IMC layer material is lower than its tensile strength.

Based on the analysis of our results for both the crack initiation temperature and the crack growth rate for the ribbon interconnection geometries investigated, we will advise the use of ribbon interconnect widths of circa 900µm to 1000µm (for cell tabbing with 5 ribbons) or 1200µm (for cell tabbing with 3 ribbons), as this will lead to higher ribbon interconnection reliability for the PV module assembly. In addition, this recommendation will also lead to lower materials costs; as increasing the ribbon interconnection width leads to higher metallization and manufacturing costs. In addition to savings on metallization and materials costs, reducing the ribbon interconnection width helps to increase the solar PV module performance as the efficiency of the cell increases with the exposure of more silicon cell surface area to sun light.

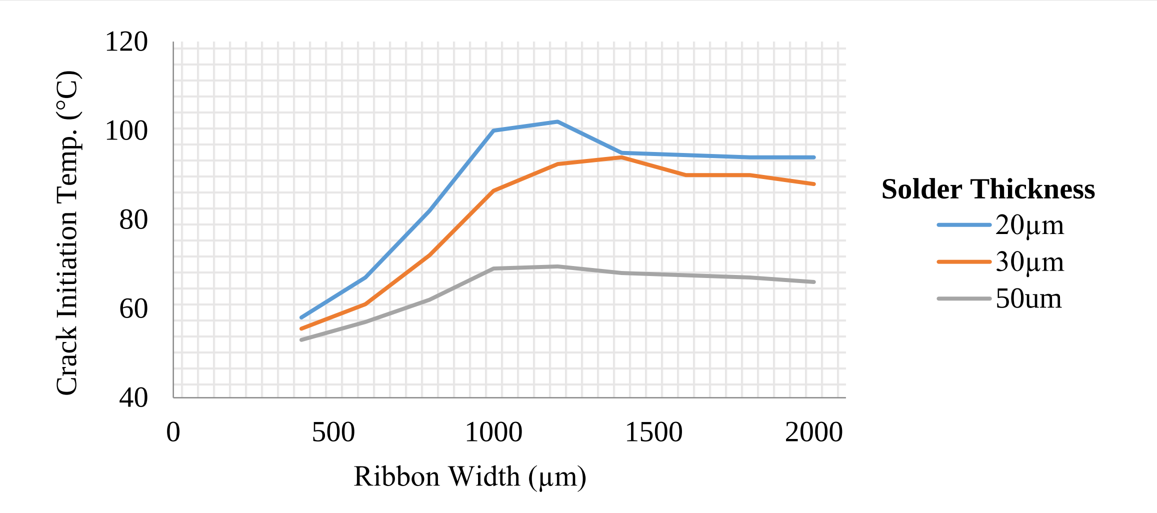

Figure 29**:** Effect of ribbon width on the crack initiation temperature for different solder thicknesses.

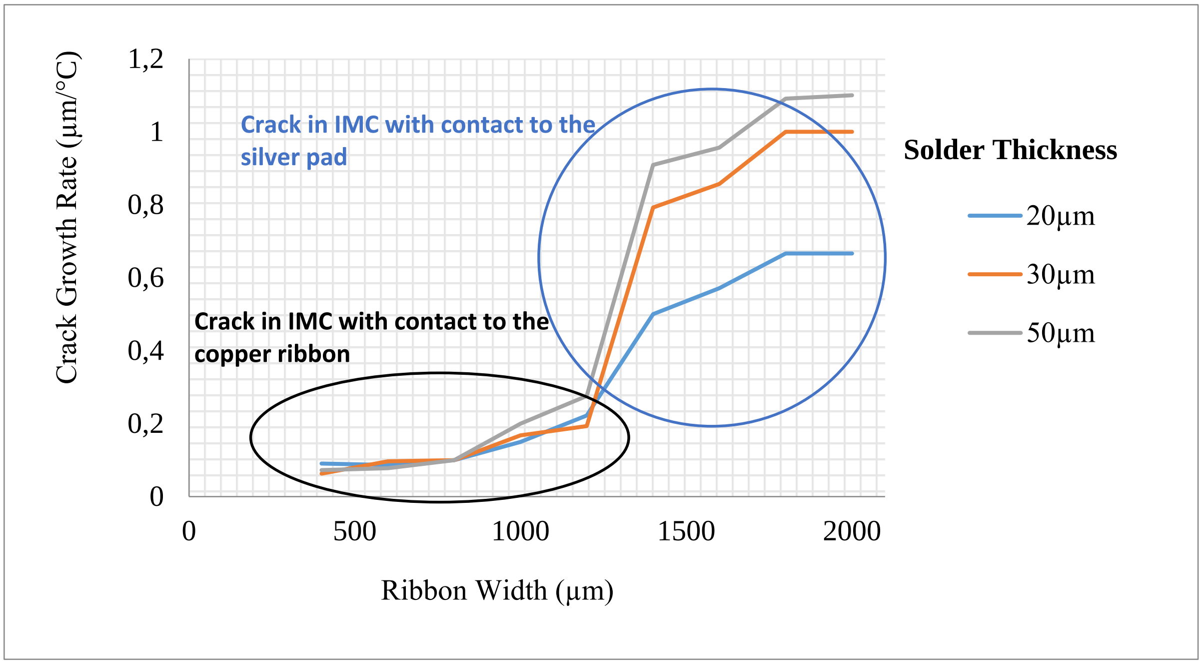

Figure 30**:** Effect of ribbon width on the crack growth rate for different solder thicknesses.

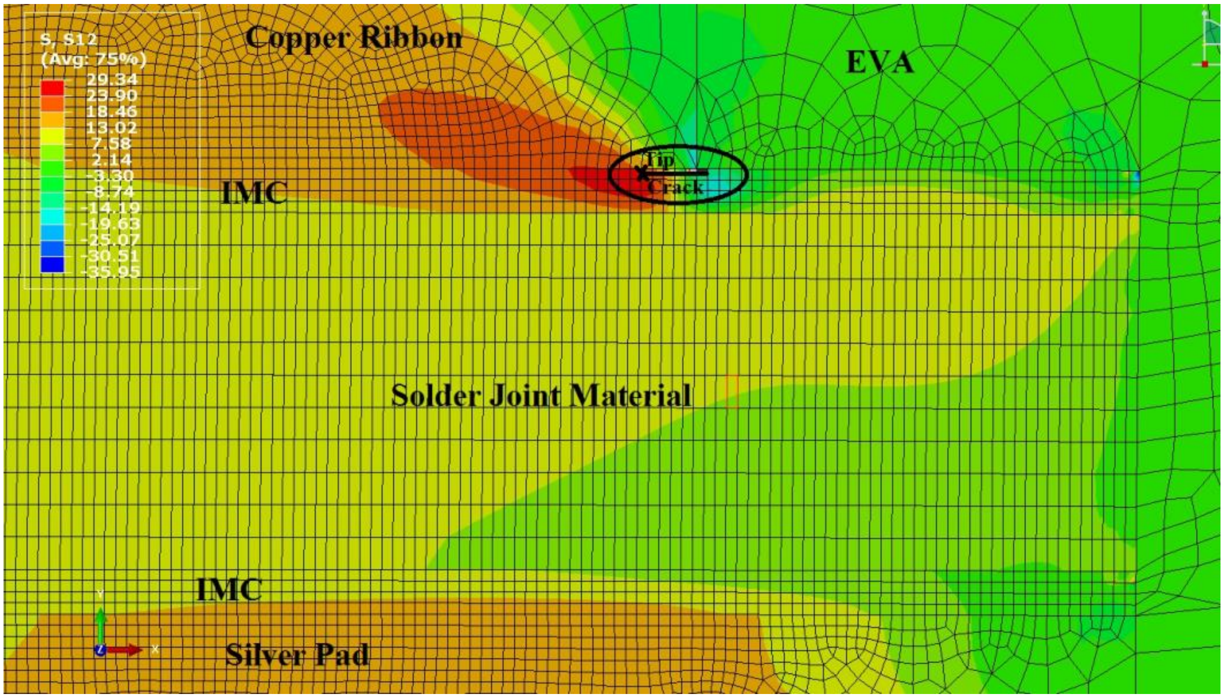

Figure 31**:** Crack's location and propagation direction in the IMC layer interface with the copper ribbon (shear stress, in MPa distribution contour is displayed).

4.3.2. Effect of Copper Thickness Change

The results of our study presented in Figure 32 and Figure 33 show the effect of copper thickness on the crack initiation temperature and the crack growth rate for the PV ribbon interconnection geometries investigated. The results in Figure 32 show that increasing the copper thickness leads to a decrease in the crack initiation temperature; and that reduction in the crack initiation temperature is more pronounced for the thicker solders. The results in Figure 33 also show that the lowest crack growth rate occurs at the 200µm copper thickness (the lowest point for all solder thicknesses). The results also show that the PV module solder joint interconnections experiences high crack growth rates for the copper thickness below 200µm, due to crack location in the IMC interface layer in contact with the silver-pad. Hence, the 200µm copper thickness is recommended for the PV ribbon interconnection as this gives the lowest crack propagation rate and better reliability.

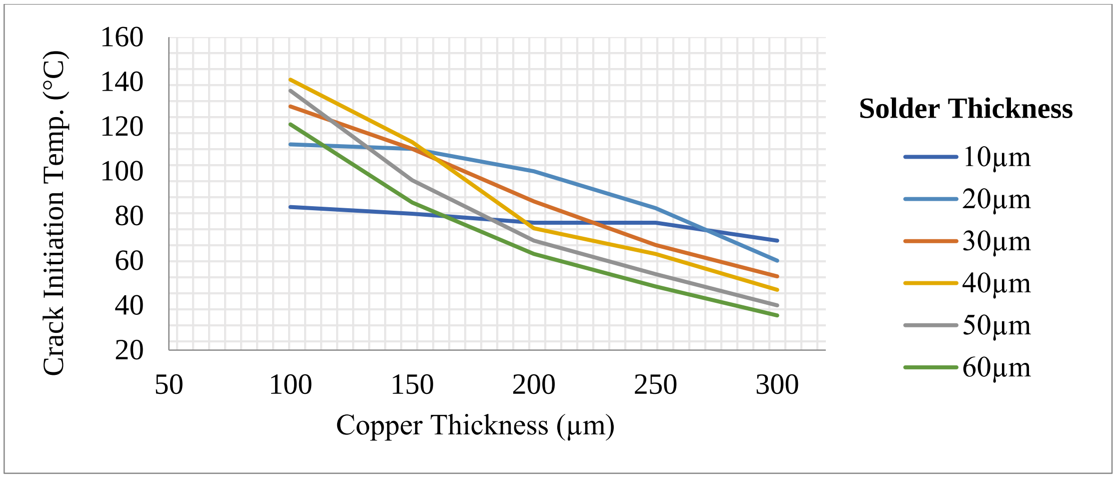

Figure 32**:** Effect of copper thickness on the crack initiation temperature for different solder thicknesses.

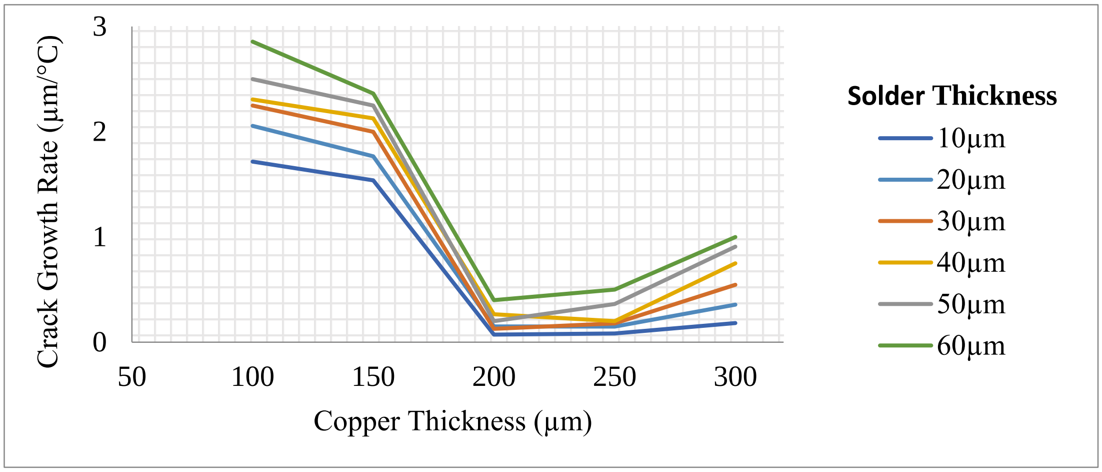

Figure 33**:** Effect of copper thickness on the crack growth rate for different solder thicknesses.

4.3.3. Effect of Changing Solder and IMC Thickness

The results from the presented FEM simulation showed that increasing the solder thickness leads to a decrease in the crack initiation temperature (circa linear relationship, see Figure 34); and this trend is the same for all the solder thicknesses investigated in our study, as it is discussed earlier in Section 4.3.1. As it is shown in Figure 34, the reduction in crack initiation temperature is more pronounced for thicker IMCs. This can be explained by the higher stress levels in the solder joint material and the strain accumulated in the IMC layer which results in crack initiation at lower temperatures. This result is not in line with the expectation that a thicker solder will result in higher interconnection reliability (a stronger solder joint that will be more resilient to premature failures).

Figure 35 presents a plot of the effect of solder and IMC thickness on the crack growth rate (silver-pad thickness, copper thickness and ribbon width are considered as 50μm, 200μm and 1mm, respectively). The results show that the crack growth rate is almost constant for the solder thickness under 50µm, but further increases in solder thickness beyond the 50µm limit leads to a big jump in the crack growth rate. Figure 35 shows that the crack growth rate is lower in the thicker IMC layers compared to thinner IMC layers. Based on the results of the study, presented in Figure 34 and Figure 35, a solder thickness of 20µm is recommended as this will help to keep the crack growth rate low and also keep the crack initiation temperature high; helping to increase the PV module ribbon interconnection reliability.

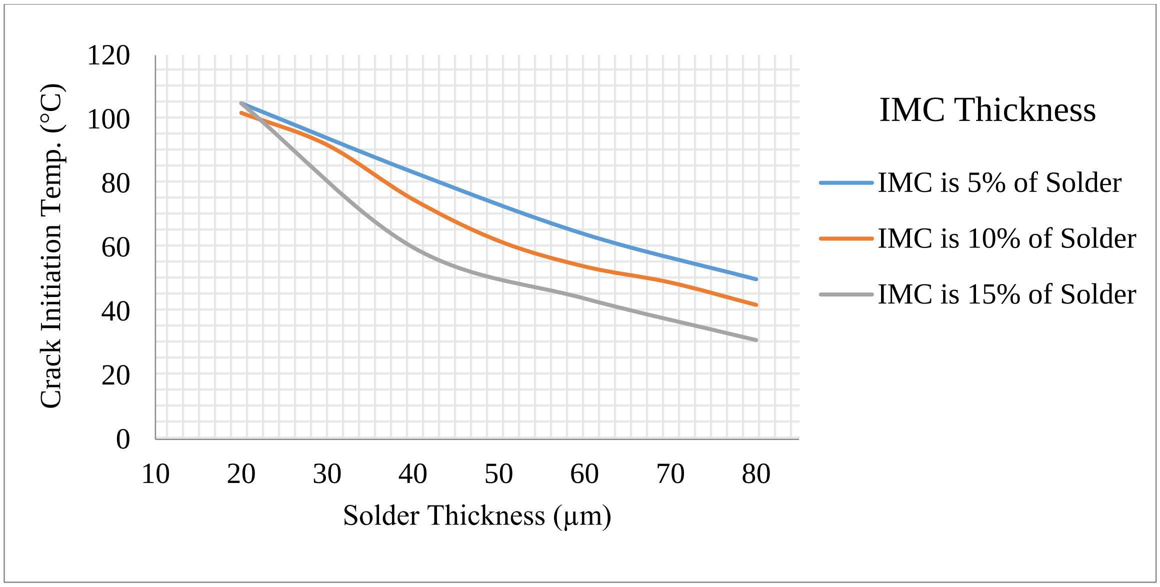

Figure 34**:** Effect of solder and IMC thickness on the crack initiation temperature.

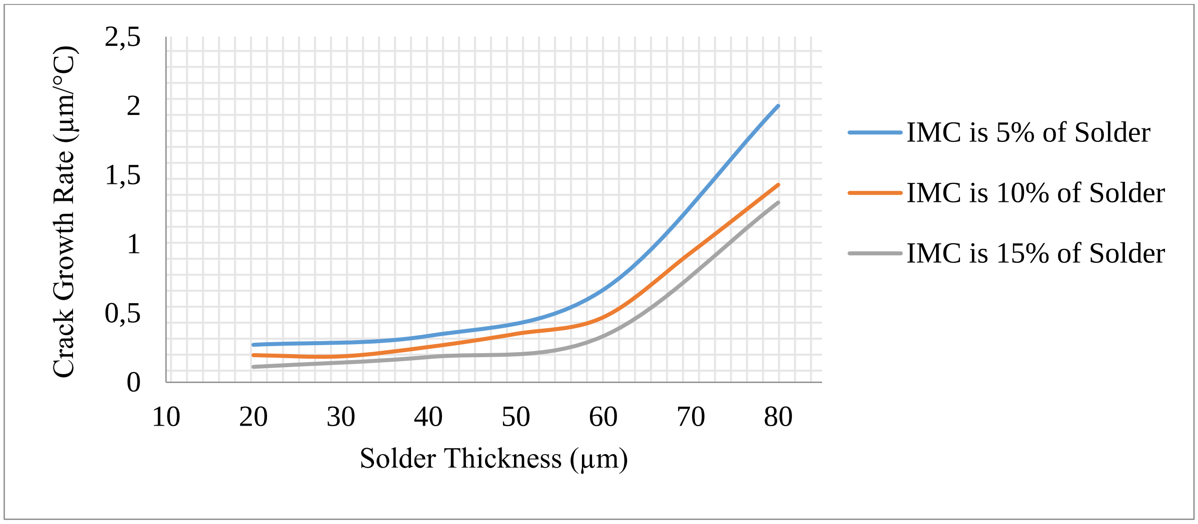

Figure 35**:** Effect of solder and IMC thickness on the crack growth rate.

4.3.4. Effect of Silver-pad Thickness

The results of our study presented in Figure 36 and Figure 37 show effect of silver-pad thickness on crack initiation temperature and the crack growth rate in the solder joints of the PV ribbon interconnection geometries investigated. The results show that crack initiation temperature and the crack growth rate decrease with increasing the silver-pad thickness. However, Figure 36 suggests that the crack initiation temperature for 20µm and 30µm solder thickness peaks at the silver-pad thickness in range of 30µm to 50µm before decreasing (copper thickness, ribbon width and IMC thickness are considered as 200µm, 1mm and 4µm, respectively). The results presented in Figure 37 shows that there is a significant change in the crack growth rate for silver-pad thicknesses less than 50µm; as the crack nucleation is located in the IMC-Silver. Based on the results of the ribbon interconnection geometries investigated in our study, the recommended solder thickness will be 20µm, and we recommend silver-pad thickness of between 40µm and 50µm which will help to achieve a higher ribbon interconnection reliability and lower material and manufacturing costs.

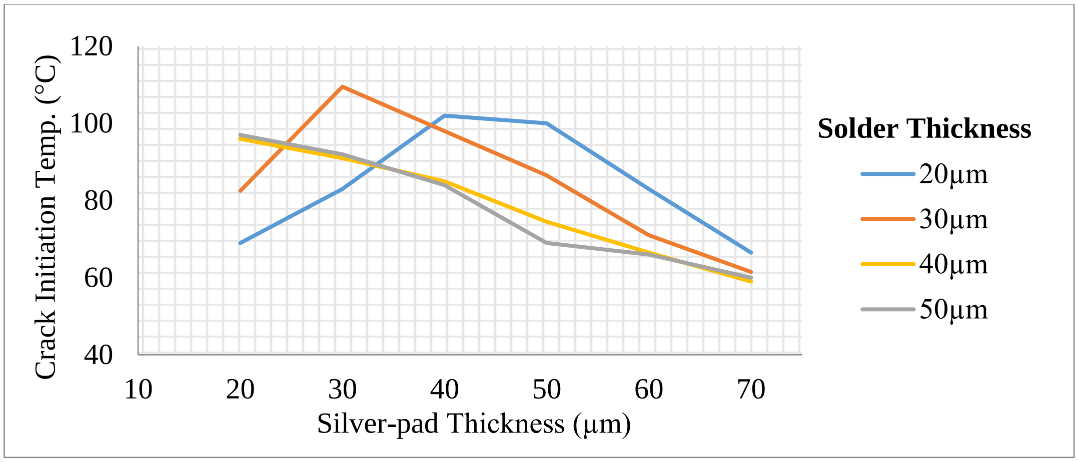

Figure 36**:** Effect of silver-pad thickness on the crack initiation temperature for different solder thicknesses.

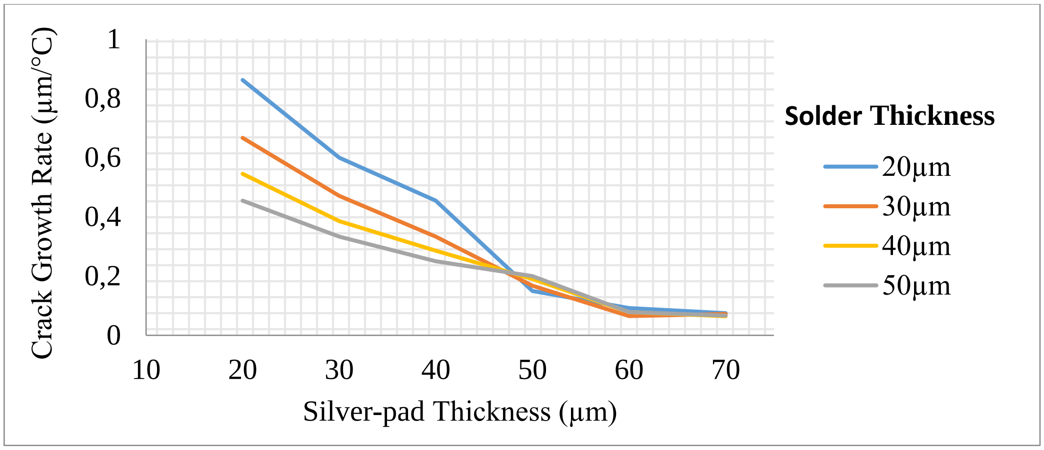

Figure 37**:** Effect of silver-pad thickness on the crack growth rate for different solder thicknesses.

4.3.5. Interaction between Copper and Silver-pad Thickness Change

Figure 38 shows the plot of the effect of changing both silver-pad and copper thickness on the crack initiation temperature in solder joints of the PV ribbon interconnection geometries investigated in the study (solder thickness, ribbon width and IMC thickness are considered as 20μm, 1mm and 4μm, respectively). This shows that reducing the copper thickness leads to an increase in the crack initiation temperature. The results also show that the silver-pads with thickness between 40μm to 50μm are recommended as this provides the higher crack initiation temperatures and hence better resistance to crack induces failures. Figure 39 shows the plot of the effect of changing the silver pad and copper thickness on the crack growth rates. The implication of the result in Figure 39 is that the crack growth rate for smaller silver pad thicknesses is significantly higher when compared with those for thicker silver pads. This is especially true for narrow copper ribbons, as in these cases the crack nucleated location is in the IMC-Silver pad.

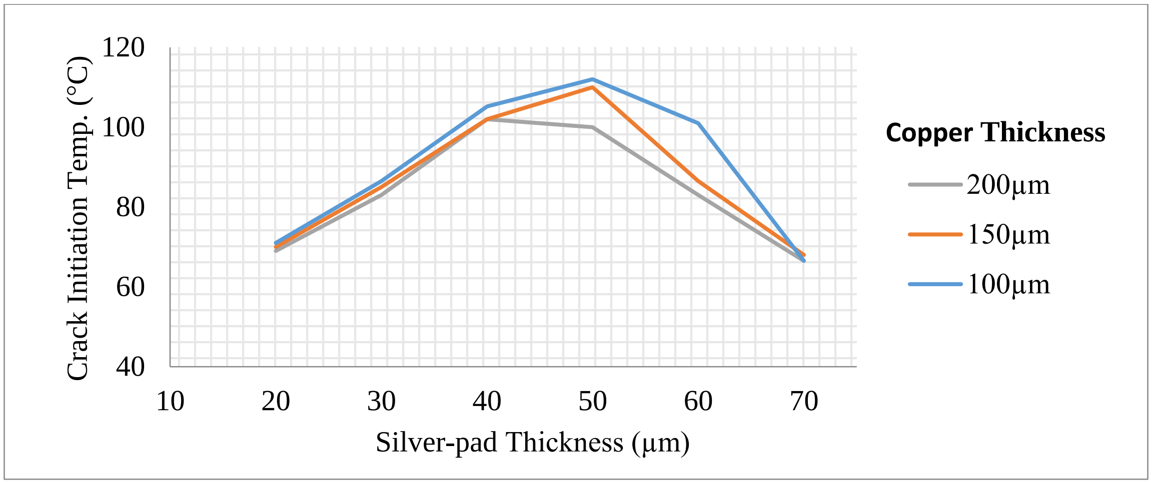

Figure 38: Effect of silver thickness on the crack initiation temperature for different copper thicknesses.

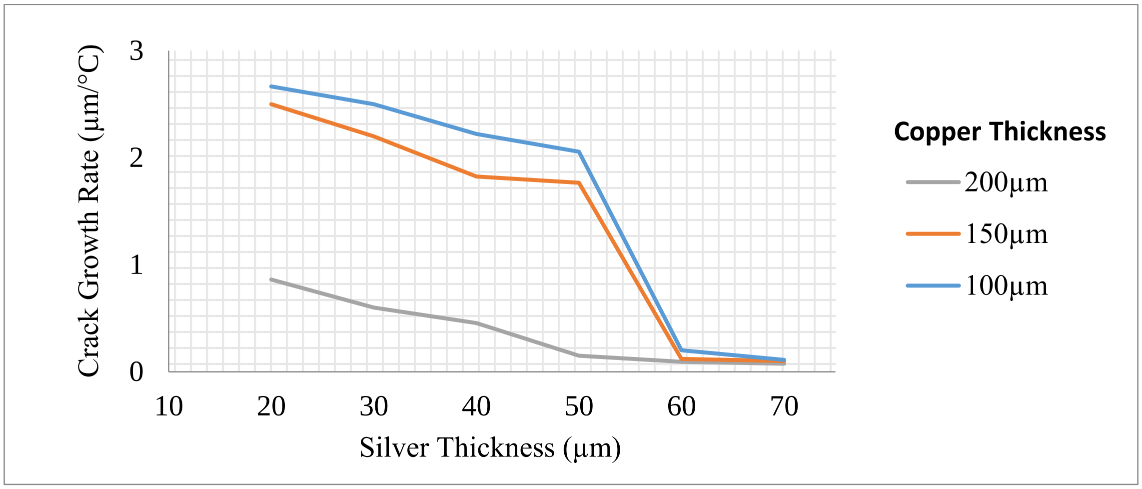

Figure 39: Effect of silver thickness on the crack growth rate for different copper thicknesses.

4.4. Chapter Summary and Conclusion

The XFEM in ABAQUS 2019 is employed to find the effect of geometrical dimensions of the PV module interconnection materials on the micro-crack initiation temperature and also the crack growth rate. The results show that PV module ribbon interconnection configuration has significant influence on the crack initiation temperature and the crack propagation rate; and consequently can adversely affect the PV module interconnection reliability. The results also show that micro-cracks are initiated at the edge of the IMC layer; and that cracks tend to propagate in shear direction and that crack growth rate is very dependent on the PV module ribbon interconnection geometry.

The main results of the study are summarized below:

- The crack nucleation is located in the IMC layer on the silver-pad side (the IMC-Silver) for ribbon interconnect configurations with copper ribbons widths greater than 1200µm, with copper ribbons thickness less than 200µm and with silver-pads thickness less than 50µm. For other configurations the crack nucleation is located in the IMC layer on the Copper side (the IMC-Copper). When the crack nucleation location is in the IMC-Silver, the crack growth rate is significantly higher, which increases the crack related failures and adversely affects the reliability of the PV module interconnection.
- Increasing the ribbon interconnection solder thickness leads to an increase in the crack growth rate (for solders greater than 50µm thick) and also a decrease in the crack initiation temperature (circa linear relationship); and this reduction in crack initiation temperature is more pronounced for thicker IMCs when compared to thinner IMCs. For this reason, a solder thickness of 20µm is recommended as this will help to keep the crack growth rate low and also keep the crack initiation temperature high; helping to increase the PV ribbon interconnection reliability.
- Increasing the ribbon interconnection width leads to an increase in the crack initiation temperature for widths up to 1200µm; but the crack initiation temperature remains relatively constant for increases beyond the 1200µm limit. Based on the analysis of the results for both the crack initiation temperature and the crack growth rate for the ribbon interconnection geometries investigated, we will advise the use of ribbon interconnect widths of circa 900µm to 1000µm (for cell tabbing using 5 ribbons) or 1200µm (for cell tabbing using 3 ribbons), as this will lead to higher ribbon interconnection reliability for the PV module assembly. In addition, this recommendation will also lead to lower materials costs; as increasing the ribbon interconnection width leads to higher metallization and manufacturing costs. In addition to savings on metallization and materials costs, reducing the ribbon interconnection width helps to increase the solar PV module performance as the efficiency of the cell increases with the exposure of more silicon cell surface area to sun light.
- The crack initiation temperature and the crack growth rate decreases with increasing silver-pad thickness (however, the crack initiation temperature for 20µm solder thickness peaks at the

silver-pad thickness in range of 30µm to 50µm before decreasing). The recommended solder thickness for ribbon interconnections is 20µm, and we also recommend silver-pad thickness of between 40µm and 50µm; which will help to achieve a higher ribbon interconnection reliability and lower material and manufacturing costs.

- Increasing the copper thickness leads to a decrease in the crack initiation temperature; and the reduction in the crack initiation temperature is more pronounced for thicker ribbon interconnection solders. The lowest crack growth rate occurs at the 200µm copper thickness; hence the 200µm copper thickness is recommended for PV module ribbon interconnections as this gives the lowest crack propagation rate and better reliability.

In summary, the results show that the crack initiation temperature and crack propagation rate are quite dependent on the dimensions of ribbon interconnection. For the different PV module ribbon interconnection configurations and design parameters investigated to establish the impact of interconnection geometry on the crack initiation temperature and crack propagation rate; a ribbon interconnection with 900µm to 1000µm (for cell tabbing using 5 ribbons) or 1200µm (for cell tabbing using 3 ribbons) copper width, with 200µm copper thickness, with 40µm silver-pad thickness and with 20µm solder thickness is recommended for low cost and high reliability solar PV ribbon interconnection.

The results of this chapter will be beneficial for researchers in predicting the propagation paths for existing micro-cracks during the thermal fatigue cycling under in-service PV module operating conditions; and hence for the predicting of PV module interconnection reliability.

These results investigate the effect of pairs of parameters while the rest are fixed at nominal values. Hence this study has not investigated the potential combined effect of simultaneously changing all parameters and the effect of interactions; but the main linear effects are established, and these are generally the dominant ones.

Chapter 5

5. Study of Crack Initiation and Propagation in New PV Module Ribbon Interconnections

This chapter presents the analysis for crack initiation and propagation in the new PV module ribbon interconnections (LCR and MBB interconnections) during the lamination process. The crack initiation temperature and crack growth rate for each configuration are found as main parameters to investigate the crack analysis, in which the design with higher crack initiation temperature (latent crack) and with lower crack growth rate is the optimum design.

Section 5.1 of this chapter focuses on the investigation of crack in the solder joint of different configuration of the LCR interconnection during the lamination process. For this investigation, different configurations of the LCR interconnection with changes of solder, silver-pad, copper thickness and also the change of ribbon width are considered.

Section 5.2, the chapter is on study of the MBB interconnection in the PV modules. Similar to Section 5.1 and also Chapter 4, thermal crack initiation and propagation in the solder joint of the interconnection are investigated, in which the effect of the non-homogeneity of the solder on the ribbons (resulting from manufacturing process faults) on the cracking the solder joint is concerned as a main issue.

5.1. Thermal Crack in the Solder Joint in LCR PV Module Interconnection

This section studies a comparison of the crack initiation and growth in the PV module solder joint interconnections due to the lamination process between the LCR and the CR interconnection. The XFEM in ABAQUS 2019 is employed to find the crack initiation temperatures and crack growth rate for different configurations of PV module interconnection designs. The mentioned parameters are considered as the main parameters to find the crack length in high temperatures and comparatively they help us to estimate the reliability of the PV modules. The crack initiation temperature and the crack growth rate associated in the solder joint of the LCR are found and then; they are compared to the relevant parameters of the CR interconnection in chapter 4 to find the impact of new structure on the failure of the PV module solder joint interconnections.

The LCR interconnection is one of the new concepts to replace the CR interconnection in solar cell tabbing. The LCR uses a grooved surface to reflect more light back onto the cell surface (see Figure 40).

Using the LCR interconnection increases the efficiency of PV modules by reflecting the incident sun rays from the interconnection ribbon to the cell surface.

The figure is redacted for the public view due to lack of permission of the copyright holder.

Figure 40: Schematic view of optical path and reflecting light back onto the cell for a structured Light–Capturing Ribbon (Ulbrich, 2013)

5.1.1. Finite Element Simulation

In this study, it is assumed that 3 and 5 LCR interconnections are used to connect the cell (see Table 2, Section 3.4, Chapter 3). For each configuration, the main dimensional parameters including ribbon interconnection width and thickness (i.e. copper thickness), solder thickness and silver-pad thickness are changed to find the effect of the dimensions on the specification of thermal crack (i.e. crack initiation temperature and crack growth rate) associated in the solder joint of the LCR.

2D symmetrical geometries of the LCR interconnections are modelled using a scripted Python code in ABAQUS 2019. To reduce the FEM calculation, the models are excluded the outer layers (glass protective sheet and Tedlar layers), and it is checked that there is not large difference between the results of the simulation with/without modelling the outer layers. Thus, the top edge of EVA which is in contact with the glass protective sheet in PV module is considered fixed displacement 0 in X and Y direction (i.e. no X and Y direction movement is assumed). Also, a symmetry boundary condition in thickness direction (Y axis) is applied to the silicon wafer. A view of FEM simulation of the LCR interconnection on the c-Si solar cell of the PV module is shown in Figure 41. This figure also demonstrates the material arrangement and the structural grooves of the LCR interconnection. The IMC layers which are more probable to be cracked due to their brittle material behaviour; are modelled as the boundary layers of the solder joint materials. Furthermore, the temperature of whole solar cell has been increased linearly and isothermally to the simulate the lamination process. The details of FEM simulation including the material properties, applied thermal load, are presented in Section 3.5.1 and Section 3.5.2.1 of Chapter 3, respectively. Figure 41 shows a schematic view of the FEM model for the LCR PV module interconnection.

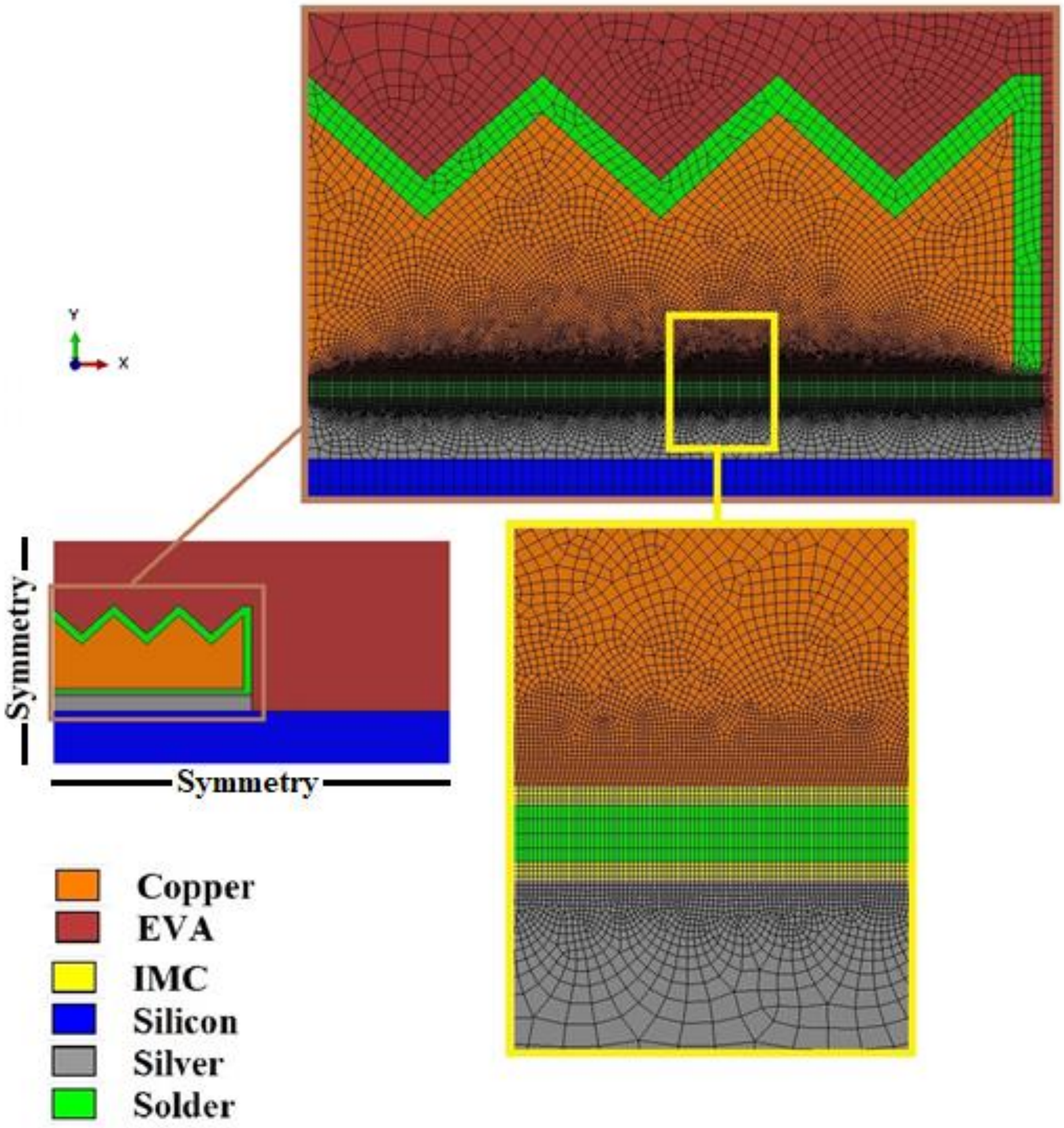

Figure 41**:** FEM view of the LCR interconnection in the PV module with symmetry constraints

5.1.2. FEM Results and Discussion

Various solder, copper and silver-pad thicknesses are considered to find the effect of geometrical parameters of the LCR interconnection on the crack initiation temperature and the crack growth rate; and the results are compared to the results of the relevant CR interconnection presented in Section 4.3, Chapter 4. The results of XFEM investigation of the LCR interconnections showed that the location of crack initiation and the propagation direction are same as the CR interconnections; which the crack is initiated at the edge of IMC layer interface with the copper ribbon and it is propagated in the shear direction due to low strength of the IMC layer.

5.1.2.1. Effect of Solder and Copper Thickness Change

Figure 42 shows the results of the XFEM for the crack initiation temperature in the LCR interconnection with the CR interconnection for different solder and copper thicknesses when the silver-pad thickness is considered as 50µm. The results indicate that for all copper thicknesses, there are similar trends of the crack initiation temperature changes via solder thickness changes. Figure 42 depicts that for the LCR interconnection, with increasing the silver-pad thickness from 10µm to 20µm, the crack initiation temperature increases and this offers more reliability since the crack is nucleated in higher temperatures (the silver-pad thickness is considered 50µm). However, after experiencing a peak of the crack initiation temperature at 20µm solder thickness, there is a decreasing rate of crack initiation temperature for thicker solder joints. Also, Figure 42 illustrates that for the LCR and the CR interconnections, with increasing the copper thickness, there is a reduction in the crack initiation temperature; this means that the thicker ribbons cause earlier crack initiation in the solder joint materials. This effect of copper thickness is also found when the LCR interconnection is compared to the relevant CR interconnection which the LCR interconnections are cracked in lower temperatures rather than the CR interconnection due to using thicker copper layer.

Figure 43 shows the crack growth rate in the LCR and the CR interconnections for different copper and solder joint thickness. As it is seen in Figure 35, there is a same trend of crack growth rate changes via changing the solder thickness; as with increasing the thickness of the solder joint, the crack growth rate increases fast and causes longer cracks which adversely affect the strength of the joint connection and the reliability of the PV module interconnection. Figure 43 also demonstrates that the LCR interconnection has less crack growth rate rather than the CR interconnection and this improves the reliability of this structured design when it has low crack initiation temperature. The graph also suggests that in the LCR interconnection with high solder joint thickness, with decreasing the copper thickness, the crack growth rate decreases. However, when the solder thickness is less than 30µm, there is no pronounced difference in the crack growth rate values of the LCR interconnection.

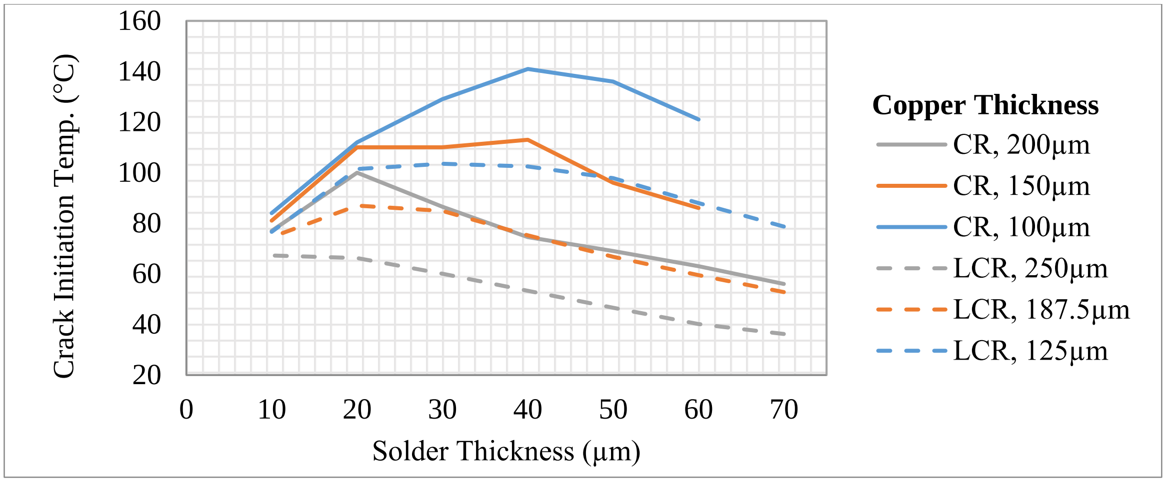

Figure 42**:** Comparison of the crack initiation temperature in the LCR with the CR interconnection for different solder and copper thicknesses.

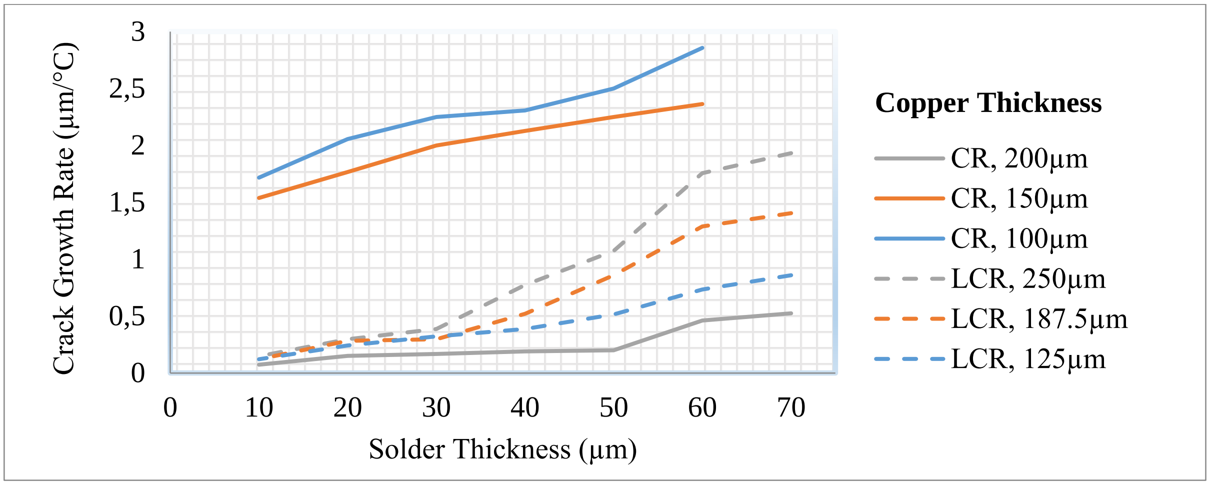

Figure 43**:** Comparison of the crack growth rate in the LCR with the CR for different solder and copper thicknesses.

5.1.2.2. Effect of Silver-pad and Copper Thickness Change

Figure 44 and Figure 45 show the crack initiation temperature and the crack growth rate in the LCR and the CR interconnections, respectively, for different silver-pad and copper thicknesses. The solder thickness in these cases is considered as 20μm that is found as an optimum thickness to have the highest crack initiation temperature and also low crack growth rate (see Section 5.1.3.1, Chapter 5).

Figure 44 shows that the peak of the crack initiation temperature for the LCR and the CR interconnections is when the silver-pad thickness is 40μm and 50μm, respectively (the solder thickness is considered 20μm). It is found that the pick of the crack initiation temperature in the LCR interconnection (106^{0}C) is same as the CR interconnection, but for thicker silver-pad pads than 40μm, the LCR interconnection experiences lower crack initiation temperatures. Figure 44 also states that using the thicker interconnection ribbon results in a reduction of the crack initiation temperature for both designs (see also Section 4.3.2, Chapter 4 for the results of the crack initiation temperature in the CR interconnections).

Figure 45 shows that the crack growth rate in the LCR interconnection with copper thicknesses of 125µm and 187.5µm have experienced lower values compared to the relevant CR interconnection (100µm and 150µm thick coppers). However, for the LCR interconnection with copper thickness 250µm, the crack growth rate is higher than the crack growth rate in the relevant CR interconnection (200µm thick copper). It is seen that when the silver-pad thickness increases, the crack growth rate decreases and this improves the reliability of the PV module interconnection. In addition, the graph suggests that for the silver-pads with thickness lower than 40µm, the thicker ribbons have lower crack growth rate.

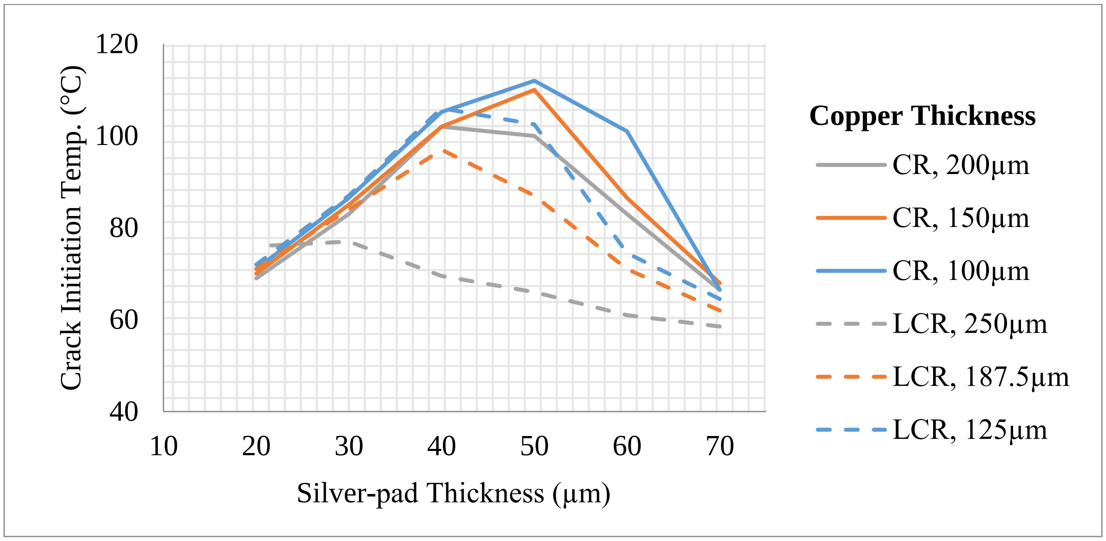

Figure 44**:** Comparison of the crack initiation temperature in the LCR with the CR interconnection for different silver-pad and copper thicknesses.

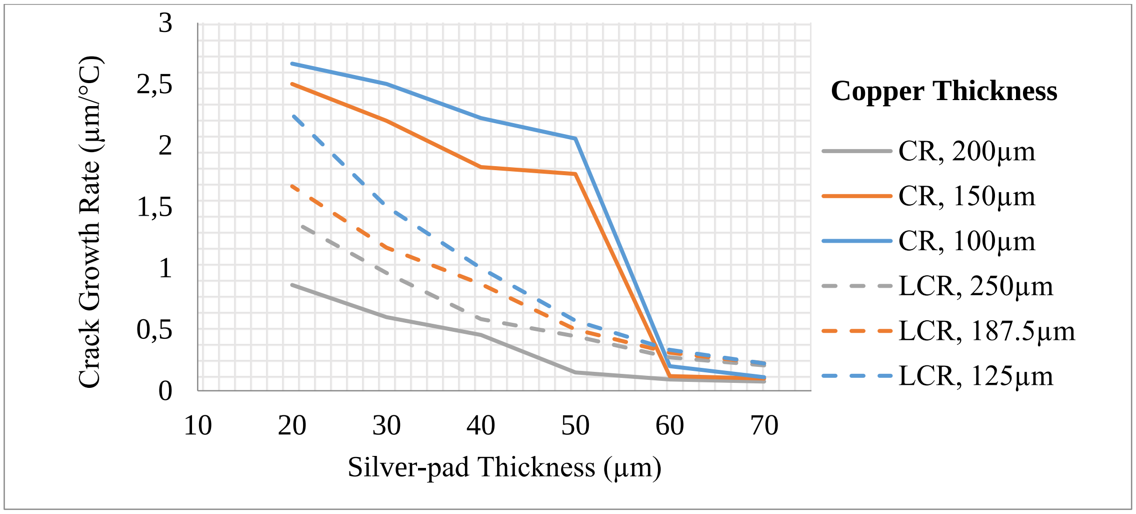

Figure 45**:** Comparison of the crack growth rate in the LCR with the CR interconnection for different silver-pad and copper thicknesses.

Figure 46 shows the calculated crack length in the LCR and the CR interconnections at high lamination process temperature (150˚C) for different copper and silver-pad thickness of the interconnection ribbons (with an optimum solder thickness which is 20µm). According to Figure 46, the crack length in the LCR interconnection with copper thicknesses of 125µm and 187.5µm are less than the crack length in the relevant CR interconnections and only for the 250µm thick LCR interconnection, length of crack is higher than the 200µm thick CR interconnection. Also, it is seen that for the silver-pad pad thicker than 40µm, length of crack in the LCR interconnection is independent on the copper thickness. Hence, the LCR interconnection with copper thicknesses of 125µm and 187.5µm (thin ribbons) can suggest more reliability for the PV module interconnection rather than the relevant CR interconnection.

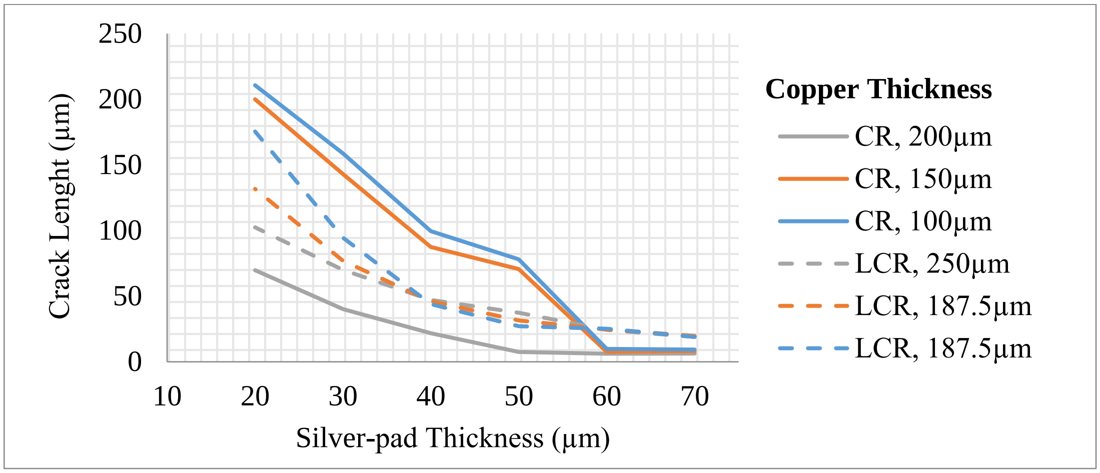

Figure 46: Crack length at 150^0C in the LCR and the CR interconnections for different silver-pad and copper thicknesses.

5.2. Crack in Non-Homogeneous Solder Coating in the MBB Interconnections

The MBB interconnection is a new type of interconnection which incorporates several round copper ribbons to help increase the energy conversion and transmission efficiency of PV modules and also to reduce the material costs. However, there is a main challenge in terms of the non-homogeneity of the solder coating on the ribbons (resulting from manufacturing process faults, see also Figure 15, chapter 2). The non-homogeneity of the solder coating on the ribbons is one of the main factors that is responsible for the poor connections between the ribbon and the silver-pads; which adversely impacts on the interconnection strength and long-term reliability (Walter, et al., 2014). The thermomechanical investigation of both cell and interconnecting ribbon of MBB PV modules by Rendler showed that that using MBB ribbons with lower diameters results in a reduction of the thermomechanical stress in a solar cell (Rendler, et al., 2016); and also the maximum stress in the solder joints occurs at the edge of the outermost contact pads of the solar cell (L.C. Rendler, et al., 2018). However, it is obvious that the lower diameters of the MBB ribbons associate more manufacturing errors in the solder coating on the ribbons. Thus, it is very important to understand how the stress distribution and level can be affected by changing the non-homogeneity of the solder coating on the ribbons.

The focus of this section is on the effect of non-homogenous coatings on the strength of brittle micro-cracking in the IMC interface layer of the PV module solder joint interconnections. This section evaluates the two main parameters of non-homogeneity (out of centre value and direction), and also investigates the effect of geometrical parameters. The XFEM in ABAQUS 2019 was used to determine the micro-crack initiation temperature and location for a given joint design. Altogether, 82 ribbon interconnection models were simulated in ABAQUS 2019.

5.2.1. Geometry of Models

Figure 47 shows cross-section of a soldered MBB interconnection on the silver-pad. As shows, the solder materials are melted and moved to the corners of the connection area between ribbon and the silver-pad. This distribution of the solidified solder material in the connection area is used to find the mathematical formulation for determination of the solder joint geometry (Walter et al., 2014).

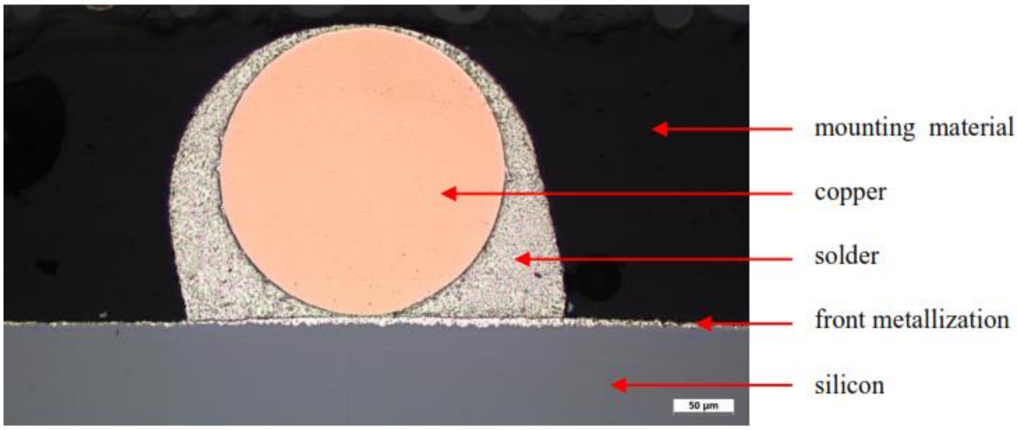

Figure 47: Cross-section of a soldered MBB interconnection on the silver-pad (Walter et al., 2014).

The schematic view of cross-section of the round ribbon interconnector presented in Figure 48, shows that $\mathbf{S_e}$ (the molten solder area) located between the lower end of ribbon interconnection and the silver-pad is displaced sideways to the both left and right corners of interconnect ribbon; thereby increasing the contact area between the ribbon interconnection and silver-pad. The mathematical expressions used for calculating X_m, the extra contact length between the solder joint and the silver-pad, is given by Equation #11. If we assume that the Solder Area S_e with height, H_e is sub-divided into triangular areas S_m; then the derivation of the extra contact length X_m is as detailed in equations #11 to #15.

To investigate the effect of solder joint height on the strength of the ribbon interconnection, four different molten solder heights H_e was considered (i.e. H_e was varied from 25%, 37.5%, 50% to 62.5% of solder thickness).

$$X_e = \sqrt{{R_s}^2 - (R_s - H_e)^2} \tag*{$Eq.11$}$$

$$tan(\alpha) = \frac{X_e}{R_s - H_e} = \frac{Y_m}{X_m} \tag*{$Eq.12$}$$

$$S_e = {R_s}^2.\alpha - 2.X_e.(R_s - H_e) \tag*{$Eq.13$}$$

$$S_m = \frac{Y_m.X_m}{2} = \frac{S_e}{2} \tag*{$Eq.14$}$$

$$X_m = \sqrt{\frac{S_e}{\tan(\alpha)}} = \sqrt{\frac{{R_s}^2.Arctan\left(\frac{\sqrt{{R_s}^2 - (R_s - H_e)^2}}{R_s - H_e}\right) - \sqrt{{R_s}^2 - (R_s - H_e)^2}.(R_s - H_e)}{\frac{\sqrt{{R_s}^2 - (R_s - H_e)^2}}{R_s - H_e}}} \tag*{$Eq.15$}$$

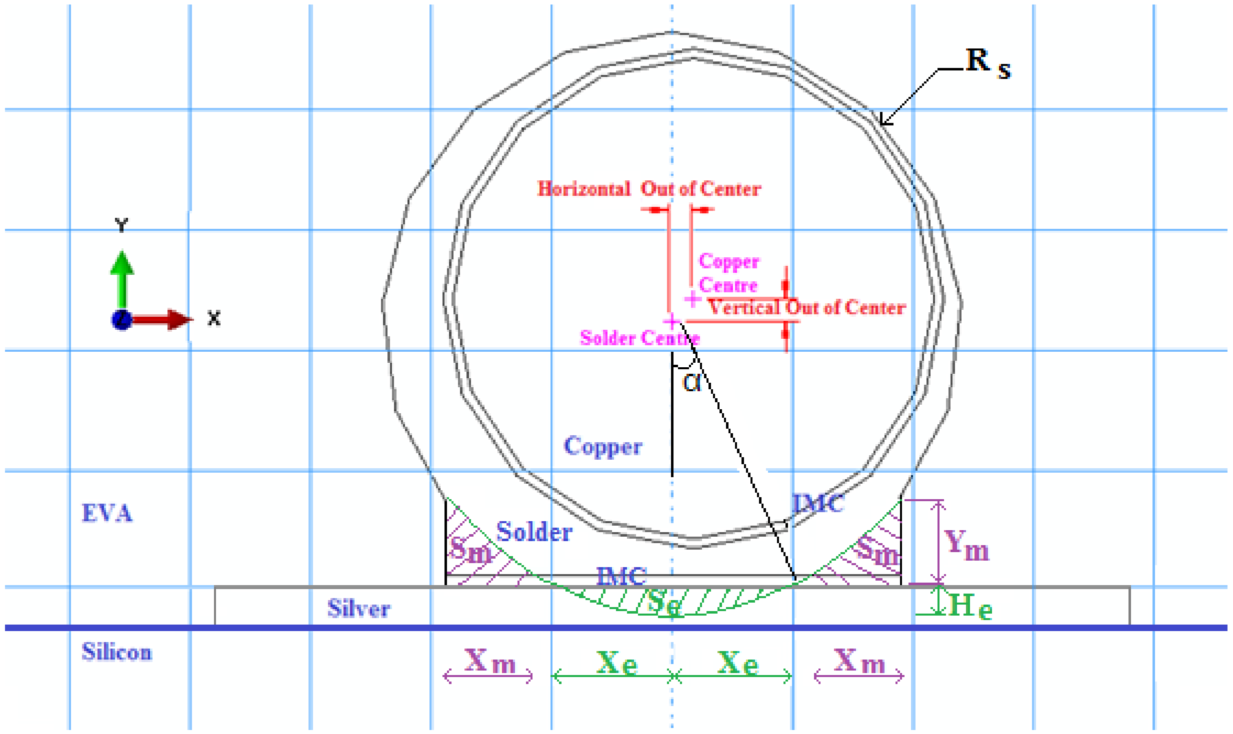

Figure 48: Cross-section of round ribbon interconnector with view of vertical and horizontal out of centre.

5.2.2. FEM Simulation

Based on multi-busbar connector prototype specifications published by (Walter et al., 2014), the diameter of copper ribbons (15 ribbons) and the width of silver-pad are assumed to be 276µm and 450µm, respectively; and the thickness of silver-pad are 20µm (Note: in order to achieve stable response, the gaps between the interconnection ribbons were considered to be 6mm). To investigate effect of geometrical parameters, four different solder thickness (15µm, 20µm, 25µm and 30µm) were evaluated. In addition, the effect of IMC layer thickness (silver-pad interface) was investigated; with four different IMC layer thickness considered (1µm, 2µm, 3µm and 4µm was used to reflect wide range of soldering temperature). However, the IMC layer thickness on the copper ribbon core interface is assumed to be 2µm and symmetry boundary conditions are applied for the bottom of silicon cell.

For reducing the FEM calculation, the 2D models excluding the glass protective and Tedlar layers are simulated using the scripted code in ABAQUS 2019. The top edge of EVA in contact with the glass protective sheet is considered fixed in X and Y; and a symmetry boundary condition in thickness direction (Y axis) is applied to the mid thickness of the silicon wafer. The temperature of whole solar cell has been increased linearly and isothermally to the crack initiation temperature. For simulation of the high temperature lamination process, an isothermal increasing temperature load is applied to the whole PV module interconnection models (see Section 3.5.2 of Chapter). The temperature dependent material properties of PV module interconnecting materials are considered in which the cohesive traction-separation law method is used for simulation of the XFEM technique in metallic materials of the PV module interconnection (see Section 3.5.1 of Chapter).

Figure 49, shows the discretization and meshing method used in the study and the configuration for the copper core, solder joint, IMC layer, silver-pad, EVA and silicon cell. A very fine mesh size of 1µm was used for investigating the effect of the IMC layer thickness on the silver-pad interface; and to determine the crack initiation temperature and location of micro-crack.

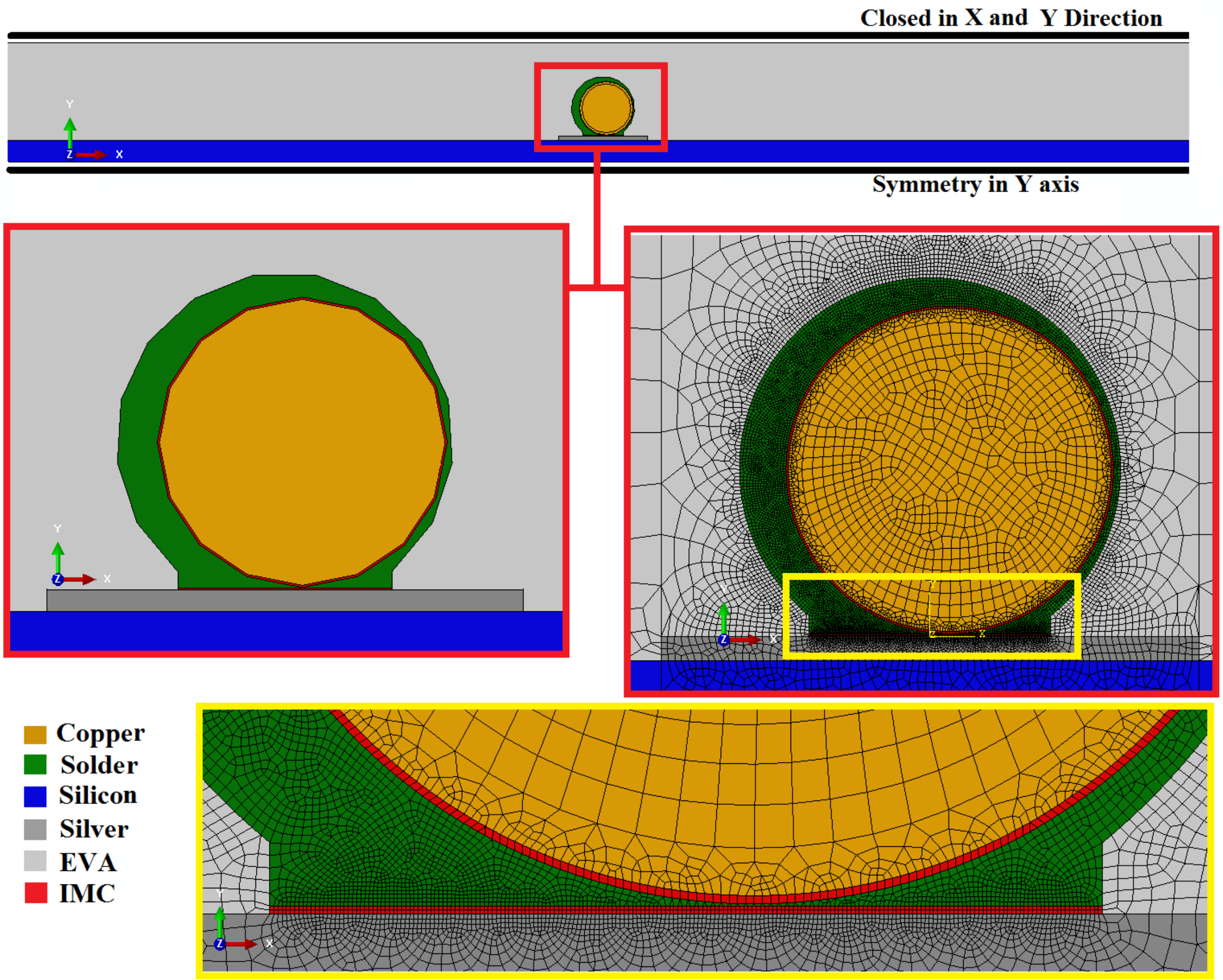

Figure 49: Applied mesh and material arrangement of the PV module Cell in the top interconnecting area.

5.2.3. Results and Discussions

This section presents the results from the study on the investigation of the effect of solder coating non-homogeneity on the thermomechanical response of round copper ribbons used for PV module interconnections and the evaluation of the effect of three geometrical parameters, namely the IMC layer thickness, solder joint height and thickness on the strength of the interconnections.

5.2.3.1. Crack Location

The results of the XFEM analysis presented in Figure 50 shows the one-micrometre crack that is initiated in the IMC layer between the solder joint material and silver-pads. For all the geometrical parameters considered in the study, the results show that the highest stress concentration (and the micro-crack initiation) occurs at the edge of the IMC layer interface between the solder joint and silver-pad. The results also show that the crack propagation is in the parallel direction to the silver-pad. Figure 50 depicts the shear stress contours in the IMC layer between solder coat and silver-pad at the micro-crack initiation temperature and the crack propagation. Although the concentration of shear stress in the IMC layer leads to the micro-crack initiation and propagation along the IMC interface layer; further crack progression can be caused by thermal cycling during operation which can lead to the disconnection of the ribbon interconnection from the silver-pad.

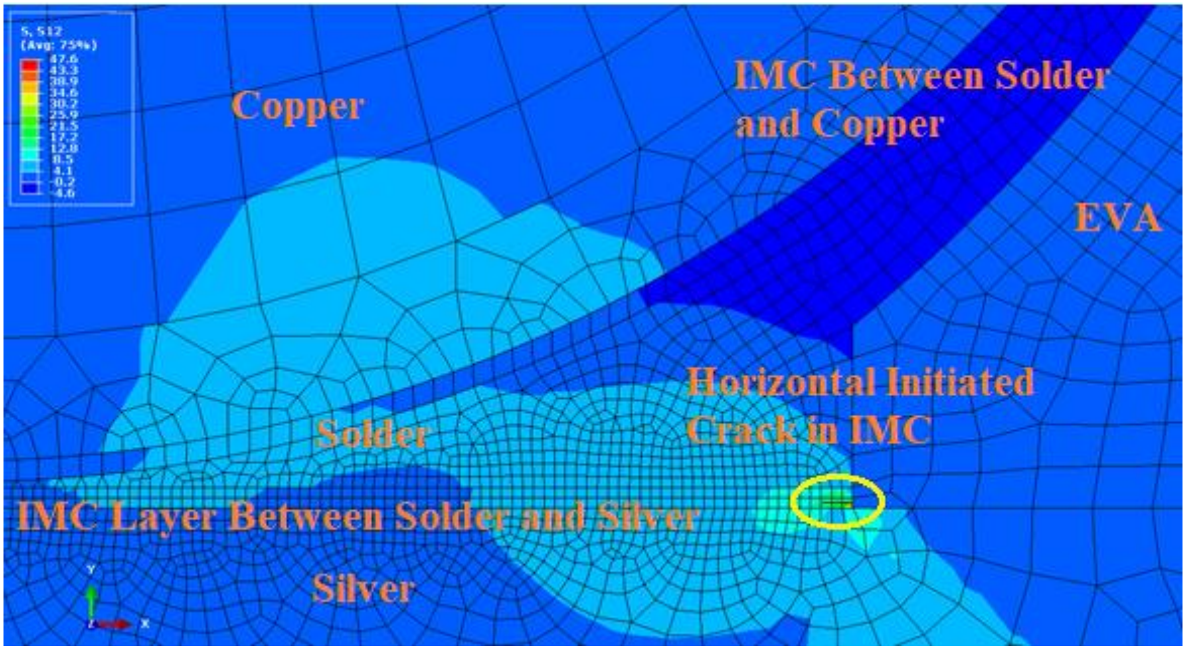

Figure 50: Shear Stress (MPa) distribution at the temperature of cracking (105 °C)in the IMC layer between solder coat and silver-pads.

5.2.3.2. Out of Centre Positioning of Copper in the MBB Interconnection

Figure 51 shows the crack initiation temperatures for different geometries and out of centre distances in different directions including the upward Y direction (+90 Degrees), the downward Y direction (-90 Degrees), the horizontal (0 Degree) and also the upward and the downward radial directions (-9.5 and +/-18.5 Degrees). The molten solder height in this graph is considered 50% of solder thickness (10µm) and the thickness of IMC layers are assumed to be 2µm. The results of the simulations show that by increasing the out of centre distance (i.e. with more non-homogenous solder coating) in downward directions, the crack initiation strength of the solder joint decreases (Note: the highest rate is for -90 Degree out of centre positioning). This means that for the downward out of centre positioning of the copper inside the coated ribbon, the crack initiation temperature decreases with increasing non-homogeneity of coating. This is because the narrow solder thickness between copper ribbon and silicon layer results in an increase in the accumulated strain and thermal stress due to the high CTE mismatch between the interconnecting materials.

For this reason, the micro-cracks are more likely to occur at the interface between the IMC layer and the silver-pad. The results also show that for the upward out of centre positioning of the copper inside the coated ribbon, the cracking initiation strength of the solder joint is increases with more non-homogenous solder coating (increases the micro-crack initiation strength); and the crack initiation temperature is also much higher than those for downward out of centre positioning directions.

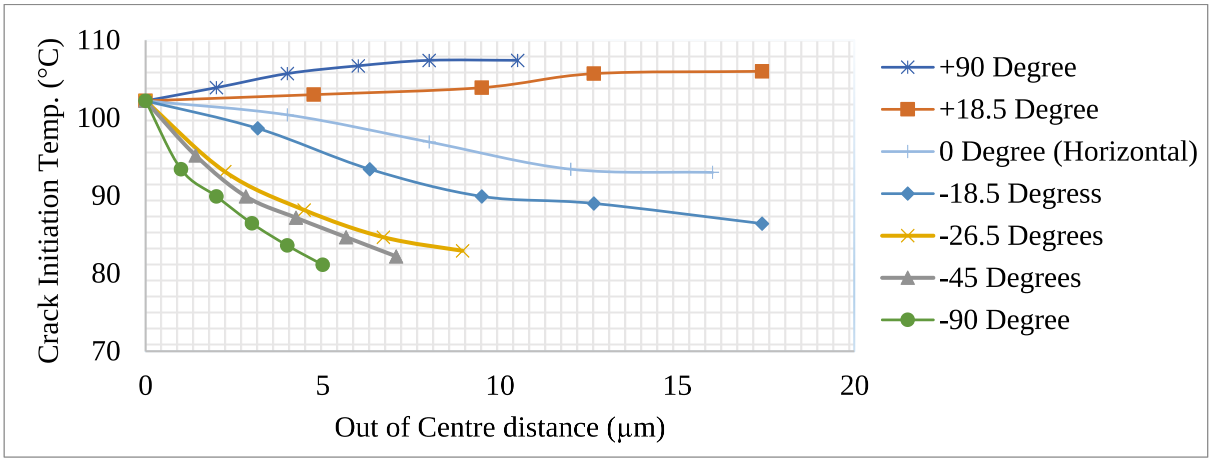

Figure 51: Crack initiation temperature for different direction of out of centre distances.

5.2.3.3. Molten Solder Height

Figure 52 shows the effect of the out of centre distance in the downward Y direction (-90 Degrees) for different molten solder heights on the crack initiation temperature. In principle, increasing the molten solder height increases the solder contact between the copper ribbon and the silver-pad and hence lead to more reliable connection; the results in Figure 52 suggests that by increasing the molten solder height and increasing solder contact will actually result in micro-cracks occurring at much lower temperatures. This reduction in the micro-crack initiation temperature can be attributed to the high levels of thermal stress resulting from the CTE mismatch in the increased solder contact. However, the reduction in the micro-crack initiation temperature due out of centring is mitigated by the increase in solder joint strength; and thereby reducing the impact of out of centring with high molten solder height.

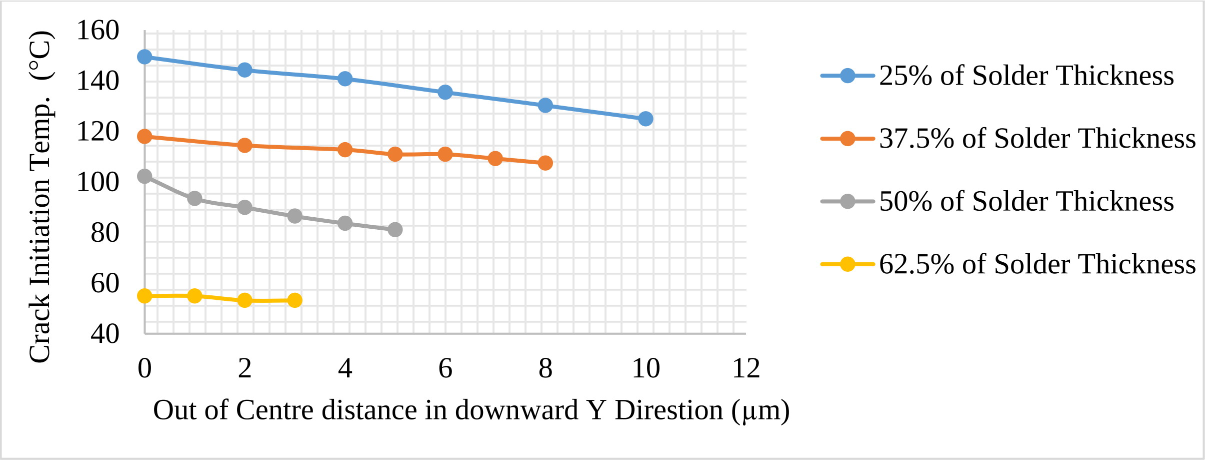

Figure 52: Crack initiation temperature via out of centre distances in downward Y direction for different molten solder height.

5.2.3.4. Thickness of IMC Interface Layer between Ribbon Interconnection and Silver-Pad

Figure 53 demonstrates the effect of out of centre distances in downward Y direction (-90 Degrees) on crack initiation temperature for cases where the solder thickness is 20µm and the molten solder height is 10µm (i.e. 50% of solder thickness), with different IMC layer thickness between ribbon interconnection and silver-pad. The results show that solder joints with lower IMC layer thickness exhibited higher strengths than solder joints with higher IMC thickness. The results also show that there is a reduction in the crack initiation temperature with increases in the out of centre positioning; however, this is negligible with higher IMC layer thickness.

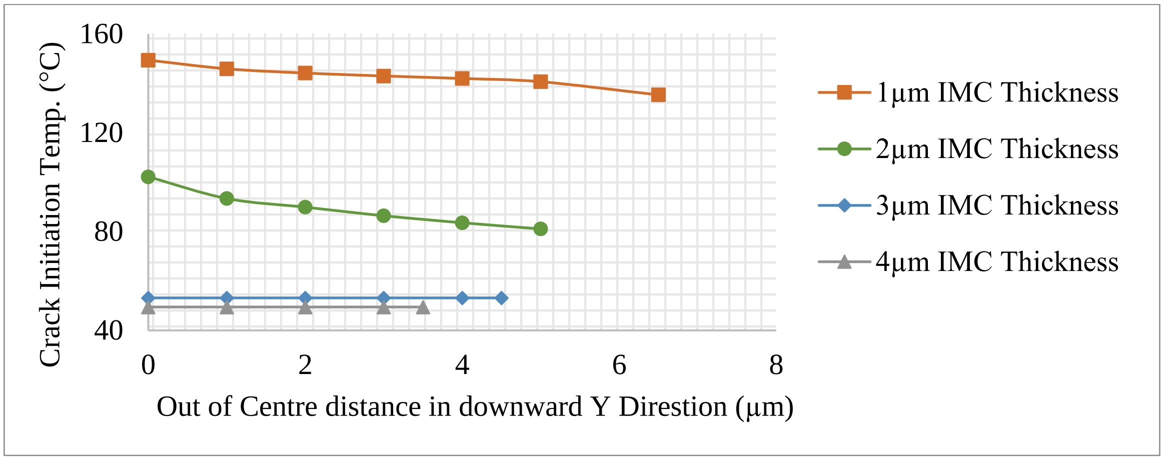

Figure 53: Crack initiation temperature via out of centre distances in downward Y direction for different IMC layer thickness.

5.2.3.5. Solder Coating Thickness

Figure 54 shows the effect of out of centre distances on crack initiation temperature in downward Y direction (-90 Degrees) for cases with 10µm molten solder height (50% of Solder thickness), IMC layer thickness of 2µm with different solder thickness. The result shows that for higher solder thickness, increasing the solder thickness reduces the crack initiation temperature; but the effect of out of centre distance on crack initiation temperature is negligible.

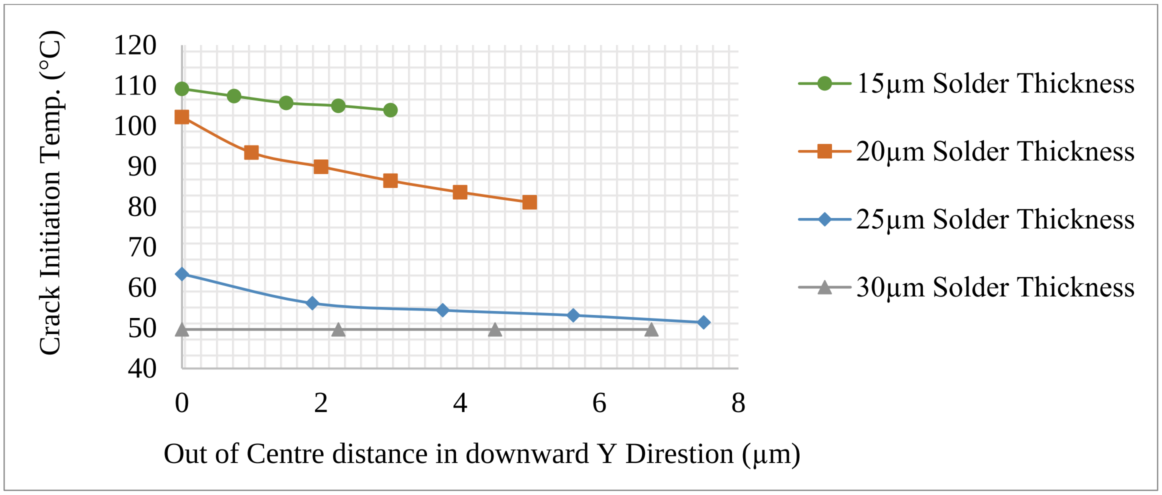

Figure 54: Crack initiation temperature via out of centre distances in downward Y direction for different solder thickness.

5.3. Chapter Summary and Conclusion

This chapter studied the crack initiation temperature and the crack growth rate in the LCR interconnection and the MBB interconnection of the PV module due to the lamination process. Firstly, the results from the XFEM simulation in ABAQUS 2019 are found for the LCR interconnections and they are compared to the relevant results for the CR interconnections. The thicknesses of the LCR interconnection are considered as 125µm,187.5µm and 250µm to have the same cross-section of the CR interconnection with the thicknesses of 100µm,150µm and 200µm, respectively. Secondly, this chapter presented the results of the XFEM Simulation performed on the round ribbon used in MBB interconnection of PV module to evaluate micro-crack initiation in non-homogenous solder coating at high temperatures. The determination of the conditions for micro-crack initiation in the solder coating on the round ribbon is important for determining the interconnection design parameters that will ensure long-term reliability of the solar PV module. The main conclusions for the results are presented in the sub-sections below:

5.3.1. Conclusion for Crack Analysis in the LCR Solder Joint Interconnection

Different configurations including silver-pad, copper and solder thickness are considered to study the effect of each parameter on the crack initiation temperature and the crack growth rate. The results show that there is a same trend of the crack initiation temperature and the crack growth rate for the CR and the LCR interconnections; also the location of the cracks is at the edge of the IMC layers and the cracks propagates in shear direction. Compared to the CR interconnection, the LCR interconnections are cracked in the lower temperatures, but they experienced lower values of the crack growth rate. We found that the LCR interconnection experiences a peak of crack initiation temperature when the solder and the silver-pad thicknesses are 20μm and 40μm, respectively, as for thicker silver-pads, there is a fast reduction of the crack initiation temperature. The results show that thicker copper ribbons cause earlier crack initiation in the solder joint materials. It is also shown that for solder joints thicker than 20μm, the crack growth rate increases fast and makes longer crack which adversely affect the strength of the joint connection and the reliability of the PV module interconnection. However, with increasing the silver-pad thickness, there is a high reduction in the crack growth rate values. The optimum solder, silver-pad and copper thickness for the LCR interconnection are recognized as 20μm, 40μm and 125-187.5μm, respectively, where this configuration experiences high crack initiation temperature and low crack growth rate and then crack length in the solder joint material is shorter than the crack length in the relevant CR interconnection.

5.3.2. Conclusion for Crack Analysis in the MBB Solder Joint Interconnection

The study evaluates the two main parameters of non-homogeneity (out of centre value and direction), and also investigates the effect of geometrical parameters including IMC layers thickness and solder joint height. The XFEM in ABAQUS 2019 was used to determine the high temperature required for micro-crack initiation for each joint design. Also, the XFEM analysis was used to predict the location of the micro-crack in the IMC layer between solder and silver-pad. The results show that the micro-crack is initiated in the parallel direction with silver-pad and the initiation temperature is most affected by the direction of solder coating non-homogeneity and the downward vertical direction of out of centre positioning of copper in the solder coating leads to the most reduction in crack initiation temperature (up to 21% reduction was observed for the case 5.5μm out of centre distance). The results also show that by increasing the amount of molten solder/solder thickness, the micro-crack initiation will take place at a lower temperature due to high thermal stress concentration in the IMC layer. Also, it was found that at high solder thickness the micro-crack initiation temperature is less affected by non-homogeneity. The results also show that increasing the IMC layer thickness leads to a decrease in the micro-crack initiation temperature threshold and thinner IMC layers are more sensitive with non-homogeneity.

Chapter 6

6. Creep-Fatigue Life Estimation for PV Module Interconnections

6.1. Introduction

Study of the potential failure modes of PV module have shown that one of the major PV modules reliability challenges is the creep-fatigue failure of the solder joints used for connecting the ribbon to the cell. This is because the daily power-up and shut-down and the associated heating and cooling down of the PV module results in thermal cycling and ageing of the PV module. Consequently, the solder joints used for the PV module interconnection can experience very high stress and strain levels due to the CTE mismatch between the adjacent materials (Itoh, et al., 2014). The induced stress and strain in the solder joints results in high levels of energy accumulation that can significantly reduce the creep-fatigue life of the interconnection and the long-term reliability of the PV module (Ogbomo, et al., 2018).

The research on numerical approaches for predicting creep-fatigue life of solder joints mostly suggests that the modified Coffin-Manson model and the developed Morrow Energy Density model (based on total strain energy) accurately work to calculate the number of heat cycles to failure (N_f). Also, it is reported that the Hyperbolic Sine creep law is widely used to determine the energy terms of the aforementioned models in order to estimate the creep-fatigue life of solder materials (see Section 2.8, Chapter 2).

In this chapter, the FEM simulations of the different PV module interconnections operating under thermal cycling loads are implemented to find the creep-fatigue failure of the solder joints used for connecting the ribbon to the cell. For this, the Hyperbolic Sine creep law is used to find the required energy terms for the calculation of the creep-fatigue life; and then the modified Coffin-Manson and the developed Morrow Energy Density models are considered to calculate the creep-fatigue life of the solder joints in both the conventional and new PV module interconnections. The details of the numerical approach for the creep-fatigue analysis used in this study, are presented in Section 3.2.2, Chapter 2.

6.2. Creep in the Conventional PV Module Solder Joint Interconnection

This section is to investigate the creep-fatigue failure of the conventional PV module solder joint interconnections operating under thermal cycling load in service condition. The total dissipated energy in the solder joint is extracted from FEM simulation in ABAQUS 2019 using the Hyperbolic Sine creep law, and then the values of the energy terms are used to calculate the number of thermal cycles to failure (N_f) using the developed Morrow Energy Density model. Also, a Coffin–Manson–Arrhenius exponent factor is found from comparing different thermal cycling conditions. Then this factor is used to determine the creep-fatigue life of the PV module solder joint interconnections under arbitrary thermal cycling condition.

6.2.1. FEM Simulation for Creep-Fatigue Life

To investigate the creep-fatigue behaviour of solder joint in the CR interconnections, 2D models using 3- and 4-node plane strain elements are implemented (see Section 3.5.5, Chapter 3). Different configurations of the CR interconnections are examined, including the designs with 2, 3, and 5 ribbons (see Table 2, Section 3.4, Chapter 3). As it is mentioned in Section 3.3 of Chapter 3, the thickness materials used for the models (namely, aluminium, silicon cell, EVA, glass and Tedlar layers), are assumed to be 25µm, 200µm, 460µm, 3mm and 190µm, respectively. Also, the thickness of the IMC layer in the boundaries of the solder joint with the copper and silver-pad materials is considered to be 4µm. The interconnection width and the thickness of other component parts including silver-pad, copper, and the solder joints are then varied to investigate the effect of interconnection design on the creep-fatigue response. The mid-section of the models is subjected to the symmetry boundary condition and bottom-end of the model (Tedlar layer) is fixed in Y axis degree of freedom (see Section 3.5.4, Chapter 3). The models are subjected to a homogenous thermal cycling load, with time history in accordance with the IEC 61215-2:2016 standard (see Section 3.5.1.2, Chapter 3). To define the stress/strain hysteresis loop which is used for calculating the accumulated creep energy, the Hyperbolic-Sine creep model (with the temperature dependent material properties) is used for the solder joints (see Section 3.5.1.2, Chapter 3). Other material properties of the PV module interconnecting materials used in these simulations are presented in Section 3.5.1, Chapter 3.

Figure 55 shows a schematic view of the cross-section of the conventional PV module interconnection showing the applied boundary conditions and the solder joint mesh design used for the 2D simulation in ABAQUS 2019.

Furthermore, to compare the results from 2D simulation with the results from 3D simulation for a similar case study, a 3D model of conventional PV module interconnection with 20µm, 40µm, 200µm and 1000µm silver-pad thickness, solder joint thickness, copper ribbon thickness and ribbon width, respectively, is performed in ABAQUS 2019. However, for the 3D simulation some simplifications are considered to reduce the FE calculations and they are checked to have negligible influence in the results. This modelling simplifications include using symmetry boundary condition for the silicon mid-section and using a fixed boundary condition in contact of the EVA layer with the glass layer instead of modelling the glass. Also, relatively coarse meshes (with minimum size of 4µm for IMC layer) are used for the used 3D nonlinear elements (C3D20, 20-node elements). All other simulation details such as material property and load conditions are considered same to the 2D simulation as it was discussed before. Figure 56 shows a schematic view of the 3D model simulated in ABAQUS 2019.

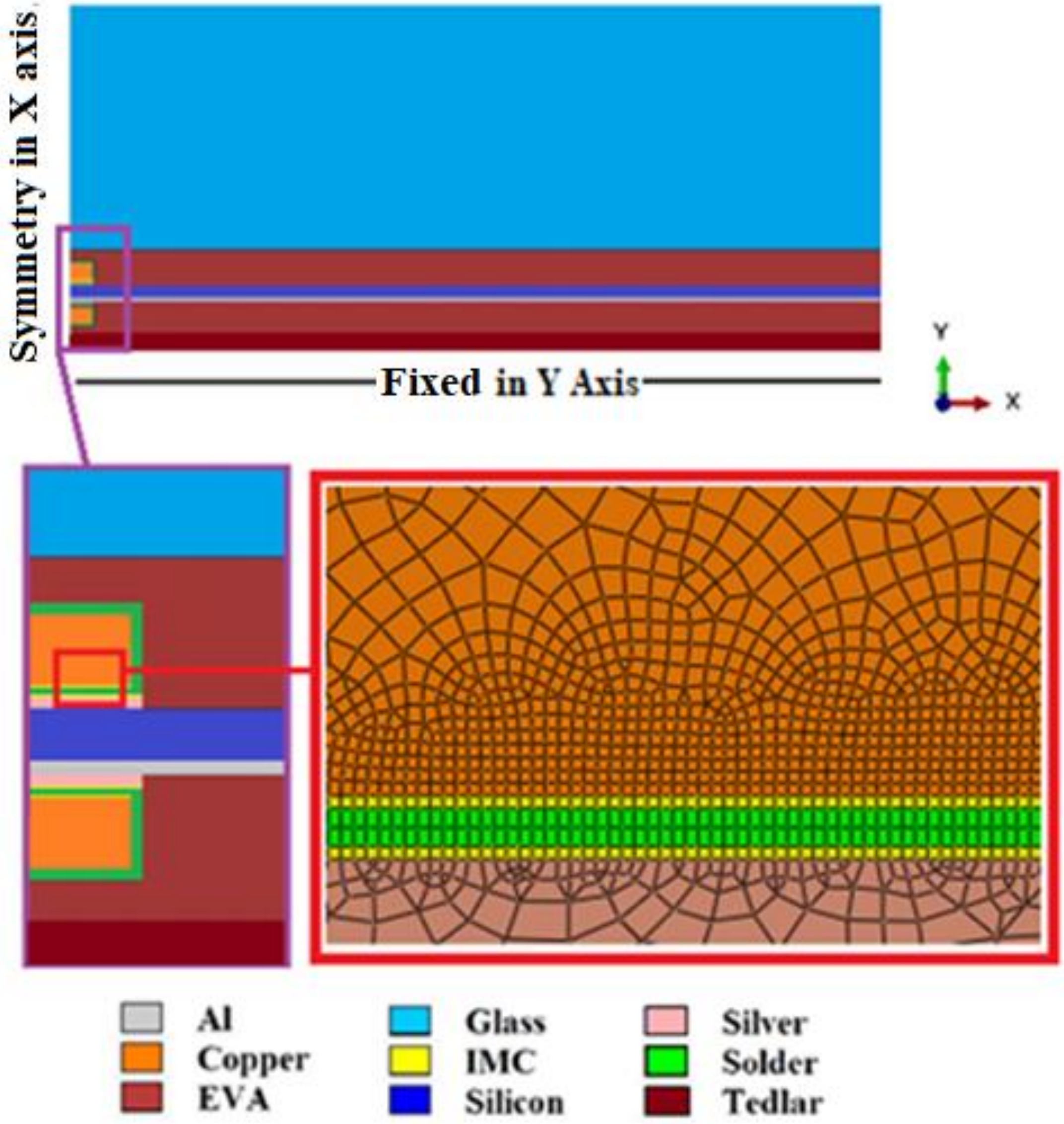

Figure 55: Schematic view of the 2D simulated conventional PV module interconnection showing the boundary conditions, arrangement of materials and solder joint mesh design.

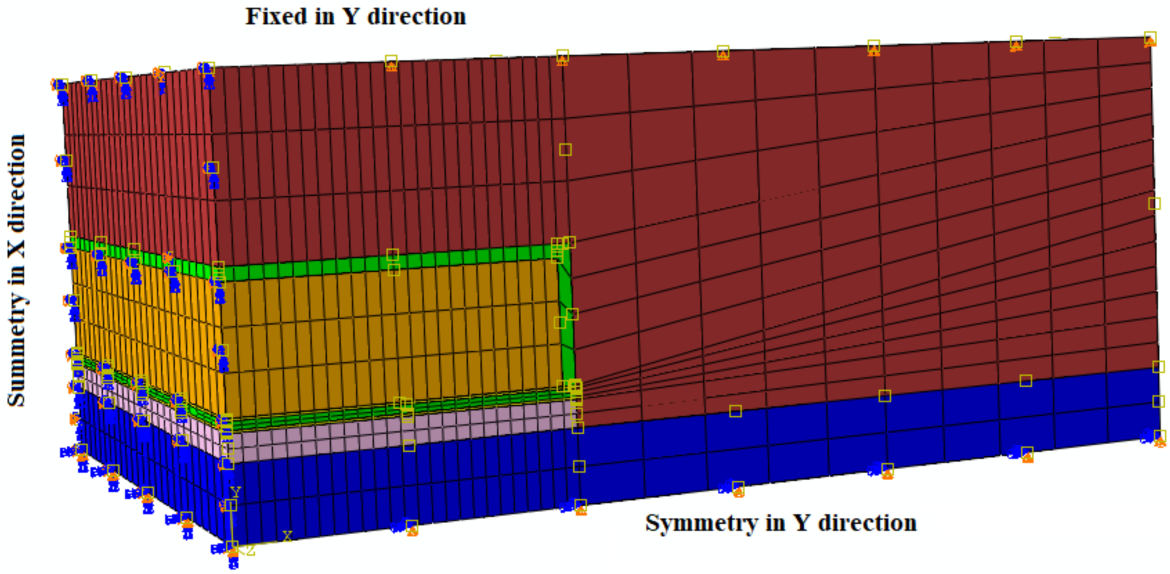

Figure 56: Schematic view of the 3D simulated conventional PV module interconnection.

6.2.2. Results and Discussion

The FEM results of the creep stress/strain for each PV module interconnection configuration investigated in this study for 5 thermal cycles are discussed in this section. Figure 57 shows the creep strain distribution (in shear direction), in the solder joint of the conventional PV module interconnection simulated in 2D and 3D simulations, for the first 5 thermal cycles (ranging from -40°C to 85°C). The interconnection model is simulated with 20µm, 40µm, 200µm and 1000µm in solder, silver-pad, copper thickness and ribbon width, respectively. Figure 57 shows that the results from the 2D simulation is in convincing agreement with the results from the 3D simulation (<15% difference). In addition, the results from both 2D and 3D simulation show that the maximum shear creep strain in the solder joint is located at the side of the IMC layer in contact with the copper; and that the middle of the solder joint does not experience high levels of shear creep strain. The location for the maximum shear creep strain found in the solder joint is in agreement with the location of the maximum shear stress (location of the crack initiation) found in chapter 4.

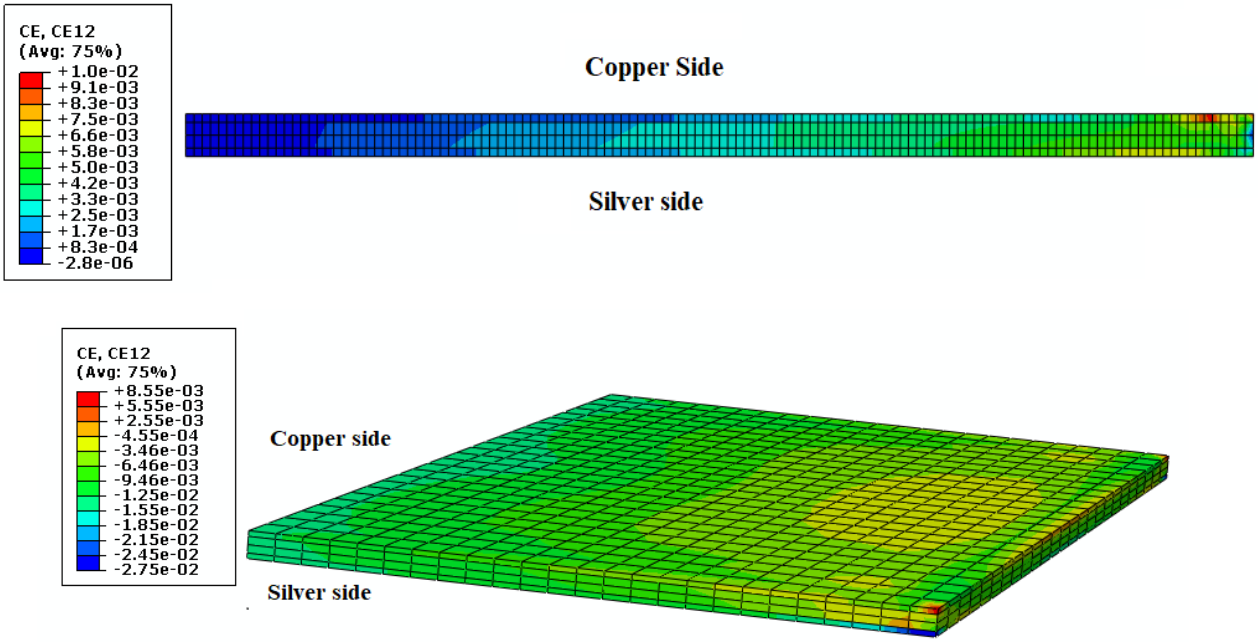

Figure 57: Creep strain distribution (in shear direction) in the conventional PV module interconnection after 5 thermal cycles, top: from the 2D simulation, bottom: from the 3D simulation.

Figure 58 shows the plot of the hysteresis stress-strain in shear direction at the element with the highest level of the creep strain for the solder joint during the first 5 thermal cycles shown in Figure 57 (from 2D simulation). Figure 58 shows that the area enclosed by the stress-strain curve increases marginally with increase in the number of cycles; and this means that the accumulated creep energy in the solder joint material increases with thermal cycling which may induce thermal fatigue failure of the solder joint. Also, the maximum shear strain induced during the thermal cycles is more than 1% (the limit value of the strain level) which is acceptable to use Coffin-Manson model for accurate estimation of the creep-fatigue life (Hund & Burchett, 1991).

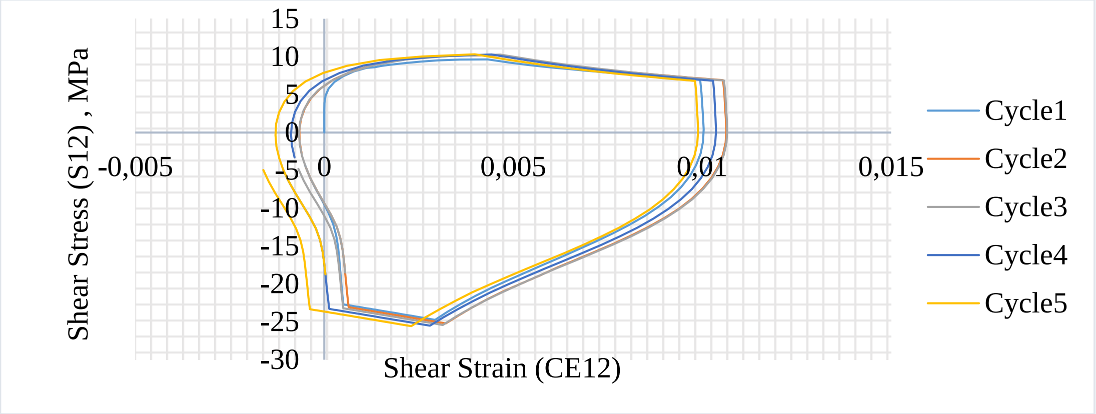

Figure 58: Plot of the Hysteresis Stress-Strain (in shear direction) in the solder element with the highest creep strain value (in the CR interconnection) for 5 thermal cycles.

Figure 59 shows the distribution of the creep-dissipated energy per unit volume for the solder joint shown in Figure 57 (from the 2D simulation), for 5 thermal cycles (ranging from -40°C to 85°C). The changes in the creep-dissipated energy at the element with the maximum values during the 5 thermal cycles is shown in Figure 60. As it is shown in Figure 59, the side of solder joint exhibits a maximum creep energy and it increases with an increase of the cycle number. This trend is clearly shown in Figure 60, which by increasing the time (cycle number), the magnitude of the maximum creep dissipated energy increases.

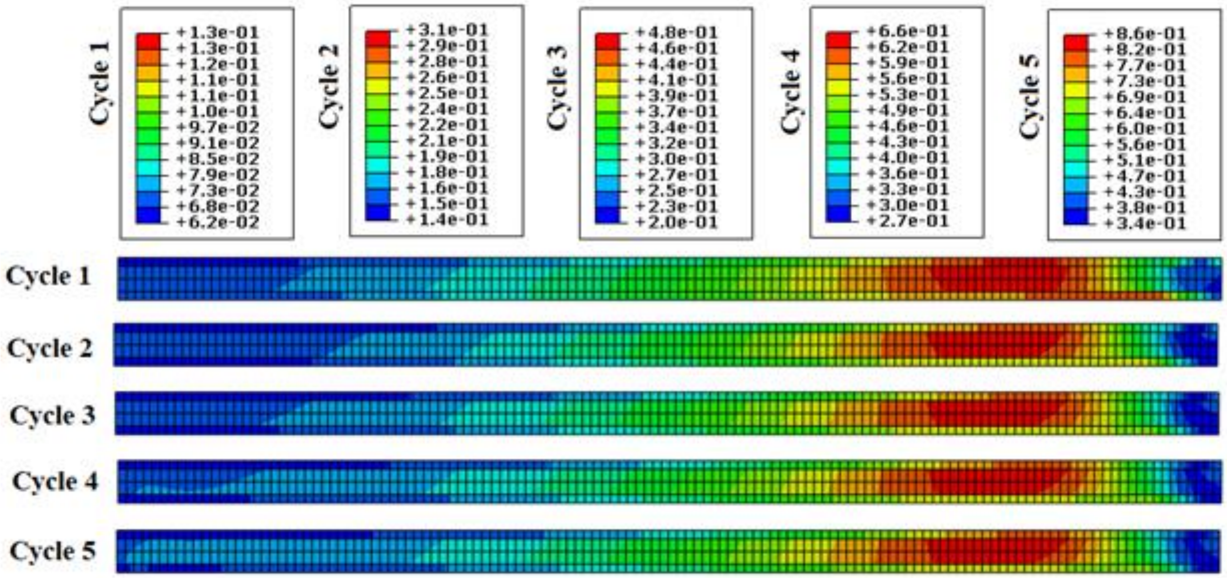

Figure 59: Total creep dissipated energy density (per unit volume, unit: mJ/mm^3) in the solder joints for the 5 thermal cycles.

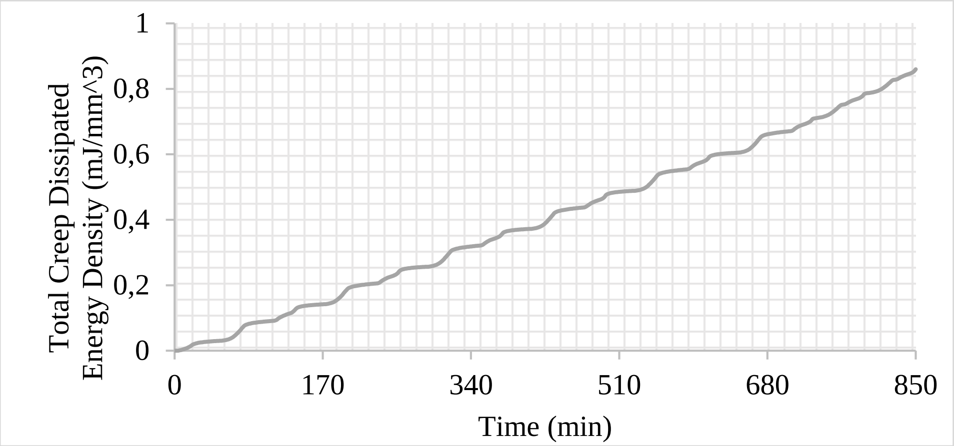

Figure 60: Total creep dissipated energy density (per unit volume) at the element with the highest creep strain value in the solder joint for 5 thermal cycles (from 2D simulation).

6.2.3. Estimation of the Number of Cycles to Creep-Fatigue Failure

To determine the number of thermal cycles to creep-fatigue failure (N_f) of the PV module solder joint interconnections, a developed Morrow Energy Density model is used. This model is based on the total strain energy (plastic and elastic) and it uses the stress–strain hysteresis energy loops for predicting the creep energy in each cycle. For each configuration of the PV module interconnection, the accumulated creep energy density per cycle (w_{acc}) is found by using the Hyperbolic Sine creep law for the solder joints. Then, the value of N_f for the solder joints under standard thermal cycling condition (temperature ranging from -40°C to 85°C, according to the IEC 61215-2:2016) are calculated using the average value of w_{acc} in the solder joints between the interconnecting materials as presented in Equation #8 (see Section 3.2.2, Chapter 3).

Figure 61, Figure 62, Figure 63 and Figure 64 show the effect of different parameters (namely: solder thickness, silver-pad thickness, copper thickness and ribbon width; introduced in

Table 11) on the value of N_f for the CR interconnections. Figure 61 shows that for solder joints thicker than 20µm, the value of N_f has changed little with increase in the solder joints thickness. The results in Figure 62 shows that the value of N_f increases linearly with increasing silver-pad thickness which are in very good agreement with results for the effect of silver-pad thickness on crack initiation temperature and crack growth rate presented in Figure 38 and Figure 39, Section 4.3.5, Chapter 4. Also, Figure 63 shows that increasing the copper thickness can cause a slight decrease in the value of N_f. According to Figure 63,an increase of the copper thickness from 150µm to 250µm causes about 8% reduction in the value of N_f. This finding is highly consistent with the results obtained for the cracking parameters in Section 4.3.5, Chapter 4. The results in Figure 64 demonstrates that when the ribbon width is more than 1000µm, altering the ribbon width has a negligible influence on N_f. This finding corresponds extremely well with the results regarding the effect of copper thickness on the crack initiation temperature presented in Figure 29, Section 4.31, Chapter 4.

Table 11 summarizes the results of N_f for the solder joint in different configurations of the CR interconnection (28 samples) under standard thermal cycling condition. Comparing the results shown in

Table 11 helps to select an optimal design for the conventional PV module interconnection in which the value of N_f is enough high and the consumption of the material is reasonable. As a case of matter, the conventional PV module interconnection with 1000µm ribbon width, 200µm copper thickness, 20µm solder thickness and 40/50µm silver-pad thicknesses (sample number #2/#14) are suggested.

Figure 61: Number of cycles to failure (N_f) for the CR interconnections with different solder thickness, under standard thermal cycling condition.

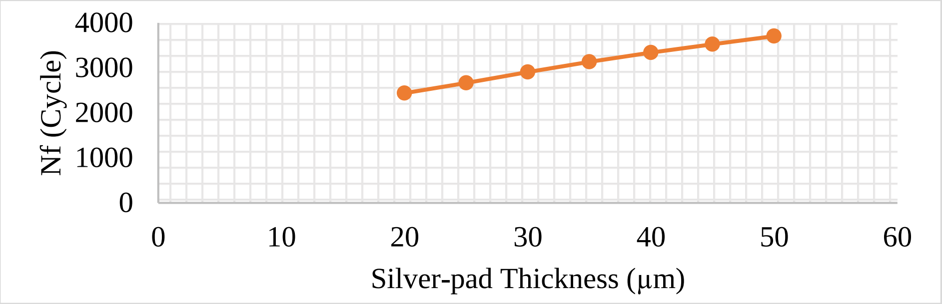

Figure 62: Number of cycles to failure (N_f) for the CR interconnections with different silver-pad thickness, under standard thermal cycling condition.

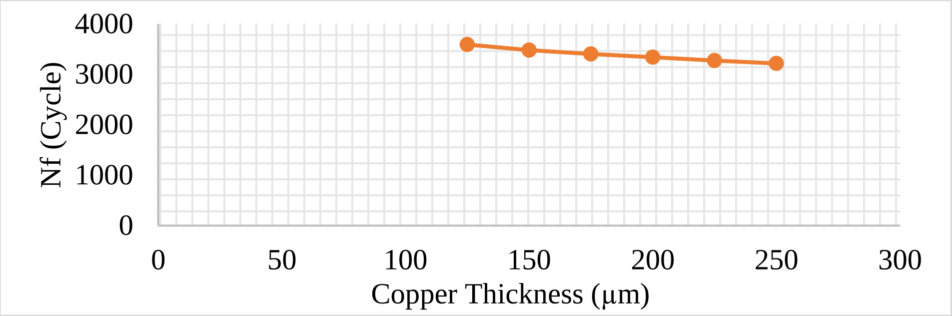

Figure 63: Number of cycles to failure (N_f) for the CR interconnections with different copper thickness, under standard thermal cycling condition.

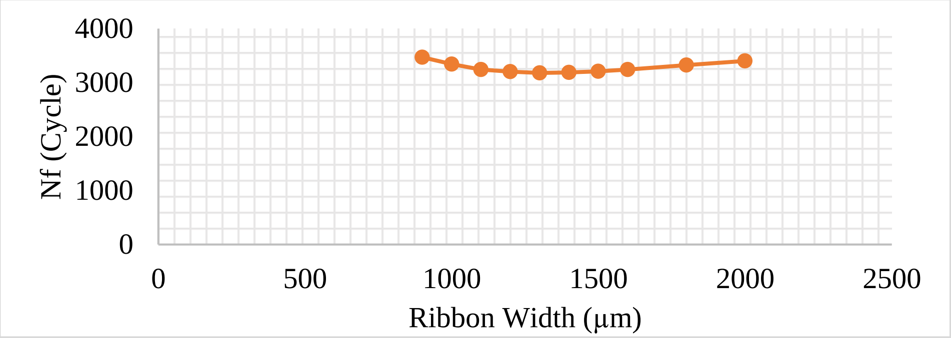

Figure 64: Number of cycles to failure (N_f) for the conventional PV module interconnection with ribbon width, under standard thermal cycling condition.

Table 11: Number of cycles to failure (N_f) for different configurations of the conventional PV module solder joint interconnection under standard thermal cycling condition.

	Ribbon Width (µm)	Copper Thickness (µm)	Silver-pad Thickness (µm)	Solder Thickness (µm)	Number of Ribbons	N_f (Cycle)	Sample Number
Solder Thickness Changes	1000	200	40	**15**	**5**	**2574**	**1**
	1000	200	40	**20**	**5**	**3334**	**2**
	1000	200	40	**25**	**5**	**3457**	**3**
	1000	200	40	**30**	**5**	**3556**	**4**
	1000	200	40	**35**	**5**	**3637**	**5**
	1000	200	40	**40**	**5**	**3703**	**6**
	1000	200	40	**45**	**5**	**3751**	**7**
	1000	200	40	**50**	**5**	**3784**	**8**
Silver Thickness Changes	1000	200	**20**	20	**5**	**2440**	**9**
	1000	200	**25**	20	**5**	**2665**	**10**
	1000	200	**30**	20	**5**	**2907**	**11**
	1000	200	**35**	20	**5**	**3134**	**12**
	1000	200	**40**	20	**5**	**3334**	**2**
	1000	200	**45**	20	**5**	**3526**	**13**
	1000	200	**50**	20	**5**	**3708**	**14**
Copper Thickness Changes	1000	**125**	40	20	**5**	**3593**	**15**
	1000	**150**	40	20	**5**	**3481**	**16**
	1000	**175**	40	20	**5**	**3404**	**17**
	1000	**200**	40	20	**5**	**3334**	**2**
	1000	**225**	40	20	**3**	**3277**	**18**
	1000	**250**	40	20	**3**	**3219**	**19**
Ribbon Width Changes	**900**	200	40	20	**5**	**3471**	**20**
	1000	200	40	20	**5**	**3334**	**2**
	1100	200	40	20	**5**	**3244**	**21**
	1200	200	40	20	**5**	**3205**	**22**
	1300	200	40	20	**3**	**3181**	**23**
	1400	200	40	20	**3**	**3189**	**24**
	1500	200	40	20	**3**	**3210**	**25**
	1600	200	40	20	**3**	**3243**	**26**
	1800	200	40	20	**3**	**3327**	**27**
	2000	200	40	20	**2**	**3403**	**28**

6.2.4. Fast Cycling Test

In this section, the modified Coffin–Manson–Arrhenius lifetime model is used to predict the creep life of the solder joints in which this model considers the cycling temperature as the main parameter that affects the creep fatigue life. The analytical formula that describes the relation between the number of cycles to failure, N_f and the temperature intervals (ΔT) of cycles is presented in Equation #7, Section 3.2.2, Chapter 3. However, in Equation #7, the value of exponent factor, α, for the PV module solder joint interconnection, needs to be defined by comparing N_f for different thermal cycling loads (with different ΔTs). For this, the value of N_f is firstly calculated (according to the approach presented in Section 6.2.3) for a selected design (Sample Number #2 in

Table 11) under different thermal cycling loads (i.e. field and test cycling conditions), and then using the Equation #7 gives the exponent factor (α).

Table 12 shows the calculated values of accumulated creep energy density per cycle (w_{acc}) for the selected design under different cycling conditions. The values of w_{acc} are calculated (by using Equation #9, Section 3.2.2, Chapter 3) for the each first 5 cycles, and the average value of w_{acc} for the solder elements between interconnecting materials is used to estimate the number of cycles to failure (N_f) (see Equation #8, Section 3.2.2, Chapter 3). Then, using Equation #7, Section 3.2.2, Chapter 3 gives the value of α based on the comparison of the each field thermal cycling condition with the test thermal cycling condition (temperature ranging from -40°C to 85°C). The results of the study presented in Table 12, shows that there is good convergence in the values of w_{acc} for each of the five cycles used for investigating the thermal cycling scenarios; and this provides confirmation that the FEM simulation of the PV module interconnection has been implemented accurately.

To find the generic value of $\boldsymbol{\alpha_m}$ for a given field thermal cycling condition and design, we use the mean value of the calculated α values (see Table 12), which is found to be $\boldsymbol{\alpha_m}$ -1.8. This $\boldsymbol{\alpha_m}$ (generic value) found for the PV module interconnection operating under any field thermal cycling condition, can be substituted into Equation #5, Section 3.2.2, Chapter 3 to determine the number of cycles to failure (N_f) and the associated the creep-fatigue life. This generic value for the exponential factor found in this study can be used for evaluating potential design changes and to facilitate design for reliability validation of different configurations to improve the long-term PV module system reliability.

Table 12: Averaged accumulated creep energy density in the solder elements between interconnecting materials and α for different thermal cycling conditions.

T_{min} (°c)	T_{max} (°c)	T_m (k)	ΔT (k)	**accumulated creep energy density per cycle, w_{acc}, ($\frac{mJ}{mm^3}$)**					N_f (Cycle)	α
				w_{acc_1}	w_{acc_2}	w_{acc_3}	w_{acc_4}	$w_{acc_{ave.}}$		
-40	**85**	**296**	**125**	**0.157**	**0.158**	**0.158**	**0.158**	**0.158**	**3334**	-
-20	70	298	90	0.088	0.088	0.088	0.088	0.088	5983	-1.93
-10	70	303	80	0.071	0.072	0.072	0.072	0.072	7351	-2.11
-10	60	298	70	0.055	0.055	0.055	0.053	0.055	9530	-1.90
-10	50	293	60	0.042	0.042	0.042	0.040	0.042	12592	-1.74
-10	40	288	50	0.030	0.030	0.030	0.030	0.030	17311	-1.63
-20	60	293	80	0.070	0.070	0.070	0.068	0.070	7271	-1.70
-20	50	288	70	0.055	0.055	0.055	0.055	0.055	9510	-1.54

6.2.5. Creep-Fatigue Life Estimation

The number of cycles per day used for calculating the creep-fatigue life for PV module operating under thermal cycling has generally been assumed to be l.5 cycles per day (Guyenot, et al., 2011); and this rate 1.5 cycles per day is then used to determine the numbers of years to failure (. The effect of different parameters (namely: solder thickness, silver-pad thickness, copper thickness and ribbon width), on the creep-fatigue lifetime of the conventional PV module interconnection (operating under 3 different thermal cycling loads, namely: from temperature ranges of 10°C to 50°C, 0°C to 50°C and 0°C to 60°C) are presented in Figure 65 to Figure 68. The results show that for all PV module interconnection dimensions studied, the creep-fatigue lifetime calculated for the thermal cycling loads (namely: the 10°C to 50°C and the 0°C to 50°C) are identical. The estimation of the creep-fatigue life for all cases show that the maximum temperature of the cycling load massively impacts the creep-fatigue lifetime; as by increasing the high temperature extreme of the cycle from 50°C to 60°C, the creep-fatigue lifetime decreased by 50%. However, it is found that the minimum temperature of the cycling load (from 10°C to 0°C) has only ~5% decrease in creep-fatigue lifetime.

The results in Figure 65 shows that for solder joints thicker than 20μm, there is little or no change in the creep-fatigue lifetime with increase in the solder joints thickness. For instance, the creep-fatigue lifetime of the solder joint of interconnection under thermal cycling in range of 0°C to 50°C ($\Delta T = 50°C$) is 26.5 years which has a very good agreement with the reported life (25 years) for similar configuration studied by Guyenot (Guyenot, et al., 2011). This provides further validation for the methodology used for this section, as reported in Chapter 4. The results in Figure 66 show that the creep-fatigue lifetime increases linearly with increasing silver-pad thickness. For example, increasing the silver-pad thickness from 20μm to 50µm leads to an increase of about 50% in the creep-fatigue lifetime. Also, the results presented in Figure 67 and Figure 68, show that changing the copper thickness and ribbon width has very marginal effect on the creep-fatigue lifetime (less than 10%).

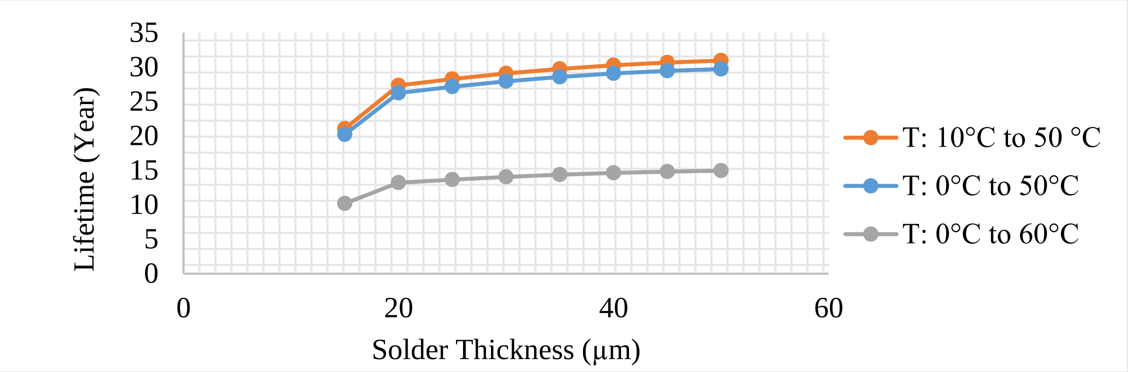

Figure 65: Effect of solder thickness on the creep-fatigue lifetime of the conventional PV module interconnection operating under 3 different thermal cycling conditions.

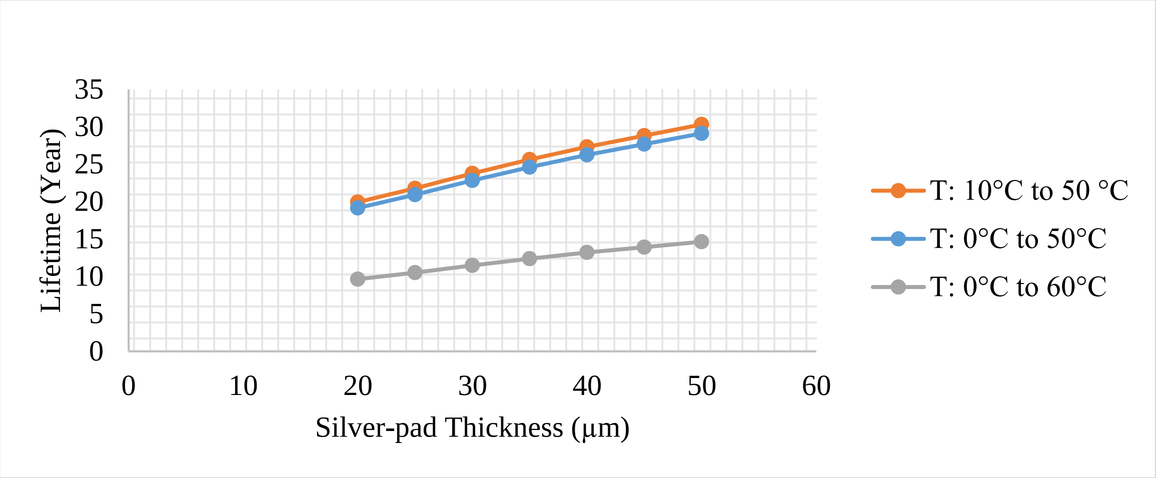

Figure 66: Effect of silver-pad thickness on the creep-fatigue lifetime of the conventional PV module interconnection operating under 3 different thermal cycling conditions.

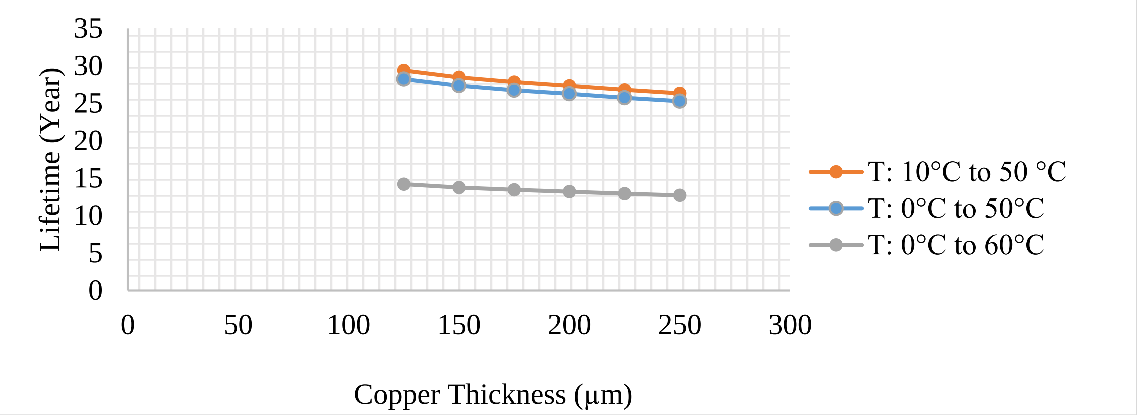

Figure 67: Effect of copper thickness on the creep-fatigue lifetime of the conventional PV module interconnection operating under 3 different thermal cycling conditions.

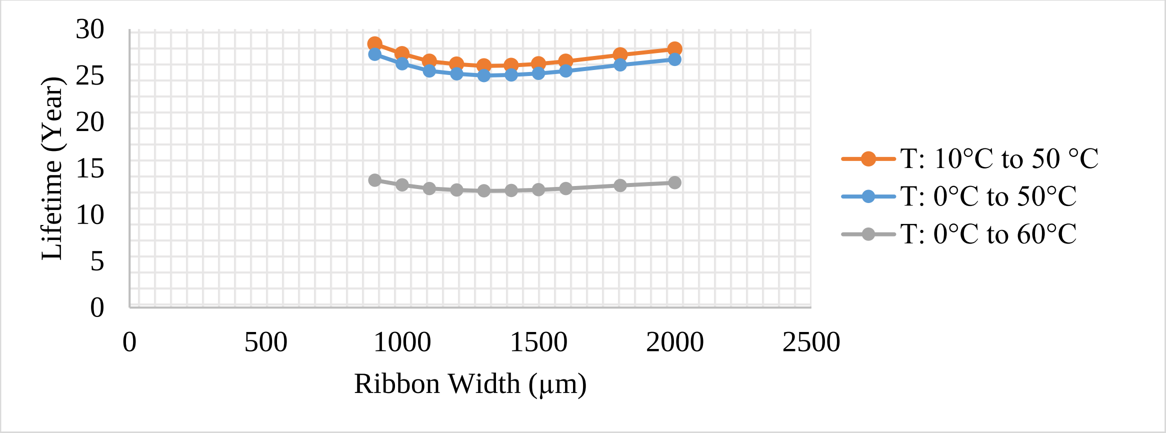

Figure 68: Effect of ribbon width on the creep-fatigue lifetime of the conventional PV module interconnection operating under 3 different thermal cycling conditions.

6.3. Creep in the New PV Module Solder Joint Interconnection

This section presents the creep-fatigue analysis for the SAC solder joints used in the LCR and MBB interconnection of PV modules. To find the best design parameters of the LCR and MBB interconnection configuration, several designs are investigated in which, the designs with higher failure life that can provide higher thermo-mechanical reliability are found. Table 13 summarizes the design parameters for the investigated LCR and MBB interconnections in this section. As Table 13 introduces seven 2-cases for the LCR and MBB interconnections to access the effect of the LCR width and the MBB diameter on the number of cycles to creep-fatigue failure (N_f). The required number of ribbons are also considered to have same cross-section of area for both ribbon interconnection types. For example, the case number #1 for MBB interconnection uses 15 ribbons with 276µm diameters (0.9mm^2 cross-section area) which is comparable with the LCR interconnection with 5 ribbons and 900µm ribbon width. The maximum thickness of the LCR interconnections presented in Table 13 is considered 250µm (the average thickness is 200µm). Also, the solder thickness for both LCR and MBB interconnection are assumed 20µm and the silver-pad thicknesses are 40µm and 20µm for the LCR and MBB interconnection, respectively. It should be noted that in this section, the molten solder height for the MBB interconnection is assumed half of the solder thickness; and it is also assumed that the solder material is homogenously coated on the copper.

Table 13: Dimensions and numbers of the LCR and MBB ribbon interconnections for the creep-fatigue analysis.

	MBB Interconnection			**LCR Interconnection**		
Case Number	**Ribbon Diameter (µm)**	**Ribbons Numbers**	**Cross-section Area (mm^2)**	**Ribbon Width (µm)**	**Ribbons Numbers**	**Cross Section Area (mm^2)**
1	276	15	0.90	900	5	0.90
2	291	15	1.00	1000	5	1.00
3	306	15	1.10	1100	5	1.10
4	319	9	0.72	1200	3	0.72
5	332	9	0.78	1300	3	0.78
6	345	9	0.84	1400	3	0.84
7	357	9	0.90	1500	3	0.90

Furthermore, to separately find the effect of design parameters (copper ribbon, solder joint, silver-pad thicknesses) on the creep-fatigue life of the solder joints in each type of the interconnections, several simulations are investigated. Indeed, the changes of 3 copper ribbon thicknesses (125µm, 187µm and 250µm), 8 solder joint thicknesses (ranging from 10µm to 30µm) and 7 silver-pad thicknesses (ranging from15µm to 50µm) are considered for the simulations of the LCR interconnections with 1000µm ribbon width. Also, the solder thickness and silver-pad thickness for MBB interconnections are similarly changed from 10µm to 30µm, and from15µm to 50µm, respectively.

6.3.1. FEM Simulation

The steps for the FEM simulations of the introduced LCR and MBB interconnections including the material arrangement, meshing style, boundary conditions are according to Section 3.5, Chapter 3. Indeed, the material properties for creep-fatigue analysis presented in Table 3,

Table 4 and Table 6 are used; and also the thermal cycling creep-fatigue condition in accordance with the IEC 61215-2:2016 (see Figure 21) is applied to the models.

The methodology introduced in Section 3.2.2, Chapter 3, is used to estimate N_f and to predict the creep-fatigue life. For this, similar to Section 6.2, developed Morrow Energy Density model is used to find the N_f and then using the modified Coffin-Manson–Arrhenius model (considering the exponent factor, α, found in Section 6.2), the creep-fatigue life of the new PV module solder joint interconnections are calculated.

6.3.2. Results and Discussion

6.3.2.1. Effect of LCR width and MBB Diameter

To find effect of the LCR width, the MBB diameter on the number of cycles to failure (N_f) for the new PV module interconnections, several samples (presented in Table 13) are simulated using FEM and according to the methodology in Section 6.2.

Figure 69 and Figure 70 show the effect of LCR width and MBB diameter, respectively, on the value of N_f for the LCR and MBB designs under thermal cycling condition (temperature ranging from -40°C to 85°C). Figure 69 shows that for LCR interconnections with width less than 1100μm (using 5 ribbons), the value of N_f is slightly decreased (≤6%) when the ribbon width is increased. However, for the LCR with higher widths, there is not any significant change in the N_f. Figure 70 also shows that with an increase of the MBB diameter, there is a slight reduction in the N_f (≤10%) which means that MBB interconnection with more ribbons (15 ribbons) but with lower diameter (276μm) can provide higher thermo-mechanical reliability for the PV module.

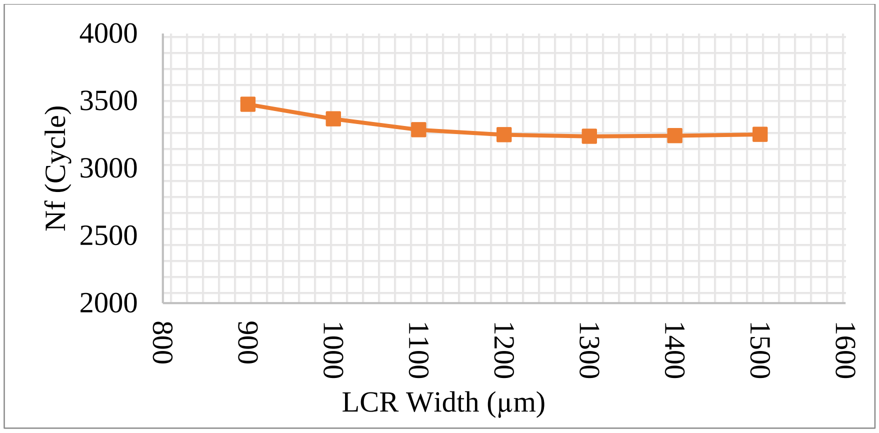

Figure 69: Effect of LCR width on the number of cycles to failure (N_f) in PV modules under standard thermal cycling condition.

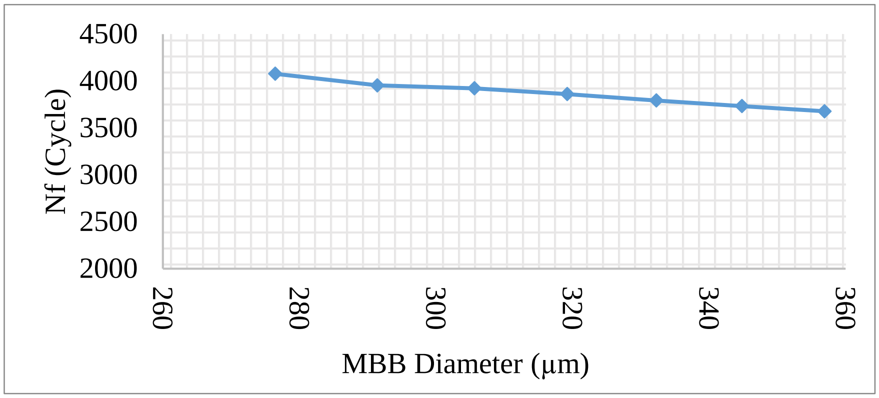

Figure 70: Effect of MBB diameter on the number of cycles to failure (N_f) in PV modules under standard thermal cycling condition.

Figure 71 compares the value of N_f for the LCR and MBB designs presented in Table 13. It is seen that the MBB interconnection designs can provides higher reliability compared to the LCR interconnection designs due to having higher N_f (10% to 15% higher). Also, as Figure 71 suggests, the samples number #1 has higher value of N_f rather than other samples, which means that using the MBB interconnection with 15 ribbons with diameter of 276µm; and also using a design with 5 LCR interconnections with 900µm width can provide more reliability. However, the LCR interconnections with 1000µm width (sample number #2) can be also suggested as it provides almost same N_f, and it provides more cross-section of area compared to the sample number #1; and this means that there is less electrical resistance in the ribbon designed based on the sample number #2. Similarly, to have consistency in the cross-section of areas of ribbons, the MBB interconnection sample number #2 (with diameter of 291µm) is selected for finding the effect of geometrical parameters on the creep-fatigue lifetime of different PV module ribbon interconnection designs.

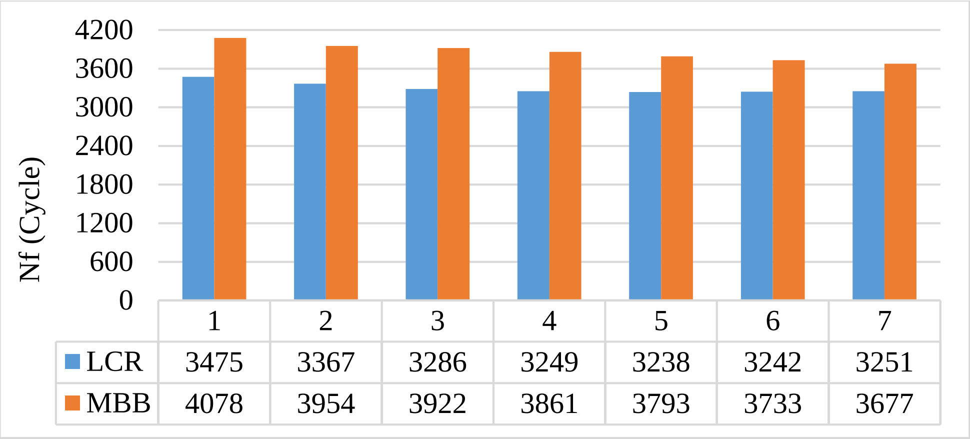

Figure 71: Number of cycles to failure (N_f) for different design cases of the LCR and MBB interconnections with same cross-section areas, but with different ribbon width/diameter and numbers. The modelling results are obtained for the PV modules under standard thermal cycling condition.

6.3.2.2. Effect of Solder and Copper Thickness

Figure 72 shows the effect of solder thickness and also copper (ribbon) thickness on the value of N_f for the LCR interconnection deigns using 5 ribbons with 1000µm width and 40µm silver-pad thickness. The results show that an increase in the solder joint thickness leads to a slight increase in N_f (up to 5%). In addition, Figure 72 shows that increasing the copper thickness leads to a decrease in N_f, in which the LCR interconnection with 187µm copper thickness provides about 6% higher N_f, when it is compared to the LCR interconnection with 250µm copper thickness. The results shown in Figure 72 suggests that a LCR interconnection with 20µm solder joint thickness and 187µm copper thickness can be an optimal design as this configuration provides high value of N_f (3850 cycles), but it remarkably saves the material consumptions. This finding is consistent with the results obtained for the cracking parameters in Section 5.2.3., Chapter 5.

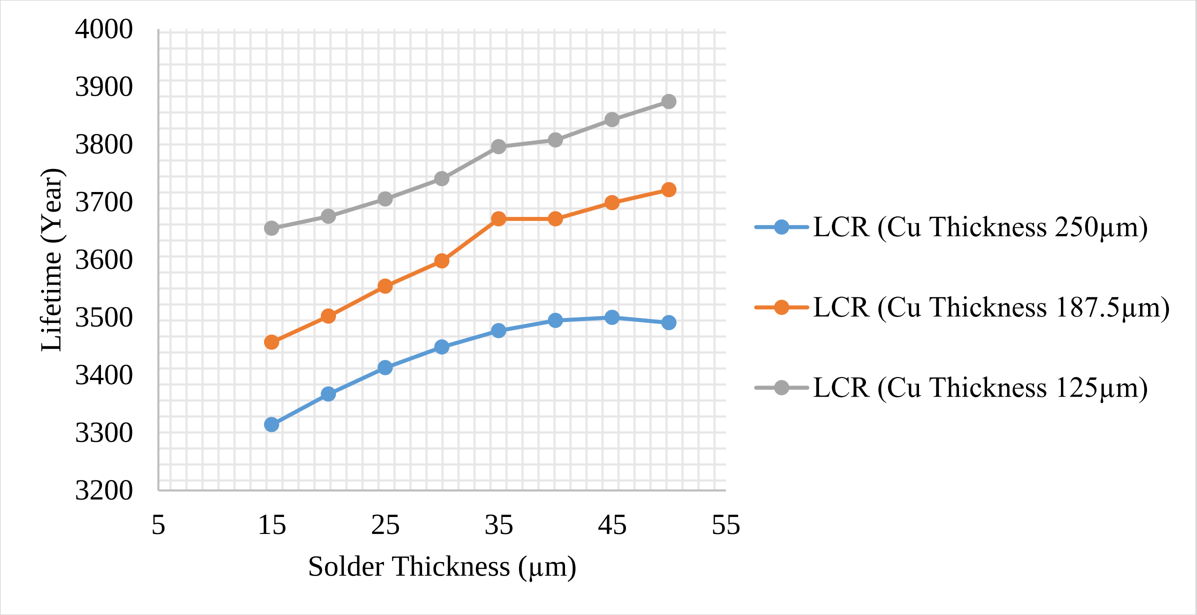

Figure 72: Effect of solder and copper thickness on N_f for the LCR interconnection design under standard thermal cycling condition.

6.3.2.3. Effect of Silver-pad and Solder Thickness

Figure 73 shows the effect of silver-pad thickness on the associated N_f for the LCR and MBB interconnections with 20µm solder thickness. Copper thickness of the LCR interconnection and ribbon diameter of the MBB interconnection are considered 187µm and 291µm, respectively. It is shown that increasing the silver-pad thickness from 20µm to 50µm causes 32% increase of N_f for the LCR interconnection. However, Figure 73 suggests that there is no change of N_f when the silver-pad thickness of the MBB interconnection increases. To re-check the effect of solder thickness on the reliably of the MBB interconnection, the results of creep-fatigue analysis for the MBB interconnections with different solder joint thicknesses are presented in Figure 74. As Figure 74 shows, increasing the solder thickness results in an increase of N_f for the MBB interconnections, in which for the MBB interconnection with 40µm silver-pad thickness, the increase of the solder thickness from 10µm to 15µm causes a significant increase in the N_f (166%). However, for the MBB interconnection with solder thickness thicker than 15µm, there is also a linear increase in N_f (up to 22%) in which the N_f is not affected by the silver-pad thickness. Consequently, the MBB interconnection with 20µm solder and silver-pad thickness can suggest more reliability for the PV module and also can help to save the material consumption.

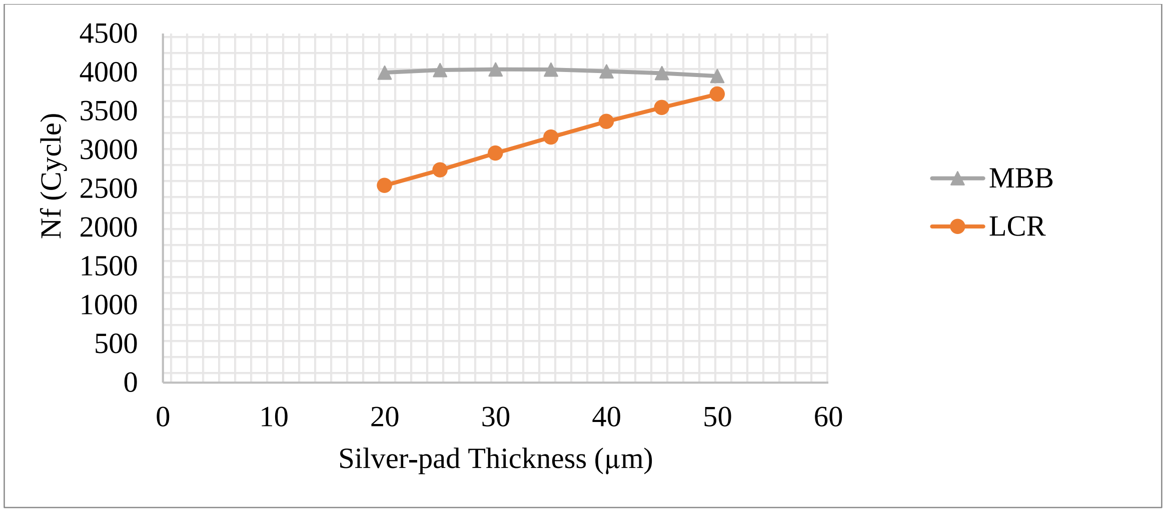

Figure 73: Effect of silver-pad thickness on the N_f for the LCR and MBB interconnection designs under standard thermal cycling condition.

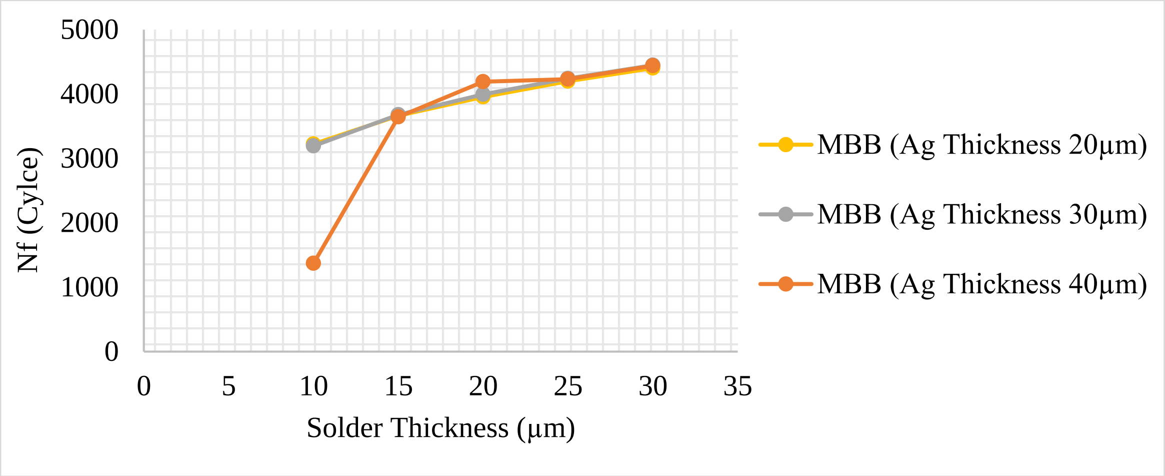

Figure 74: Effect of solder thickness and silver-pad thickness on the N_f for the MBB interconnection design under standard thermal cycling condition.

6.3.2.4. Creep-Fatigue Life Estimation

To estimate the creep-fatigue lifetime of the solder joints in the MBB and LCR interconnections operating under field thermal cycling with different ΔTs, the modified Coffin–Manson–Arrhenius lifetime model (with the found value of α in Section 6.2.4) is used according to the methodology explained in Section 3.2.2, Chapter 3. Figure 75 and Figure 76 show the estimated creep-fatigue lifetimes of solder joints for the LCR interconnection with 1000µm width, 40µm silver-pad thickness and 187µm copper thickness; and in the MBB interconnection with diameter 291µm and silver-pad thickness 20µm, respectively. Three different thermal cycling loads, namely: from temperature ranges of 10°C to 50°C, 0°C to 50°C and 0°C to 60°C are considered for the ribbon interconnections and the results are provided for the different solder joint thicknesses. The results shown in Figure 75 and Figure 76 suggest that the MBB interconnection creep-fatigue lifetime experiences higher increase by increasing the solder thickness when it is compared to the LCR interconnection design. Comparison of the results for the thermal cycling loads shows that by increasing the maximum temperature of the cycling load from 50°C to 60°C, the creep-fatigue lifetime decrease by 50%; however, it is found that the minimum temperature of the cycling load has less 3% reduction effect on the creep-fatigue lifetime values.

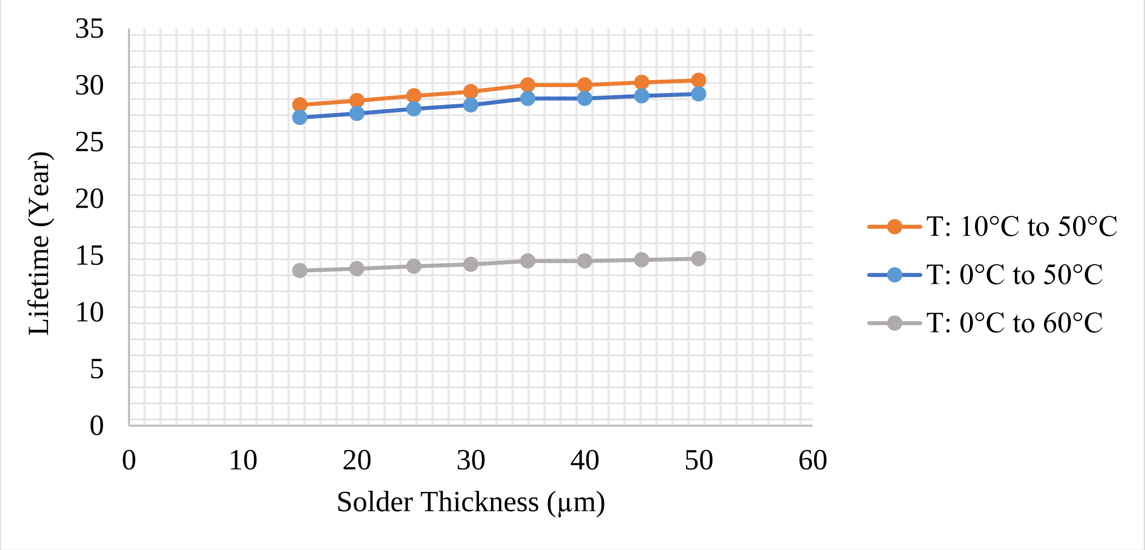

Figure 75: Creep-fatigue lifetime of the LCR interconnection with different solder thickness operating under 3 different thermal cycling conditions.

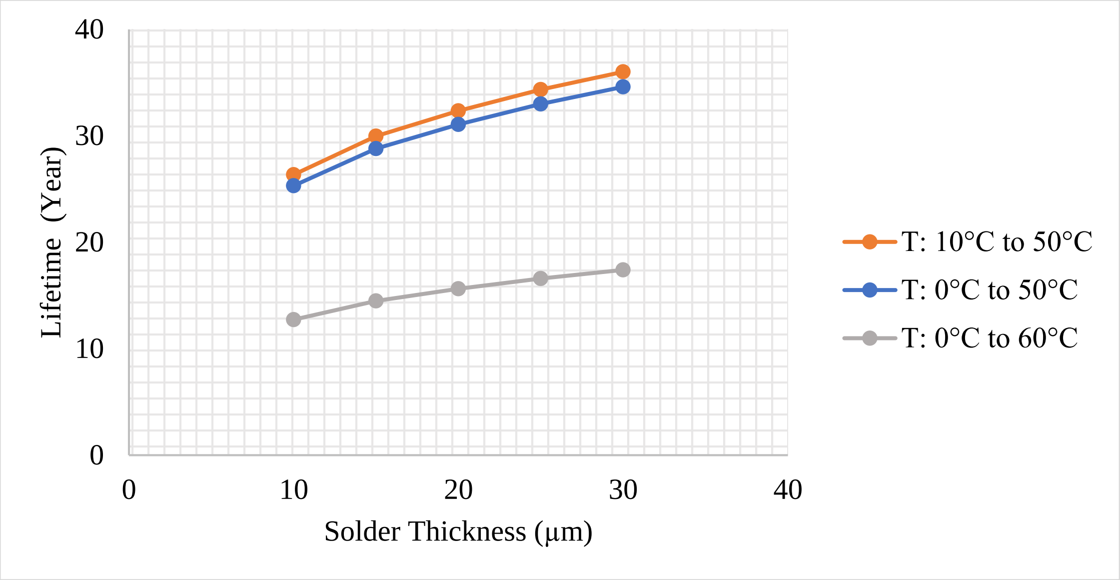

Figure 76: Creep-fatigue lifetime of the MBB interconnection with different solder thickness operating under 3 different thermal cycling conditions.

6.4. Chapter Summary and Conclusion

The strain and stress induced by the field thermal cycling loads leads to the creep-fatigue failure mode of the solder joint which adversely affect the reliability of the PV module and in this study, the FEM simulation in ABAQUS 2019 is implemented to study the creep behaviour of the solder joints for the three PV module interconnection designs with different dimensions.

Our results show that the maximum shear creep strain in the solder joint is located at the corner of the connection area in copper side; and that this location has the highest potential for creep fatigue failure during the operation. In the study, the total dissipated energy is used to find the number of cycles to failure for each of the PV module interconnections operating under the test and field thermal cycling load. The exponent factor of Coffin–Manson–Arrhenius approach for determining the creep-fatigue life of the PV module interconnections was determined to be -1.8; and this generic exponent factor value was then used to determine the solder joint's creep-fatigue life under thermal cycling operating conditions. The estimation of the creep-fatigue life for all cases show that the maximum temperature of the cycling load has significant impact on the creep-fatigue lifetime; as by increasing the maximum temperature from 50°C to 60°C, the creep-fatigue lifetime decreases by 50%. Similarly, the results show that the minimum temperature of the cycling load has much less effect on the creep-fatigue lifetime (~5%).

The results of investigations of the CR, LCR and MBB interconnections show that the creep-fatigue lifetime decreases (up to 10%) when wider ribbons are used. The results also show that changing the solder joints thickness in the LCR interconnections had very marginal effect on the creep-fatigue lifetime (≤ 5%); however, the results of investigations of the CR and the MBB interconnection show that with increasing the solder joints thickness, the creep-fatigue lifetime increases up to 23%. In addition, it is found that the creep-fatigue lifetime increases linearly with an increase of the silver-pad thickness up to 34%, 32 % and 6% for the CR, LCR and MBB interconnection designs, respectively. It is also found that using the thicker ribbons results in a reduction of the creep-fatigue lifetime (≤ 11%). These findings are almost consistent with the results obtained from the XFEM simulation of the crack analysis in solder joints subjected to the lamination process (presented in Chapter 4 and Chapter 5). Table 14 summarizes the results of the creep-fatigue lifetime change for different configurations of the PV module interconnection.

Table 14: creep-fatigue lifetime change for different configurations of the PV module interconnection.

Interconnection Design	**CR**		**LCR**	**MBB**
Ribbon Width Range (µm)	900 to 1300	1300 to 2000	900 to 1500	276 to 357
Ribbon Width Effect	-9.00%	6.50%	-7%	-10%
Solder Thickness Range (µm)	20 to 50	15 to 20	15 to 50	15 to 30
Solder Thickness Effect	11.00%	23.00%	5%	22%
Silver-pad Thickness Range (µm)	20 to 50	20 to 50	20 to 50	20 to 40
Silver-pad Thickness Effect	34%	34%	32%	6%
Copper Thickness Range (µm)	125 to 250	125 to 250	125 to 250	276 to 357
Copper Thickness Effect	-11%	-11%	-10%	-10%

In summary, the methodology developed for this study to investigate the effect of the four geometrical parameters on the creep-fatigue lifetime of different PV module ribbon interconnection designs has provided the results for determining the optimal design for long-term reliability. For example, based on the modelling results, a design with the 20µm solder thickness, the 40µm-50µm silver-pad thickness, the 150µm-200µm copper thickness and the 1mm ribbon width is recommended. Table 15 depicts the recommended configurations for different PV module ribbon interconnection designs according to the creep-fatigue lifetime. As Table 15 suggests, the MBB interconnections can provide more thermo-mechanical reliability compared to the LCR and the CR interconnection designs (up to 15%). It should be also noted that the recommended configurations in this chapter are in agreement with the recommended PV module interconnections resulted from the XFEM simulation of the crack analysis reported in Chapter 4 and Chapter 5.

Table 15: Recommended configurations for different PV module ribbon interconnection designs according to the creep-fatigue lifetime.

Geometrical Parameters	**CR**		**LCR**		**MBB**	
Designs	**1st**	**2nd**	**1st**	**2nd**	**1st**	**2nd**
Ribbon Width (µm)	1000	1000	1000	900	276	291
Solder Thickness (µm)	20	20	20	20	20	20
Silver Thickness (µm)	40	40	40	40	20	20
Copper Thickness (µm)	150	200	187	250	276	276
Number of Ribbons	5	5	5	5	15	15
Copper cross-section of area (mm^2)	0.75	1	0.75	0.9	0.9	1.0
N_f (Cycle)	3481	3334	3502	3475	4078	3954

Chapter 7

7. Discussion of Results

In this chapter, the main FEM results for the PV module ribbon interconnection designs presented in Chapter 4 to 6, are compared to determine the optimum configurations in terms of the thermo-mechanical reliability and the material consumption.

A very good agreement between the XFEM findings and the results of creep-fatigue investigation on the thermal failure of the PV modules solder joint interconnections are found. The results from the XFEM simulation provided in Chapter 4 and Chapter 5 showed that in all PV modules interconnection designs, location for the crack nucleation is at the edge of IMC interface layers and the crack propagates in the shear direction. Also, the results of creep analysis presented in Section 6.2.2, Chapter 6, showed that the maximum shear creep strain in the solder joint is located at the side of the IMC layer. The effect of different PV module ribbon interconnection configurations and design parameters (namely: solder thickness, silver-pad thickness, copper thickness and ribbon width) on the XFEM results (crack initiation temperature and crack growth rate) and also on the creep-fatigue life are compared in the sub-sections below.

7.1. Effect of Ribbon Width Change

Figure 29 and Figure 30 showed that increasing the ribbon width leads to an increase in the crack initiation temperature (positive effect) and an increase in the crack growth rate (negative effect) for the CR PV module interconnection; and it is resulted that the ribbon interconnection with widths of circa 900µm - 1000µm (for cell tabbing using 5 ribbons) are the best choices in terms of the thermo-mechanical reliability as this gives high crack initiation temperature, but no high crack growth rate. Figure 68 also showed that by increasing the ribbon width, there is a marginal reduction in the number of cycles to creep-fatigue failure (N_f) and it is suggested to use the CR interconnection with the width mentioned above. In addition, as Figure 69 showed there is a similar reduction trend for N_f when the LCR ribbon width increases.

In conclusion, for the CR and the LCR interconnection, the 900µm - 1000µm ribbon width is recommended when 5 ribbons are used for cell tabbing in the solar PV module.

7.2. Effect of Copper Thickness Change

As it was shown in Figure 33, increasing the copper thickness from 150μm to 200μm leads to a reduction in the crack growth rate for the CR interconnections under the high temperature lamination process; and the lowest crack growth rate occurs at the 200μm copper thickness. However, Figure 32 showed that increasing the copper thickness results in a reduction in the crack initiation temperature for the CR interconnection design. The summation of the effects of copper thickness changes on the crack initiation temperature and the crack growth rate for the CR interconnections showed there is a slight increase in the crack length when the copper thickness increases (see Figure 46). These results are consistent with the results of N_f shown in Figure 67, as it was shown that thicker copper used for the CR interconnections experienced a marginal decrease of N_f. Also, for the LCR interconnection, as shown in Figure 42 and Figure 43, increasing the copper thickness results in lower crack initiation temperature, but higher crack growth rate in which the thicker copper interconnections cause longer cracks in the solder joints during the lamination process. This finding was in agreement with the creep-fatigue results provided in Figure 72 in which the thicker LCR interconnections have the lower N_f. Furthermore, Figure 70 showed that increasing the diameter of MBB interconnection leads to a marginal decrease of N_f in which the highest value of N_f was found for the MBB interconnection with the lowest diameter (276μm).

In conclusion, for the CR interconnection, the 150μm - 200μm copper thickness is recommended; and also for the LCR interconnection, the 125μm - 250μm copper thickness is recommended and for the MBB interconnection, the 276μm diameter is the optimum dimension of the copper.

7.3. Effect of Silver-pad Thickness Change

Figure 44 and Figure 45 showed that the crack initiation temperature and the crack growth rate decrease with increasing silver-pad thickness for the LCR and the CR interconnections. This finding is consistent with the found N_f for different silver-pad thicknesses (see Figure 66 and Figure 73). However, Figure 73 also showed that for the MBB interconnection, there is no significant change of N_f via the silver-pad thickness changes.

In conclusion, for the LCR and the CR interconnections, the 40μm silver-pads thickness is recommended, and for the MBB interconnection, the 20μm silver-pads thickness which also results in smaller silver material consumption is recommended.

7.4. Effect of Solder Thickness Change

As shown in Figure 42, for the CR interconnection when the copper thickness is between 150µm and 200µm, the highest crack initiation temperature is occurred at 20µm solder thickness. Also, Figure 42 showed that for all copper thicknesses of the LCR interconnection, the 20µm solder thickness has the highest crack initiation temperature. Similarly, Figure 43 showed that for the solder thicknesses of 10µm - 30µm, the crack growth rate slightly increases with increasing the solder thickness. In addition, Figure 54 showed that for the MBB interconnection solder joint thicker than 20µm, increasing the solder thickness sharply reduces the crack initiation temperature and the highest crack initiation temperature is at the solder thickness of 15µm - 20µm.

The results of creep-fatigue investigation for the three interconnection designs (see Figure 65, Figure 72, Figure 74) showed that increasing the solder thickness leads to a marginal increase in the N_f. However, the solder thickness of 20µm is recommended for all ribbon interconnection designs due to less smaller material consumption, but still providing the high N_f.

In conclusion, for all ribbon interconnection designs, the 20µm solder coating thickness is recommended as this leads to lower crack growth rate, but the higher N_f and crack initiation temperature; and this gives an increase in the PV ribbon interconnection reliability.

7.5. Recommended Configurations for the PV Module Interconnection Designs

Section 7.1 to Section 7.4 compared the results of XFEM simulation and creep-fatigue investigation for the different PV module interconnection designs used in this study. The recommended configurations for the three PV module interconnection designs are determined to provide the optimum thermo-mechanical reliability and to reduce the solder and the silver consumptions. In this regard, four configurations for the CR interconnections, three configurations for the LCR and three configurations for the MBB interconnections are selected to be compared in terms of the initial crack (due to the high temperature lamination process) and the value of N_f (under thermal cycling condition with temperature ranging from -40°C to 85°C). Table 16 presents dimensions of the selected PV module interconnections, and it also shows the high temperature crack specifications (crack initiation temperature and crack growth rate) and the value of N_f (with and without considering the initial crack) for the selected PV module interconnection configurations.

Table 16 shows that the best configuration for the CR interconnection uses 5 ribbons with the 900µm ribbon width, the 200µm copper thickness, the 20µm solder thickness and the 40µm silver-pad thickness.

This configuration has 0.9mm^2 cross-section area of the copper which helps to keep the electrical resistance low. As it is shown, this configuration exhibits a 4.0% cracked section (18μm initial crack length) due to the high temperature lamination process, and when the initial crack length is considered, the N_f 3331 cycles (ranging from -40°C to 85°C). It should be noted that sample number #4, without considering the initial crack has the higher N_f (3481 cycles), however, its N_f with considering the initial crack, the N_f is 2873 cycles which is lower than N_f for other configurations (due to the large initial crack).

As Table 16 shows, using 5 ribbons with 1000μm ribbon width, with 187μm copper thickness, with 20μm solder thickness and with 40μm silver-pad thickness (0.75mm^2 total cross-section area of the copper) is recommended for the LCR interconnection, in which this configuration can endure the 3281 thermal cycles (ranging from -40°C to 85°C). However, the sample number #2 with the 900μm ribbon width and the 250μm copper thickness which has the lower electrical resistance can be also recommended (N_f is 3114 cycles and the total cross-section of copper is 0.9mm^2).

In addition, Table 16 shows that for the MBB interconnection, with 15 ribbons, with 291μm and 276μm copper diameters, with 20μm solder thickness and with 20μm silver-pad thickness provides higher N_f (3813 and 3808 cycles, respectively) compared to the sample number #3 with 15μm silver-pad thickness. Table 16 also shows that the MBB interconnection has higher N_f (i.e. higher thermal creep-fatigue lifetime) compared to the CR and the LCR interconnection designs.

Table 17 shows the estimated creep-fatigue life of the solder joint in the recommended ribbon interconnection designs (presented in Table 16) in the solar PV module operating under 3 different thermal cycling loads, namely: from temperature ranges of 10°C to 50°C, 0°C to 50°C and 0°C to 60°C. It is shown that the MBB interconnection provides 15% thermal creep-fatigue lifetime more than to the CR and the LCR interconnections. Indeed, the MBB interconnection not only saves the silver consumption, but it also provides higher thermo-mechanical reliability for the solar PV modules compared to the CR and the LCR interconnections.

Table 16: Dimensions, high temperature crack specifications and number of cycles to creep-fatigue lifetime of the recommended PV module ribbon interconnection designs

Designs		**CR**				**LCR**			**MBB**		
Geometrical Parameters		**1st**	**2nd**	**3rd**	**4th**	**1st**	**2nd**	**3rd**	**1st**	**2nd**	**3rd**
Number of ribbons		5	5	3	5	5	5	5	15	15	15
Ribbon width (µm)		900	1000	1200	1000	1000	900	1000	291	276	276
Copper thickness (µm)		200	200	200	150	187	250	125	291	276	276
Solder thickness (µm)		20	20	20	20	20	20	20	20	20	15
Silver-pad thickness (µm)		40	40	40	40	40	40	40	20	20	20
Copper area (mm^2)		0.9	1	0.72	0.75	0.75	0.9	0.5	1	0.9	0.9
Crack initiation temp. (°C)		98	102	104	102	87	69.5	106	98	102	110
Crack growth rate (µm/°C)		0.35	0.45	0.6	1.82	0.5	0.58	1	0.1	0.19	0.25
Initial crack length at 150 °C (µm)		18	22	28	87	31.5	46.69	44	5	9	10
*Cracked Section (%)**		4.0	4.3	4.6	17.5	6.3	10.38	8.8	3.6	6.6	7.2
N_f (Cycle) *T: -40°C to 85°C*	*W.O. Crack*	3471	3334	3205	3481	3502	3475	3369	3954	4078	3644
	With Crack	3331	3190	3058	2873	3281	3114	3073	3813	3808	3380

* It is assumed that the crack is initiated in left and right sides of the IMC layer (as the symmetrical models are considered in the simulations), so, the crack length is assumed to be duplicated.

Table 17: Creep-fatigue life estimation of the solder joint for the selected ribbon interconnection.

Designs		**CR**	**LCR**	**MBB**
		1st	**1st**	**1st**
Creep-fatigue lifetime (Year)	*T: 10°C to 50°C*	27.3	26.9	31.2
	T: 0°C to 50°C	26.2	25.8	30.0
	T: 0°C to 60°C	13.2	13.0	15.1

7.6. Chapter Summary and Conclusion

This chapter compared the main FEM results for different the PV module ribbon interconnection designs used in this study, and then the best configurations are recommended to provide the highest thermo-mechanical reliability, but with less material consumption. Comparison of the effects of changing solder, silver, copper, IMC thickness and ribbon width changes on the reliability of the PV modules interconnections showed that there is a good agreement between the crack analysis results (from the XFEM simulation) and the results of creep-fatigue investigation of the solder joints for all PV modules interconnection designs. It is also shown that the location of the crack nucleation is same with the location of the maximum shear creep strain in the solder joints (found from the creep investigation) which is at the side of the IMC interface layers.

The results showed that for the CR and the LCR interconnections, using 5 ribbons with 900µm - 1000µm ribbon width, with 40µm silver-pads thickness and with 20µm solder thickness is recommended to provide over 25 years' life service for the solar PV module operating under thermal cycling condition with temperature ranging from 0°C to 50°C.

Also, it is shown that the MBB interconnection (with15 ribbons with 276µm ribbon diameter and with 20µm silver and solder thicknesses) provides 15% more fatigue life rather than the CR and the LCR interconnection designs. As a result, recommended configuration for the MBB interconnection could be the most reliable design to guarantee over 30 and 15 years' life service for the thermal failure of the solder joints in PV module interconnection operating under thermal cycling conditions with temperature ranging from 0°C to 50°C and 0°C to 60°C, respectively.

Chapter 8

8. Summary, Conclusion, Suggestions

8.1. Summary

This study concerned the investigation of the thermal failure of the solder joints in c-Si PV module interconnection, a key component of the PV module as its failure accounts for over 40% of known PV module failure. The thesis presented the method for determination of the optimum designs of PV module interconnections that gave improved thermo-mechanical reliability and that keeps the module efficiency high and material consumption low. Different PV module interconnection designs including the CR, the LCR and the MBB interconnections were investigated to determine the effect of changing dimensions of each design on the PV module interconnection reliability. The FEM simulation in ABAQUS 2019 was used to investigate the thermal failure of the solder joints in different PV module interconnection designs under two different thermal load conditions (namely: high temperature in lamination process, and thermal cycling). For this, the PV module interconnections were modelled using a scripted Python code launched in ABAQUS 2019, in which the main nonlinearities of the models such as temperature dependency of the materials and the presence of the brittle IMC interface layer at the border of the solder joints were considered. These investigations were implemented for over 350 cases of the three main PV module interconnection designs with different dimensions of the interconnections materials (namely: silver-pad, solder, copper thickness and ribbon width).

The XFEM technique was implemented to find the crack initiation temperature and the crack growth rate in solder joints subjected to the high temperature lamination process(up to 150 °C). Also, to investigate the creep-fatigue failure of the solder joints in different PV module interconnection designs operating under thermal cycling load (ranging from -40°C to 85°C), the number of cycles to failure were determined using the FEM simulations and Morrow Energy Density model; and then the creep-fatigue results were correlated with the Coffin–Manson–Arrhenius formulation to estimate the creep-fatigue lifetime of each design operating under different thermal cycling conditions (namely: from temperature ranges of 10°C to 50°C, 0°C to 50°C and 0°C to 60°C).

Finally, the effect of the initial cracks (due to the lamination process) was combined with the effect of creep-fatigue to determine the failure lifetime of the solder joint for different PV module interconnection designs. The methodology developed can be used for investigating the thermal-fatigue life of PV module interconnections subjected to hot/cold service conditions and for predicting the long-term reliability of the solar PV module based on the knowledge of initial state.

The main conclusions of the study are presented in Section 8.2, and the limitations of the research and the recommendations for future work are presented in Section 8.3.

8.2. Conclusions

To determine the optimum design and configuration of the PV module interconnection in terms of the thermo-mechanical reliability, the XFEM simulation was used to calculate the crack length, the crack initiation temperature and the crack growth rate in the solder joints subjected to the high temperature in the lamination process. In addition, for different PV module interconnection designs, the creep-fatigue lifetime of the solder joints is estimated to determine the most reliable designs. The XFEM results were consistent with the results of creep-fatigue investigation discussed in the following sub-sections:

8.2.1. Crack Location and Propagation Direction

For all studied PV module interconnection designs subjected to the lamination process, the XFEM simulations showed that the crack location is at side of the IMC interface layers of solder joint boundaries (in contact with the silver-pad and the copper ribbon); and direction of the crack propagation is in the shear direction. It is also found that when the crack nucleation location is in the IMC-Silver layer, the crack growth rate is significantly higher, which increases the crack related failures and adversely affects the reliability of the PV module interconnection.

The creep investigation of the solder joints in PV module interconnections also showed that the mentioned location of crack initiation exhibits the maximum shear creep strain in the solder joints which means that the fatigue damage initiates at this location; and the results of the XFEM simulation and creep-fatigue investigations are in a very good agreement.

8.2.2. Effect of Changing Dimensions

Comparison of the results of XFEM and creep-fatigue investigation for the effects of changing solder, silver, copper thicknesses and ribbon width of the PV modules interconnections on the thermal failure of the solder joints and on the associated thermo-mechanical reliability showed a very good agreement between them.

The results showed that increasing the CR and the LCR interconnection width leads to an increase in the crack initiation temperature for widths up to 1200µm; but the crack initiation temperature remains relatively constant for increases beyond the 1200µm limit. Based on the analysis of the results for both the crack initiation temperature and the crack growth rate for the ribbon interconnection geometries investigated, and consequently the use of ribbon interconnects widths of circa 900µm to 1000µm (for cell tabbing using 5 ribbons) is recommended. These recommended ribbon interconnects widths also introduced similar trend for the number of cycles to creep-fatigue failure (N_f) in the PV module solder joint interconnections.

The results also showed that increasing the copper thickness in the CR interconnections leads to a decrease in the crack initiation temperature; and also for interconnection thickness between 150µm to 200µm, there is a significant reduction in the crack growth rate, with the 200µm copper thickness experiencing the lowest crack growth rate. The summation of the effects of copper thickness changes on the crack initiation temperature and the crack growth rate for the CR interconnections shows that there is a minor increase in the crack length when the copper thickness increases. These results were consistent with the calculated N_f, as thicker copper experienced a marginal decrease of N_f. In addition, the results of XFEM simulation and creep-fatigue investigation for the LCR interconnection also showed that changing the copper thickness had a marginal effect on the thermal failure of the solder joints. However, for the MBB interconnection, the results showed that increasing the copper diameter leads to a marginal reduction in the N_f, and the maximum N_f was found for the MBB interconnection with the 276µm copper diameter.

The XFEM results showed that the crack initiation temperature and the crack growth rate decrease with increasing silver-pad thickness for the LCR and the CR interconnections. In summary, our results showed that in terms the N_f, the 40µm silver-pads thickness is recommended for the LCR and the CR interconnections to provide more reliability. However, the results for the MBB interconnection design shows that there is no significant effect of the silver-pad thickness on the N_f, and the 20µm silver-pads thickness is recommended for the MBB interconnection due to less silver material consumption.

The XFEM results showed that the recommended copper thickness for all interconnection designs evaluated in this study, is the 20µm solder thickness as this gives the highest crack initiation temperature in the solder joint. In addition, the results showed that the 20µm solder thickness exhibits a lower crack growth rate in comparison with the growth rate for the thicker solders. The results of creep-fatigue investigation showed that increasing the solder thickness leads to a marginal increase in the N_f. For this reason, the 20µm solder thickness is recommended solder thickness for all ribbon interconnection designs as this results in the high N_f but smaller solder material consumption.

8.2.3. Effect of Non-Homogeneous Solder Coating on cracks in the MBB Interconnections

The two main parameters of non-homogeneity (out of centre value and direction), were considered in investigation of the effect of geometrical parameters (including IMC layers thickness and solder joint height) on the crack initiation in the solder joints in MBB interconnections. The results showed that the downward vertical direction of out of centre positioning of copper in the solder coating leads to the most reduction in crack initiation temperature (up to 21%). The results also showed that by increasing the amount of molten solder/solder thickness, the micro-crack initiation takes place at a lower temperature. The results also show that at high solder thickness the micro-crack initiation temperature is less affected by non-homogeneity.

8.2.4. Creep-Fatigue Life Estimation for PV Module Interconnections

The exponent factor used for the Coffin–Manson–Arrhenius approach to estimate the creep-fatigue life of the PV module interconnections was determined to be -1.8; and this generic exponent factor value was then used to determine the solder joint's creep-fatigue life under thermal cycling operating conditions. The results show that for all cases studied, the maximum temperature of the cycling load has a significant impact on the creep-fatigue lifetime; for example, by increasing the maximum temperature from 50°C to 60°C, the creep-fatigue lifetime decreases by 50%. Similarly, the results show that the minimum temperature of the cycling load has no significant effect on the creep-fatigue lifetime (~5%).

8.2.5. Recommended Configurations for the PV Module Interconnection Designs

To provide high thermo-mechanical reliability of the PV module interconnection, the optimum configurations of the different designs are found by comparing their creep-fatigue lifetime correlated with the XFEM results. It was found that the MBB interconnection has higher thermal creep-fatigue age compared to the CR and the LCR interconnections (up to 15%). The results also showed that the MBB interconnection with 15 ribbons of 20µm solder thickness, with 20µm silver-pad thickness and with copper diameter of 276µm ($0.9mm^2$ cross-section area of the copper) has N_f of 3808 cycles which is higher than N_f determined for the other PV module interconnection designs evaluated in this study. This configuration is recommended as the optimum design of the PV module interconnection, and it can guarantee service life of 30 years and 15 years for the solder joint operating under thermal cycling conditions with temperature ranging from 0°C to 50°C and 0°C to 60°C, respectively. Another benefit of the MBB interconnection is that its use results in lower material consumption and lower manufacturing costs.

Furthermore, the results showed that the best configuration for the CR interconnection is the 5 ribbons with 900μm ribbon width, with 200μm copper thickness (0.9mm^2 cross-section area of the copper), with 20μm solder thickness and with 40μm silver-pad thickness. This configuration exhibited a 4.0% cracked section (due to the lamination process), and it was reliable for 3331 thermal cycles with temperature ranging from -40°C to 85°C (26.2 years; temperature ranging from 0°C to 50°C). The results also showed that the LCR interconnection using 5 ribbons with 1000μm ribbon width, with 187μm copper thickness (0.75mm^2 total cross-section area of the copper), with 20μm solder thickness and with 40μm silver-pad thickness is the optimum configuration of this interconnection design. This recommended configuration can guarantee 25.8 years for operating under thermal cycling condition with temperature ranging from 0°C to 50°C.

The findings of the PV module interconnections research can be used to evaluate potential design adjustments and to assist design for reliability validation of various configurations in order to enhance the long-term reliability of PV module systems.

8.3. Main Contribution to Knowledge

For the first time, this research used the XFEM technique (previously used for crack analysis in structural materials) to determine the crack initiation temperature, crack location, crack direction and growth rate in the solder joint of PV module interconnection. Furthermore, the number of cycles to creep-fatigue failure for all PV module interconnection designs studied in this research was determined using the Morrow Energy Density lifetime model (with considering the standard thermal cycling condition based on the IEC 61215-2:2016); and then the Coffin–Manson–Arrhenius lifetime model is used as a handy formulation that can be applied easily to determine the solder joint's creep-fatigue life under different lifecycles of the module. In addition, the research combines the numerical results of XFEM and creep fatigue analysis to determine the thermal failure lifetime of PV Module interconnection solder joints under high temperature lamination process and thermal cycling to consider both thermal loading scenarios. The research defined the optimised PV module interconnection configurations for CR, LCR and MBB interconnection designs and the results show that the MBB interconnection design provides higher reliability (up to 15%) compared to other designs. The research also determined a new generic exponent factor (-1.8) for the Coffin–Manson–Arrhenius lifetime model to estimate the creep-fatigue lifetime of PV module interconnections under different thermal cycling conditions. This analytical model is developed an it facilitates the fast thermal cycling estimation for PV module interconnection reliability.

The results of this research can be used by PV module manufacturers for evaluating potential design changes and to facilitate design for reliability validation of different configurations to improve the long-term PV module system reliability. Also, the results of the study will also be useful for researchers in evaluating the impact of the solder region boundaries on solar PV module reliability and in developing design-for-reliability guidelines.

8.4. Limitations of Research and Recommendations for Future Work

Despite developments and new knowledge generated in this thesis, there remains significant scope for improvement of PV module designs. The limitations of the research and the recommendations for future work are presented in the sub-sections below.

8.4.1. Limitations of Research

The limitations of this research are as follows:

1. This study used advanced finite element modelling with consideration of the nonlinearities such as temperature dependent and elastic-plastic behaviour of materials. The investigations of this study was limited to simulate the PV module interconnection on the one silicon cell to find the thermal failure of PV module solder joint interconnections.. Although the results from the 2D simulation is checked with the a results from 3D simulation for a case study and there was good agreement between the results, however, this work faced a limitation for 3D modelling of the PV module with considering all silicon cells and the ribbon interconnection bend between the cells. This is because 3D modelling of the PV module is more computationally demanding, and it requires larger meshes in the simulations, which in turn will limit the scope of the parametric study. For this reason, 2D simulations of the PV module interconnection are used in order to increase the computational solution speed
2. This study used the XFEM technique (to find the crack initiation and propagation during the lamination process) and the nonlinear FEM approach (to estimate the creep-fatigue lifetime under thermal cycling conditions) separately, for the investigation of the thermal failure of PV module solder joint interconnections. Ideally the methodology should combine the XFEM technique and the creep failure investigation is one study to facilitate determination of the optimum PV module interconnection design. Unfortunately, ABAQUS software cannot still use both approaches in one simulation study, since the XFEM technique does not provide the features for modelling the certain nonlinear failure mechanism such as creep-fatigue.

8.4.2. Recommendations for Future Work

The following are recommendations for future work:

1. Although the numerical approach used in this study can produce reasonable and accurate answers to the questions regarding the failure mechanisms of solder joints in solar PV interconnections, further experimental work is required to verify the FEM simulation results. The availability of the experimental verification results will facilitate improved damage-lifetime correlation based on the use of 2D and 3D model results.
2. Investigation of the effect of micro-scale defects on the reliability of the PV module (this should include the voids in the solder joint due to evaporation of solvents and additives; in particular, this should also include study of the effect of voids on crack initiation in the PV module solder joint interconnections).

References

ABAQUS, I. (2019) ABAQUS User’s and Theory Manuals: Version 6.19, ABAQUS Inc., Providence Rhode Island, RI, USA.

Adani Green Energy Ltd. (2019) 648 MW, Kamuthi, Tamil Nadu. [Online] Available at: https://www.adanigreenenergy.com/solar-power/Kamuthi

Afriyie Nyarko, F. K., Takyi, G. and Effah, F. B. (2021) Study on Creep Damage in Sn60Pb40 and Sn3.8Ag0.7Cu (Lead-Free) Solders in c-Si Solar PV Cell Interconnections under In-Situ Thermal Cycling in Ghana, Crystals, 11(4).

Afriyue Nyarko, F. k. & Takyi, G. (2021) Life prediction in c_Si solar cell interconnections under in-situ thermal cycling in Kumasi in Ghana. Soldering & Surface Mount Technology, 33(4).

Akay, H. U., Liu, Y. and Rassaian, M. (2003) Simplification of finite element models for thermal fatigue life prediction of PBGA packages, J. Electron. Packag., 125(3), pp. 347–353.

Aly, S. P., Ahzi, S., Barth, N. and Abdallah, A. (2020) Numerical analysis of the reliability of photovoltaic modules based on the fatigue life of the copper interconnects, Solar Energy, Elsevier, 212, pp. 152–168.

Amalu, E. H. and Ekere, N. N. (2016) Modelling evaluation of Garofalo-Arrhenius creep relation for lead-free solder joints in surface mount electronic component assemblies, Journal of Manufacturing Systems, Elsevier, 39, pp. 9–23.

Amalu, E. H., Ekere, N. N. and Aminu, G. (2011) Effects of inter-metallic compound on high temperature reliability of flip chip interconnects for fine pitch applications, In 3rd IEEE International Conference on Adaptive Science and Technology (ICAST 2011), IEEE, pp. 208–213.

Andersson, C., Sun, P. and Liu, J. (2006) Low cycle fatigue of Sn-based lead-free solder joints and the analysis of fatigue life prediction uncertainty, In Conference on High Density Microsystem Design and Packaging and Component Failure Analysis, 2006. HDP’06., IEEE, pp. 272–279.

AZoM. (2001) Silver - Applications and Properties of Silver. [Online] Available at: https://www.azom.com/properties.aspx?ArticleID=600

AZoM. (2005) Aluminium-Specifications, Properties, Classifications and Classes. [Online] Available at: https://www.azom.com/article.aspx?ArticleID=2863

Baber, F. and Guven, I. (2017) Solder joint fatigue life prediction using peridynamic approach, Microelectronics Reliability, Elsevier, 79, pp. 20–31.

Basaran, C., Cartwright, A. and Zhao, Y. (2001) Experimental damage mechanics of microelectronics solder joints under concurrent vibration and thermal loading, International Journal of Damage Mechanics, Sage Publications Sage CA: Thousand Oaks, CA, 10(2), pp. 153–170.

Belytschko, T. and Black, T. (1999) Elastic crack growth in finite elements with minimal remeshing, International journal for numerical methods in engineering, Wiley Online Library, 45(5), pp. 601–620.

Belytschko, T., Gracie, R. and Ventura, G. (2009) A review of extended/generalized finite element methods for material modeling, Modelling and Simulation in Materials Science and Engineering, 17(4).

Benabou, L., Etgens, V. and Tao, Q. B. (2016) Finite element analysis of the effect of process-induced voids on the fatigue lifetime of a lead-free solder joint under thermal cycling, Microelectronics Reliability, Elsevier, 65, pp. 243–254.

Bidram, A., Davoudi, A. and Balog, R. S. (2012) Control and circuit techniques to mitigate partial shading effects in photovoltaic arrays, IEEE Journal of Photovoltaics, IEEE, 2(4), pp. 532–546.

Birol. (2020) World Energy Outlook 2020-Flagship report . Retrieved from International Energy Agency (IEA).

Braun, S., Hahn, G., Nissler, R., Pönisch, C. and Habermann, D. (2013) The multi-busbar design: an overview, Energy Procedia, Elsevier, 43, pp. 86–92.

Braun, S., Micard, G. and Hahn, G. (2012) Solar cell improvement by using a multi busbar design as front electrode, Energy Procedia, Elsevier, 27, pp. 227–233.

Cambridge University Engineering Department. (2003) Materials Data Book. Cambridge University Engineering Department Data Books.

Campeau, Z. (2013) SunPower® Module Degradation Rate, SunPower Corporation.

Che, F. X. and Pang, J. H. L. (2004) Thermal fatigue reliability analysis for PBGA with Sn-3.8 Ag-0.7 Cu solder joints, In Proceedings of 6th Electronics Packaging Technology Conference (EPTC 2004)(IEEE Cat. No. 04EX971), IEEE, pp. 787–792.

Cheng, S., Huang, C.-M. and Pecht, M. (2017a) A review of lead-free solders for electronics applications, Microelectronics Reliability, Elsevier, 75, pp. 77–95.

Cheng, S., Huang, C.-M. and Pecht, M. (2017b) A review of lead-free solders for electronics applications, Microelectronics Reliability, Elsevier, 75, pp. 77–95.

Chen, Y., Jin, Y. and Kang, R. (2017) Coupling damage and reliability modeling for creep and fatigue of solder joint, Microelectronics Reliability, Elsevier, 75, pp. 233–238.

Chen, Z., Zhang, Z., Dong, F., Liu, S. and Liu, L. (2021) A Hybrid Finite Element Modeling: Artificial Neural Network Approach for Predicting Solder Joint Fatigue Life in Wafer-Level Chip Scale Packages, Journal of Electronic Packaging, American Society of Mechanical Engineers, 143(1), p. 011001.

Cho, Y., Jang, J. and Jang, G. (2018) Sensitivity analysis on the fatigue life of solid state drive solder joints by the finite element method and Monte Carlo simulation, Microsystem Technologies, Springer, 24(11), pp. 4669–4676.

Chung, I., young Son, H., Oh, H., Baek, U., Yoon, N., Lee, W., Cho, E.-C. and Moon, I.-S. (2013) Light Capturing Film on interconnect ribbon for current gain of crystalline silicon PV modules, In 2013 IEEE 39th Photovoltaic Specialists Conference (PVSC), IEEE, pp. 1478–1480.

Darveaux, R. (2002) Effect of simulation methodology on solder joint crack growth correlation and fatigue life prediction, J. Electron. Packag., 124(3), pp. 147–154.

Deng, X., Sidhu, R. S., Johnson, P. and Chawla, N. (2005) Influence of reflow and thermal aging on the shear strength and fracture behavior of Sn-3.5 Ag solder/Cu joints, Metallurgical and Materials Transactions A, Springer, 36(1), pp. 55–64.

Depiver, J. A., Mallik, S. and Amalu, E. H. (2019) Creep response of various solders used in soldering ball grid array (BGA) on printed circuit board (PCB), Newsroom Limited.

Depiver, J. a, Mallik, S. and Harmanto, D. (2021) Solder joint failures under thermo-mechanical loading conditions–A review, Advances in Materials and Processing Technologies, Taylor & Francis, 7(1), pp. 1–26.

Desa, M. K. M., Sapeai, S., Azhari, A. W., Sopian, K., Sulaiman, M. Y., Amin, N. and Zaidi, S. H. (2016) Silicon back contact solar cell configuration: A pathway towards higher efficiency, Renewable and sustainable energy reviews, Elsevier, 60, pp. 1516–1532.

Diwania, S., Agrawal, S., Siddiqui, A. S. and Singh, S. (2020) Photovoltaic–thermal (PV/T) technology: a comprehensive review on applications and its advancement, International Journal of Energy and Environmental Engineering, Springer, 11(1), pp. 33–54.

Domínguez, C., Puertas, G., Sanchidrián, A., Cascón, R., Martínez, M., Sánchez, D., Noriega, P., Jost, N. and Antón, I. (2018) Assessing the suitability of metal-wrap-through solar cells for low-concentration PV systems, In AIP Conference Proceedings, AIP Publishing LLC, p. 040002.

Dricus. (2011) Anti Reflective Coating: usage for solar panels. [Online] Available at: (https://sinovoltaics.com/learning-center/solar-cells/anti-reflective-coating-for-solar-panels/

DuPont™. (2014) DuPont™ Tedlar® Polyvinyl Fluoride (PVF) Films. [Online] Available at: https://www.dupont.com/content/dam/dupont/products-and-services/membranes-and-films/pvf-films/documents/DEC_Tedlar_GeneralProperties.pdf

Du, Z. (2009) eXtended Finite Element Method (XFEM) in Abaqus. [Online] Available at: http://www.simulia.com/download/rum11/UK/Advanced-XFEM-Analysis.pdf

Echizenya, D., Sakamoto, H. and Sasaki, K. (2011) Effect of mechanical surface damage on Silicon wafer strength, Procedia Engineering, Elsevier, 10, pp. 1440–1445.

Eitner, U., Eberlein, D. and Tranitz, M. (2012) Interconnector-based module technology for thin MWT cells, Proc. 27th EU PVSEC, pp. 3461–3464.

Faes, A., Despeisse, M., Levrat, J., Champliaud, J., Badel, N., Kiaee, M., Söderström, T., Yao, Y., Grischke, R. and Gragert, M. (2014) SmartWire solar cell interconnection technology, In Proc. 29th Eur. Photovoltaic Sol. Energy Conf, pp. 2555–2561.

Farukh, F., Zhao, L., Jiang, R., Reed, P., Proprentner, D. and Shollock, B. (2015) Fatigue crack growth in a nickel-based superalloy at elevated temperature - experimental studies, viscoplasticity modelling and XFEM predictions, Mechanics of Advanced Materials and Modern Processes, 1(1), p. 2, [online] Available from: https://doi.org/10.1186/s40759-015-0003-4.

Fei, H., Yazzie, K., Chawla, N. and Jiang, H. (2012) Modeling fracture of Sn-rich (Pb-free) solder joints under mechanical shock conditions, Journal of electronic materials, Springer, 41(8), pp. 2089–2099.

Ferrara, C. and Philipp, D. (2012) Why do PV modules fail?, Energy Procedia, Elsevier, 15, pp. 379–387.

Fields, R. (2002) Physical and mechanical properties of intermetallic compounds commonly found in solder joints, http://www. metallurgy. nist. gov/mechanical_properties/solder_paper. html.

Fries, TP. (2018) Extended Finite Element Methods (XFEM), In: Altenbach, H., Öchsner, A. (eds) Encyclopedia of Continuum Mechanics. Springer, Berlin, Heidelberg. https://doi.org/10.1007/978-3-662-53605-6_17-1

Geipel, T., Meinert, M., Kraft, A. and Eitner, U. (2018) Optimization of electrically conductive adhesive bonds in photovoltaic modules, IEEE Journal of Photovoltaics, IEEE, 8(4), pp. 1074–1081.

Guyenot, M., Peter, E., Zerrer, P., Kraemer, F. and Wiese, S. (2011) Enhancing the lifetime prediction methodology for photovoltaic modules based on electronic packaging experience, In 2011 12th Intl. Conf. on Thermal, Mechanical & Multi-Physics Simulation and Experiments in Microelectronics and Microsystems, IEEE, pp. 1–4.

Halouani, A., Cherouat, A., Miladi Chaabane, M. and Haddar, M. (2020) Modeling and experimental investigation of damage initiation and propagation of LQFP package under thermal cycle, Microsystem Technologies, Springer, 26, pp. 3011–3021.

Han, C. and Han, B. (2014) Board level reliability analysis of chip resistor assemblies under thermal cycling: A comparison study between SnPb and SnAgCu, Journal of Mechanical Science and Technology, Springer, 28(3), pp. 879–886.

Han, H., Dong, X., Lai, H., Yan, H., Zhang, K., Liu, J., Verlinden, P. J., Liang, Z. and Shen, H. (2018) Analysis of the degradation of monocrystalline silicon photovoltaic modules after long-term exposure for 18 Years in a hot–humid climate in China, IEEE Journal of Photovoltaics, IEEE, 8(3), pp. 806–812.

Hasselbrink, E., Anderson, M., Defreitas, Z., Mikofski, M., Shen, Y.-C., Caldwell, S., Terao, A., Kavulak, D., Campeau, Z. and DeGraaff, D. (2013) Validation of the PVLife model using 3 million module-years of live site data, In 2013 IEEE 39th Photovoltaic Specialists Conference (PVSC), IEEE, pp. 7–12.

Heimann, M., Bakowskie, R., Köhler, M., Hirsch, J., Junghänel, M., Hussack, A. and Sachert, S. (2014) Investigations of different soldering failure modes and their impact on module reliability, Energy Procedia, Elsevier, 55, pp. 456–463.

Held, M., Jacob, P., Nicoletti, G., Scacco, P. and Poech, M.-H. (1997) Fast power cycling test of IGBT modules in traction application, In Proceedings of second international conference on power electronics and drive systems, IEEE, pp. 425–430.

Herrmann, W. (2010) How temperature cycling degrades photovoltaic-module performance, International Society Advancing an Interdisciplinary Approach to the Science and Application of Light (SPIE).

Holst, H., Schulte-Huxel, H., Winter, M., Blankemeyer, S., Witteck, R., Vogt, M. R., Booz, T., Distelrath, F., Köntges, M. and Bothe, K. (2016) Increased light harvesting by structured cell interconnection ribbons: an optical ray tracing study using a realistic daylight model, Energy Procedia, Elsevier, 92, pp. 505–514.

Honsberg, C., Bowden, S. (2018) Degradation and Failure Modes. [Online] Available at: https://www.pveducation.org/pvcdrom/modules/degradation-and-failure-modes

Hsiao, P.-C., Shen, X., Wang, Z., Song, N., Li, Y., Ouyang, Z., Zhu, C., Lv, J., Shen, C., Chen, C., Chen, G. and Lennon, A. (2020) Balanced contact method: Reduction of thermomechanical stress in silicon solar cells induced by interconnection, Solar Energy Materials and Solar Cells, 215, p. 110667, [online] Available from: https://www.sciencedirect.com/science/article/pii/S0927024820302695.

Hsieh, M. and Tzeng, S. (2014) Solder joint fatigue life prediction in large size and low cost wafer-level chip scale packages, In 2014 15th International Conference on Electronic Packaging Technology, pp. 496–501.

Hund, T. D. and Burchett, S. N. (1991) Solder fatigue reduction in point focus photovoltaic concentrator modules, Sandia National Labs., Albuquerque, NM (United States).

IEA (2019) Renewables 2019, IEA, Paris. [Online], available at: https://www.iea.org/reports/renewables-2019

IEA (2021) Solar PV, IEA, Paris. [Online], available at: https://www.iea.org/reports/solar-pv

IEC 61215 (2016) Terrestrial Photovoltaic (PV) Modules—Design Qualification and Type Approval, International Electrotechnical Commission, Geneva.

IRENA (2019) Future of Solar Photovoltaic: Deployment, investment, technology, grid integration and socio-economic aspects, Abu Dhabi, International Renewable Energy Agency (IRENA).

IRENA (2020) Renewables 2020 Global Status Report: A comprehensive annual overview of the state of renewable energy, Paris, International Renewable Energy Agency (IRENA).

Ishii, T. and Masuda, A. (2017) Annual degradation rates of recent crystalline silicon photovoltaic modules, Progress in Photovoltaics: Research and Applications, Wiley Online Library, 25(12), pp. 953–967.

Itoh, U., Yoshida, M., Tokuhisa, H., Takeuchi, K. and Takemura, Y. (2014) Solder joint failure modes in the conventional crystalline Si module, Energy Procedia, Elsevier, 55, pp. 464–468.

JEDEC, S. (2009) JESD22-A104D, Temperature cycling.

Jeong, J.-S., Park, N. and Han, C. (2012) Field failure mechanism study of solder interconnection for crystalline silicon photovoltaic module, Microelectronics Reliability, Elsevier, 52(9–10), pp. 2326–2330.

Jiang, N., Clum, J. A., Chromik, R. R. and Cotts, E. J. (1997) Thermal expansion of several Sn-based intermetallic compounds, Scripta Materialia, 37(12), pp. 1851–1854.

Jiang, N., Ebadi, A. G., Kishore, K. H., Yousif, Q. A. and Salmani, M. (2019) Thermomechanical reliability assessment of solder joints in a photovoltaic module operated in a hot climate, IEEE Transactions on Components, Packaging and Manufacturing Technology, IEEE, 10(1), pp. 160–167.

Jing, X., Lee, U.-H., Xu, C., Niu, Z., Hao, H., Bae, J.-Y., Won, J. and Zhang, W. (2015) Effect of pre-CMP annealing on TSV pumping in thermal budget and reliability test, In 2015 IEEE 22nd International Symposium on the Physical and Failure Analysis of Integrated Circuits, IEEE, pp. 45–47.

Jordan, D. C., Silverman, T. J., Sekulic, B. and Kurtz, S. R. (2017) PV degradation curves: non-linearities and failure modes, Progress in Photovoltaics: Research and Applications, John Wiley & Sons, Ltd, 25(7), pp. 583–591, [online] Available from: https://doi.org/10.1002/pip.2835.

Jung, T., Song, H., Ahn, H. and Kang, G. (2014) A mathematical model for cell-to-module conversion considering mismatching solar cells and the resistance of the interconnection ribbon, Solar energy, Elsevier, 103, pp. 253–262.

Kelly, G. and Mahesh, S. (2017) Standards in the solar photovoltaic value chain in relation to international trade, International Centre for Trade and Sustainable Development (ICTSD), Geneva, Switzerland.

Khoei, A. R. and Vahab, M. (2014) A numerical contact algorithm in saturated porous media with the extended finite element method, Computational Mechanics, Springer, 54(5), pp. 1089–1110.

Kim, J.-H., Park, J., Kim, D. and Park, N. (2014) Study on mitigation method of solder corrosion for crystalline silicon photovoltaic modules, International Journal of Photoenergy, Hindawi, 2014.

Knecht, S. and Fox, L. R. (1990) Constitutive relation and creep-fatigue life model for eutectic tin-lead solder, IEEE Transactions on Components, Hybrids, and Manufacturing Technology, IEEE, 13(2), pp. 424–433.

Köntges, M., Kajari-Schröder, S., Kunze, I. and Jahn, U. (2011) Crack statistic of crystalline silicon photovoltaic modules, In 26th European photovoltaic solar energy conference and exhibition, pp. 3290–3294.

Kumar, S. and Gupta, R. (2019) Thermo-mechanical degradation at finger-solder interface in a crystalline silicon photovoltaic module under thermal fatigue conditions, In 2019 IEEE 46th Photovoltaic Specialists Conference (PVSC), IEEE, pp. 118–121.

Lau, C.-S., Abdullah, M. Z., Mujeebu, M. A. and Yusop, N. M. D. (2014a) Finite element analysis on the effect of solder joint geometry for the reliability of ball grid array assembly with flexible and rigid PCBs, Journal of Engineering Science and Technology, 9(1), pp. 47–63.

Lau, C.-S., Abdullah, M. Z., Mujeebu, M. A. and Yusop, N. M. D. (2014b) Finite element analysis on the effect of solder joint geometry for the reliability of ball grid array assembly with flexible and rigid PCBs, Journal of Engineering Science and Technology, 9(1), pp. 47–63.

Lau, J. H., Pan, S. H. and Chang, C. (2000) Nonlinear fracture mechanics analysis of wafer level chip scale package solder joints with cracks, In PROCEEDINGS-SPIE THE INTERNATIONAL SOCIETY FOR OPTICAL ENGINEERING, International Society for Optical Engineering; 1999, pp. 857–865.

Lee, T. D. and Ebong, A. U. (2017) A review of thin film solar cell technologies and challenges, Renewable and Sustainable Energy Reviews, Elsevier, 70, pp. 1286–1297.

Lee, W. W., Nguyen, L. T. and Selvaduray, G. S. (2000) Solder joint fatigue models: review and applicability to chip scale packages, Microelectronics reliability, Elsevier, 40(2), pp. 231–244.

Lee, Y. C. and Chiang, K. N. (2019) Reliability Assessment of WLCSP using Energy Based Model with Inelastic Strain Energy Density, In 2019 International Conference on Electronics Packaging (ICEP), IEEE, pp. 329–332.

Levi, D. H., Green, M. A., Hishikawa, Y., Dunlop, E. D., Hohl-Ebinger, J. and Ho-Baillie, A. W. Y. (2017) Solar cell efficiency tables (version 51), Progress in Photovoltaics, National Renewable Energy Lab.(NREL), Golden, CO (United States), 26(NREL/JA-5J00-70757).

Li, J., Karppinen, J., Laurila, T. and Kivilahti, J. K. (2009) Reliability of Lead-Free Solder Interconnections in Thermal and Power Cycling Tests, IEEE Transactions on Components and Packaging Technologies, 32(2), pp. 302–308.

Liu, X., Sooklal, V. K., Verges, M. A. and Larson, M. C. (2006) Experimental study and life prediction on high cycle vibration fatigue in BGA packages, Microelectronics Reliability, Elsevier, 46(7), pp. 1128–1138.

Li, X., Sun, R. and Wang, Y. (2017) A review of typical thermal fatigue failure models for solder joints of electronic components, In IOP Conference Series: Materials Science and Engineering, IOP Publishing, p. 012103.

Ma, H. (2009) Constitutive models of creep for lead-free solders, Journal of Materials Science, Springer, 44(14), pp. 3841–3851.

McCluskey, F. P. (2010) Reliability modeling for photovoltaic modules, In NREL Photovoltaic Module Reliability Workshop, Denver, Colorado.[Accessed 4 December 2012] Available at:< http://www1. eere. energy. gov/solar/pdfs/pvrw2010_mccluskey. pdf.

Mittag, M., Beinert, A. J., Rendler, L. C., Ebert, M. and Eitner, U. (2015a) Triangular ribbons for improved module efficiency, In 32nd EU PVSEC.

Mittag, M., Beinert, A. J., Rendler, L. C., Ebert, M. and Eitner, U. (2015b) Triangular ribbons for improved module efficiency, In 32nd EU PVSEC.

Moës, N., Dolbow, J. and Belytschko, T. (1999) A finite element method for crack growth without remeshing, International journal for numerical methods in engineering, Wiley Online Library, 46(1), pp. 131–150.

Mohammadi, S. (2008) Extended finite element method: for fracture analysis of structures, John Wiley & Sons.

Motalab, M., Mustafa, M., Suhling, J. C., Zhang, J., Evans, J., Bozack, M. J. and Lall, P. (2013) Thermal cycling reliability predictions for PBGA assemblies that include aging effects, In International Electronic Packaging Technical Conference and Exhibition, American Society of Mechanical Engineers, p. V001T05A008.

Muehleisen, W., Neumaier, L., Hirschl, C., Maier, T., Schwark, M., Seufzer, S., Battistutti, R., Pedevilla, M., Scheurer, J. and Lorenz, R. (2016) Comparison of output power for solar cells with standard and structured ribbons, EPJ Photovoltaics, EDP Sciences, 7, p. 70701.

Nyarko, F. K. A. and Takyi, G. (2021) Life prediction in c-Si solar cell interconnections under in-situ thermal cycling in Kumasi in Ghana, Soldering & Surface Mount Technology, Emerald Publishing Limited, 33(4), pp. 215–223, [online] Available from: https://doi.org/10.1108/SSMT-10-2020-0045.

Ogbomo, O. O., Amalu, E. H., Ekere, N. N. and Olagbegi, P. O. (2017) A review of photovoltaic module technologies for increased performance in tropical climate, Renewable and Sustainable Energy Reviews, Elsevier, 75, pp. 1225–1238.

Ogbomo, O. O., Amalu, E. H., Ekere, N. N. and Olagbegi, P. O. (2018) Effect of operating temperature on degradation of solder joints in crystalline silicon photovoltaic modules for improved reliability in hot climates, Solar Energy, Elsevier, 170, pp. 682–693.

Osborne, M. (2018) Henkel's novel electrically conductive adhesive is designed for next-gen solar device assembly. [Online] Available at: https://www.pv-tech.org/products/henkels-novel-electrically-conductive-adhesive-is-designed-for-next-gen-sol [Accessed 21 May 2018].

Osmundsen, T. (2014) IEA and Solar PV: Two Worlds Apart, Norwegian Climate Foundation Report.

Owen-Bellini, M., Zhu, J., Betts, T. and Gottschalg, R. (2017) Thermo-mechanical stresses of silicon photovoltaic modules, Loughborough University.

Pander, M., Dietrich, S., Schulze, S.-H., Eitner, U. and Ebert, M. (2011) Thermo-mechanical assessment of solar cell displacement with respect to the viscoelastic behaviour of the encapsulant, In 2011 12th Intl. Conf. on Thermal, Mechanical & Multi-Physics Simulation and Experiments in Microelectronics and Microsystems, IEEE, pp. 1–6.

Pander, M., Schulze, S.-H. and Ebert, M. (2014) Mechanical modeling of electrically conductive adhesives for photovoltaic applications, In Proceedings of the 29th European Photovoltaic Solar Energy Conference and Exhibition, p. 3399.

Pareek, S., Chaturvedi, N. and Dahiya, R. (2017) Optimal interconnections to address partial shading losses in solar photovoltaic arrays, Solar Energy, Elsevier, 155, pp. 537–551.

Park, N., Han, C., Jeong, J. and Kim, D. (2013) Lifetime prediction model of thermal fatigue stress on crystalline silicon photovoltaic module, In 2013 IEEE 39th Photovoltaic Specialists Conference (PVSC), IEEE, pp. 1575–1578.

Pecht, M. (1993) Soldering processes and equipment, John Wiley & Sons.

Ramachandran, V., Wu, K. C. and Chiang, K. N. (2018) Overview Study of Solder Joint Reliablity due to Creep Deformation, Journal of Mechanics, 34(5).

Qi, W., Ni, Z., Ren, F., Zhao, J. and Wang, A. (2011), Research on power loss of solar cell modules, Photovoltaics International (12).

Ramaprabha, R. and Mathur, B. L. (2012) A comprehensive review and analysis of solar photovoltaic array configurations under partial shaded conditions, International Journal of Photoenergy, Hindawi, 2012.

Rashedi, A. and Khanam, T. (2020) Life cycle assessment of most widely adopted solar photovoltaic energy technologies by mid-point and end-point indicators of ReCiPe method, Environmental Science and Pollution Research, 27(23), pp. 29075–29090, [online] Available from: https://doi.org/10.1007/s11356-020-09194-1.

Rendler, L. C., Kraft, A., Ebert, C., Eitner, U. and Wiese, S. (2016) Mechanical stress in solar cells with multi busbar interconnection—Parameter study by FEM simulation, In 2016 17th International Conference on Thermal, Mechanical and Multi-Physics Simulation and Experiments in Microelectronics and Microsystems (EuroSimE), IEEE, pp. 1–5.

Rendler, L. C., Walter, J., Goldenberg, S., Beinert, A. J., Wiese, S. and Eitner, U. (2018) Mechanical and electrical properties of wave-shaped wires for low-stress interconnection of solar cells, Solar Energy Materials and Solar Cells, Elsevier, 176, pp. 204–211.

Rendler, L. C., Walter, J., Kraft, A., Ebert, C., Wiese, S. and Eitner, U. (2017) Ultra-soft wires for direct soldering on finger grids of solar cells, Energy Procedia, Elsevier, 124, pp. 478–483.

Rowell, M. W. and McGehee, M. D. (2011) Transparent electrode requirements for thin film solar cell modules, Energy & Environmental Science, Royal Society of Chemistry, 4(1), pp. 131–134.

Sachs, E. M., Serdy, J., Gabor, A. M., van Mierlo, F. and Booz, T. (2009) Light-capturing interconnect wire for 2% module power gain, Proc. 24th EU PVSEC, Hamburg, Germany, pp. 3222–3225.

Samavatian, V., Iman-Eini, H., Avenas, Y. and Samavatian, M. (2020) Effects of creep failure mechanisms on thermomechanical reliability of solder joints in power semiconductors, IEEE Transactions on Power Electronics, IEEE, 35(9), pp. 8956–8964.

Sander, M., Dietrich, S., Pander, M., Schweizer, S., Ebert, M. and Bagdahn, J. (2011) Investigations on crack development and crack growth in embedded solar cells, In Reliability of Photovoltaic Cells, Modules, Components, and Systems IV, International Society for Optics and Photonics, p. 811209.

Sangster, A. J. (2014) Solar photovoltaics, In Electromagnetic Foundations of Solar Radiation Collection, Springer, pp. 145–172.

Satpathy, R. and Pamuru, V. (2021) Chapter 5 - Manufacturing of crystalline silicon solar PV modules, In Solar PV Power, Satpathy, R. and Pamuru, V. (eds.), Academic Press, pp. 135–241, [online] Available from: https://www.sciencedirect.com/science/article/pii/B9780128176269000058.

Schiavone, A., Abeygunawardana-Arachchige, G. and Silberschmidt, V. v (2016) Crack initiation and propagation in ductile specimens with notches: experimental and numerical study, Acta Mechanica, Springer, 227(1), pp. 203–215.

Schindler, S., Schneider, J., Poenisch, C., Nissler, R. and Habermann, D. (2013) Soldering process and material characterization of miniaturized contact structures of a newly developed multi busbar cell metallization concept, In 28th European Photovoltaic Solar Energy Conference and Exhibition, pp. 480–483.

Schmitt, P., Kaiser, P., Savio, C., Tranitz, M. and Eitner, U. (2012) Intermetallic phase growth and reliability of Sn-Ag-soldered solar cell joints, Energy Procedia, Elsevier, 27, pp. 664–669.

Schneider, A., Rubin, L. and Rubin, G. (2006) Solar cell efficiency improvement by new metallization techniques-The day4 electrode concept, In 2006 IEEE 4th World Conference on Photovoltaic Energy Conference, IEEE, pp. 1095–1098.

Schneider, J., Turek, M., Dyrba, M., Baumann, I., Koll, B. and Booz, T. (2014) Combined effect of light harvesting strings, anti-reflective coating, thin glass, and high ultraviolet transmission encapsulant to reduce optical losses in solar modules, Progress in Photovoltaics: Research and Applications, Wiley Online Library, 22(7), pp. 830–837.

Schubert, A., Dudek, R., Auerswald, E., Gollhardt, A., Michel, B. and Reichl, H. (2003) Fatigue life models for SnAgCu and SnPb solder joints evaluated by experiments and simulation, In Electronic components and technology conference, IEEE; 1999, pp. 603–610.

Schwark, M., Mühleisen, W., Neumaier, L. and Hirschl, C. (2017) Low silver content, lead free modules with light capturing ribbons, In 2017 6th International Conference on Clean Electrical Power (ICCEP), IEEE, pp. 158–162.

Shalaby, R. M., Kamal, M., Ali, E. A. M. and Gumaan, M. S. (2018) Design and properties of new lead-free solder joints using Sn-3.5 Ag-Cu solder, Silicon, Springer, 10(5), pp. 1861–1871.

Shin, H., Han, E., Park, N. and Kim, D. (2018) Thermal residual stress analysis of soldering and lamination processes for fabrication of crystalline silicon photovoltaic modules, Energies, Multidisciplinary Digital Publishing Institute, 11(12), p. 3256.

Siviour, C. R., Walley, S. M., Proud, W. G. and Field, J. E. (2005a) Mechanical properties of SnPb and lead-free solders at high rates of strain, Journal of Physics D: Applied Physics, IOP Publishing, 38(22), p. 4131.

Siviour, C. R., Walley, S. M., Proud, W. G. and Field, J. E. (2005b) Mechanical properties of SnPb and lead-free solders at high rates of strain, Journal of Physics D: Applied Physics, IOP Publishing, 38(22), p. 4131.

Song, H.-J., sang Yoon, H., Ju, Y., Kim, S. M., Shin, W. G., Lim, J., Ko, S., mi Hwang, H. and Kang, G. H. (2019) Conductive paste assisted interconnection for environmentally benign lead-free ribbons in c-Si PV modules, Solar Energy, Elsevier, 184, pp. 273–280.

Spinella, L. and Bosco, N. (2021) Thermomechanical fatigue resistance of low temperature solder for multiwire interconnects in photovoltaic modules, Solar Energy Materials and Solar Cells, 225, p. 111054, [online] Available from: https://www.sciencedirect.com/science/article/pii/S0927024821000969.

Steinhorst, P., Poller, T. and Lutz, J. (2013) Approach of a physically based lifetime model for solder layers in power modules, Microelectronics Reliability, Elsevier, 53(9–11), pp. 1199–1202.

Stoyanov, S., Bailey, C., Stewart, P. and Morrison, G. (2020) Reliability Impact of Assembly Materials for Micro-BGA Components in High Reliability Applications, In 2020 IEEE 8th Electronics System-Integration Technology Conference (ESTC), IEEE.

Stoyanov, S., Bailey, C., and Desmulliez, M. (2009) Optimisation modelling for thermal fatigue free interconnects in fine-pitch flip-chip packaging, Soldering & Surface Mount Technology, 21(1), pp. 11–24.

Stoyanov, S., Bailey, C. and Mark, C. (2002) Optimisation modelling for flip-chip solder joint reliability. Soldering & Surface Mount Technology, 14(1), pp. 49-58.

Strusevich, N., Stoyanov, S., Liu, D., Bailey, Richardson, C. A., Dumas, N., Yannou, J.M., Georgel ,V. (2006) Modelling the behavior of solder joints for wafer level SiP, 8th Electronics Packaging Technology Conference, pp. 127-132.

Summhammer, J. and Halavani, Z. (2016) Cell interconnection without glueing or soldering for crystalline Si photovoltaic modules, EPJ Photovoltaics, EDP Sciences, 7, p. 75401.

Syed, A. (2004) Accumulated creep strain and energy density based thermal fatigue life prediction models for SnAgCu solder joints, In 2004 Proceedings. 54th electronic components and technology conference (IEEE Cat. No. 04CH37546), IEEE, pp. 737–746.

Söderström, T., Papet, P., and Ufheil, J. (2013) Smart Wire Connection Technology, 28th European Photovoltaic Solar Energy Conference and Exhibition, pp. 495–499.

Tanaka, H., Qun, L. F., Munekata, O., Taguchi, T. and Narita, T. (2005) Elastic properties of Sn-based Pb-free solder alloys determined by ultrasonic pulse echo method, Materials transactions, The Japan Institute of Metals and Materials, 46(6), pp. 1271–1273.

Thaidigsmann, B., Clement, F., Wolf, A., Lohmüller, E., Fertig, F., Biro, D. and Preu, R. (2011) HIP-MWT: A simplified structure for metal wrap through solar cells with passivated rear surface, Energy Procedia, Elsevier, 8, pp. 498–502.

The EU Parliament and the Council of the EU Union (2011) Directive 2011/65/EU of the European Parliament and of the Council: on the restriction of the use of certain hazardous substances in electrical and electronic equipment. Retrieved 01/11/2021, Official Journal of the European Union.

Tippabhotla, S. K., Radchenko, I., Song, W. J. R., Illya, G., Handara, V., Kunz, M., Tamura, N., Tay, A. A. O. and Budiman, A. S. (2017a) From cells to laminate: Probing and modeling residual stress evolution in thin silicon photovoltaic modules using synchrotron X-ray micro-diffraction experiments and finite element simulations, Progress in Photovoltaics: research and applications, Wiley Online Library, 25(9), pp. 791–809.

Tippabhotla, S. K., Radchenko, I., Song, W. J. R., Illya, G., Handara, V., Kunz, M., Tamura, N., Tay, A. A. O. and Budiman, A. S. (2017b) From cells to laminate: Probing and modeling residual stress evolution in thin silicon photovoltaic modules using synchrotron X-ray micro-diffraction experiments and finite element simulations, Progress in Photovoltaics: research and applications, Wiley Online Library, 25(9), pp. 791–809.

Touloukian, Y. S. (1975) Thermal expansion: metallic elements and alloys, Thermophysical properties of matter, IFI/Plenum, 12.

Tsou, C. Y., Chang, T. N., Wu, K. C., Wu, P. L. and Chiang, K. N. (2017) Reliability assessment using modified energy based model for WLCSP solder joints, In 2017 International Conference on Electronics Packaging (ICEP), IEEE, pp. 7–15.

Ulbrich. (2013) Light-Capturing Ribbon. [Online] Available at: https://www.pvribbon.com/?s=Light-Capturing+Ribbon&x=0&y=0

United Nations. (2015) THE 17 GOALS. [Online] Available at: https://sdgs.un.org/goals

Wahid, S. (2015) TSEC, DuPont to showcase V-Series solar panels at Tokyo Expo. [Online] Available at: https://greentechlead.com/solar/tsec-dupont-to-showcase-v-series-solar-panels-at-tokyo-expo-21927 [Accessed 25 February 2015].

Walter, J., Tranitz, M., Volk, M., Ebert, C. and Eitner, U. (2014) Multi-wire interconnection of busbar-free solar cells, Energy Procedia, Elsevier, 55, pp. 380–388.

Wang, E., Yang, H. E., Yen, J., Chi, S. and Wang, C. (2013) Failure modes evaluation of PV module via materials degradation approach, Energy Procedia, Elsevier, 33, pp. 256–264.

Wang, H., Wang, A., Yang, H. and Huang, J. (2016) Study on the thermal stress distribution of crystalline silicon solar cells in BIPV, Energy Procedia, Elsevier, 88, pp. 429–435.

Weber, D., Jani, M. I. R., Grabo, M., Wallscheid, O., Böcker, J., Klaus, T. and Krauter, S. (2018) Lifetime Extension of Photovoltaic Modules by Influencing the Module Temperature Using Phase Change Material, In 2018 IEEE 7th World Conference on Photovoltaic Energy Conversion (WCPEC)(A Joint Conference of 45th IEEE PVSC, 28th PVSEC & 34th EU PVSEC), IEEE, pp. 784–789.

Wiese, S., Kraemer, F., Betzl, N. and Wald, D. (2010) Interconnection technologies for photovoltaic modules-analysis of technological and mechanical problems, In 2010 11th International Thermal, Mechanical & Multi-Physics Simulation, and Experiments in Microelectronics and Microsystems (EuroSimE), IEEE, pp. 1–6.

Wohlgemuth, J. H. (2008) Reliability of PV systems, In Reliability of Photovoltaic Cells, Modules, Components, and Systems, International Society for Optics and Photonics, p. 704802.

Wohlgemuth, J. H., Cunningham, D. W., Monus, P., Miller, J. and Nguyen, A. (2006) Long term reliability of photovoltaic modules, In 2006 IEEE 4th World Conference on Photovoltaic Energy Conference, IEEE, pp. 2050–2053.

Yang, W., Messler, R. W. and Felton, L. E. (1994) Microstructure evolution of eutectic Sn-Ag solder joints, Journal of Electronic Materials, Springer, 23(8), pp. 765–772.

Yao, Y., Long, X. and Keer, L. M. (2017) A review of recent research on the mechanical behavior of lead-free solders, Applied Mechanics Reviews, American Society of Mechanical Engineers Digital Collection, 69(4).

Zarmai, M. T., Ekere, N. N., Oduoza, C. F. and Amalu, E. H. (2015) A review of interconnection technologies for improved crystalline silicon solar cell photovoltaic module assembly, Applied energy, Elsevier, 154, pp. 173–182.

Zarmai, M. T., Ekere, N. N., Oduoza, C. F. and Amalu, E. H. (2016) Optimization of thermo-mechanical reliability of solder joints in crystalline silicon solar cell assembly, Microelectronics Reliability, Elsevier, 59, pp. 117–125.

Zhang, X. P., Yin, L. M. and Yu, C. B. (2008) Thermal creep and fracture behaviors of the lead-free Sn–Ag–Cu–Bi solder interconnections under different stress levels, Journal of materials science: materials in electronics, Springer, 19(4), pp. 393–398.

Zhong, W., Qin, F., An, T. and Wang, T. (2010) Mechanical properties of intermetallic compounds in solder joints, In 2010 11th International Conference on Electronic Packaging Technology & High Density Packaging, IEEE, pp. 520–524.

Zhu, Y., Li, X., Gao, R. and Wang, C. (2014) Low-cycle fatigue failure behavior and life evaluation of lead-free solder joint under high temperature, Microelectronics Reliability, Elsevier, 54(12), pp. 2922–2928.

Appendix A:

Permission to Reuse the Published Materials

In this thesis, a number of Figures from other published works are used (mostly for the introduction chapter). The figures without permission of the copyright holder are redacted from the electronic version of the thesis for the public view. However, the material from the Open Access sources are remained in the version and they are listed in the below table quoting the publisher notes for this purpose (either screenshots of webpages or text notes).

Table 1 Figure 2	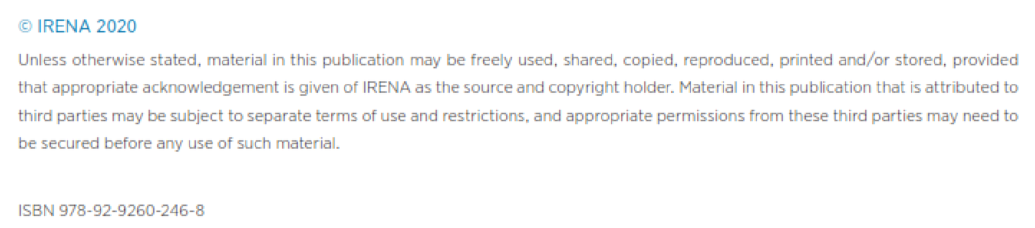 © IRENA 2020 Unless otherwise stated, material in this publication may be freely used, shared, copied, reproduced, printed and/or stored, provided that appropriate acknowledgement is given of IRENA as the source and copyright holder. Material in this publication that is attributed to third parties may be subject to separate terms of use and restrictions, and appropriate permissions from these third parties may need to be secured before any use of such material. ISBN 978-92-9260-246-8
Figure 4	Copyright © 2012 R. Ramaprabha and B. L. Mathur. This is an open access article distributed under the Creative Commons Attribution License, which permits unrestricted use, distribution, and reproduction in any medium, provided the original work is properly cited.
Figure 5	Reusing is agreed under License Number 5236031367035, betwwen the University of Wolverhampton and Elsivier.
Figure 6	This is an Open Access article distributed under the terms of the Creative Commons Attribution License (http://creativecommons.org/licenses/by/4.0), which permits unrestricted use, distribution, and reproduction in any medium, provided the original work is properly cited.
Figure 7	Free to reuse; https://aip.scitation.org/doi/abs/10.1063/1.5053510 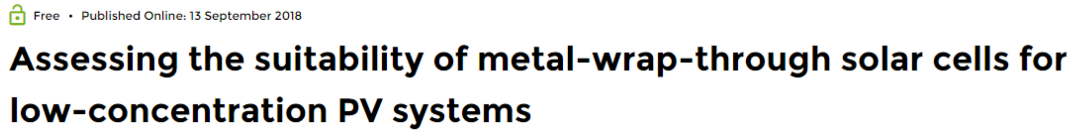 Free • Published Online: 13 September 2018 **Assessing the suitability of metal-wrap-through solar cells for low-concentration PV systems**
Figure 11	This is an Open Access article distributed under the terms of the Creative Commons Attribution License (http://creativecommons.org/licenses/by/4.0), which permits unrestricted use, distribution, and reproduction in any medium, provided the original work is properly cited.
Figure 12	Thesis / Dissertation Reuse The IEEE does not require individuals working on a thesis to obtain a formal reuse license, however, you may print out this statement to be used as a permission grant
Figure 13	Thesis / Dissertation Reuse The IEEE does not require individuals working on a thesis to obtain a formal reuse license, however, you may print out this statement to be used as a permission grant
Figure 15	This is an open access article under the CC BY-NC-ND license
Figure 16	Free to reuse; https://aip.scitation.org/doi/abs/10.1063/1.5049303

	 Home > AIP Conference Proceedings > Volume 1999, Issue 1 > 10.1063/1.5049303 Free • Published Online: 10 August 2018 **Wave-shaped wires soldered on the finger grid of solar cells: Solder joint stability under thermal cycling**
Figure 17	Thesis / Dissertation Reuse The IEEE does not require individuals working on a thesis to obtain a formal reuse license, however, you may print out this statement to be used as a permission grant
Figure 28	Thesis / Dissertation Reuse The IEEE does not require individuals working on a thesis to obtain a formal reuse license, however, you may print out this statement to be used as a permission grant
Figure 47	This is an open access article under the CC BY-NC-ND license